Utrecht University

MSc Sustainable Development

Track Energy and Materials

Master Thesis

Concepts for plasmon-driven chemistry: light-controlled assembly of metal nanoparticles and design of plasmonic reactors

Gabriel W. Castellanos

September 27, 2017

Supervisors:
Prof.dr. Gert Jan Kramer
Dr. Andrea Baldi
Daily supervisor: Rifat Kamarudheen

Second reader:
dr. Wilfried van Sark

DIFFER
Dutch Institute for
Fundamental Energy Research

Summary

Metal nanoparticles are promising catalysts in photo-chemistry, due to their surface plasmon resonances. As part of the fundamental research to bring plasmonic catalysts to applications and devices, plasmonic nanostructures which serve as platforms for the study of their catalytic properties are required. Here we propose an strategy to achieve the assembly of two metal nanoparticles in solution, i.e. a dimer, by virtue of their surface plasmon resonances. We investigated how the surface plasmon resonances of dimers can be used to selectively excite optical and thermal responses, without invoking a significant response in the individual constituent nanoparticles. We find that the size, separation, and material composition are essential parameters to tune the selectivity of the dimer resonances. Notably, only in a specific range of separation distances and sizes is the surface plasmon resonance of the dimer distinguishable from the resonance of the individual nanoparticle. Furthermore, such range is particular to the material composition. Metals with lower losses such as silver have a better selectivity of the dimer resonances. However, the heat generation of dimers is always found less selective that the optical resonance. As such, we concluded that the optical resonances must be tailored, tuning size and separation, to meet the required selectivity of the heat generation.

In addition, we explored how a reactor with plasmon catalysts would look like and what would be its productivity and economic performance compared with a identical reactor operated in the dark, in which the nanoparticles act just as conventional catalysts. We find that owing to an improved selectivity and lower operating temperature, the productivity and economic performance are better in the plasmonic reactor. However, plasmonic reactors require illumination, and by simply using the Beer-Lambert law, we find that such illumination area can be up to several ha (10000 m^2) per every m^2 of reactor. This allows us to discuss future perspectives in plasmonic catalysts for commercial applications.

Contents

1 Introduction

The energy consumption in our present society relies principally in the combustion of fossil fuels such as coal and oil that release greenhouse gases (GHGs) into the atmosphere. The Assessment Reports by the Intergovernmental Panel on Climate Change (IPCC) have shown evidence that anthropogenic greenhouse gases are very likely to be the main driver for climate change[1]. GHGs absorb infrared radiation escaping from surface towards the space and re-emit it in all directions, leading to an increase of the energy being received by the surface. According to the IPCC reports, is expected that at the current rate of fossil fuel consumption, GHGs will lead to an increase of the average surface temperatures of at least 1.5 ℃ within this century[2]. The repercussions of such temperature increase will spread over the whole climate system affecting physical, biological and human systems[3, 4].

On top of this, energy demand is expected to grow during the next decades [5, 6]. Such growth is expected in the middle-income countries for which their economic growth during the 21st century will lead to an increased energy consumption [7, 8]. Consequently, a transformation of the current energy system is necessary to drive the energy consumption away from its negative impacts on the environment[9]. Such transformation will require the deployment and development of free-carbon technologies for the supply of energy and efforts to reduce the demand of energy in the end-use sectors —buildings, industry, agriculture, and transport, by improving energy efficiency[9].

Although current renewable and pilot plant technologies have the potential to olve the carbon and climate problem for the next half century, these solutions will likely only stabilize the carbon emissions[10]. However, the effects in the climate run in a long-term basis, as carbon dioxide has an average lifetime time in our atmosphere that ranges from a few centuries to a few thousand years depending on the carbon sink[11]. Therefore as the energy demand grows other energy solutions would have to be considered and integrated into the energy system.

A promising option to mitigate carbon emissions is the use of photochemistry in solar fuels and chemical processes. Solar fuels are synthetic fuels produced by a chemical reaction in which the solar energy of light is stored in the chemical energy contained in the bonds of molecules[12]. The products obtained have high energy density and could be stored for later use. Notable examples are the production of hydrogen from light-driven water splitting and carbon reduction[13, 14]. In contrast, electricity is difficult to store and current technologies do not provide sufficient energy density to allow for global scale deployment[15]. In the chemical industry, photochemistry could reduce the energy consumption and waste disposal involved in many chemical processes[16]. However, a major drawback of solar fuels is the solar conversion efficiency of the photochemical reactions[17]. To overcome this limitation, current research is focused on the development of efficient catalysts, as they affect the rate of a chemical reaction by altering the activation energies that lead to the formation of products.

The emphasis of this thesis is in the application of plasmonic metal nanoparticles as improved catalysts for photochemistry. Recently, the optical properties of metal nanoparticles have attracted attention as promising light-activated catalysts for en-

hanced product selectivities and conversion efficiencies[18, 19, 20]. In the presence of light, metal nanoparticles support oscillation of their free electrons, called localized surface plasmon resonances[21]. Such excitations in metal nanoparticles can be utilized to control chemical reactions[22]. Due to the electron oscillation, light can be concentrated into small volumes, increasing the number of photons per unit of volume, and therefore the number of photons that are transformed into chemical bonds. In addition, part of the electromagnetic energy is dissipated as hot-electrons above the Fermi level, which can be injected into adsorbed molecules to alter the chemical bonds, and heat, localized near the nanoparticle[23] that could accelerate the reaction by virtue of the Arrhenius equation. Plasmonic particles have demonstrated to drive catalytic conversions at lower temperatures and enable reactions that cannot be activated using conventional thermal processes[18]. Commercially important reactions such as ethylene[24] and propylene[25] epoxidation and carbon dioxide hydrogenation[26] have shown enhanced conversion rates, dependent on the light intensity, when plasmonic catalysts were employed. Consequently, plasmonic photocatalyst materials have the potential to the reduce the energy budget of chemical and increase the conversion efficiencies of solar fuel devices[18].

Yet, plasmonic nanoparticles as efficient catalysts face several challenges if they are to become relevant for solar fuel conversion and industrial applications. Plasmon-driven chemistry still requires research to provide a fundamental understanding of the mechanisms in which a plasmonic nanoparticle can affect a chemical reaction. It is not yet understood to what extent do the several mechanisms described before —photon density, hot-electrons and heat, contribute in a reaction. Therefore it is important to provide a platform where such mechanisms can be studied in detail. In the Nanomaterials for Energy Applications group of dr. Andrea Baldi, at the Dutch Institute for Fundamental Energy Research (DIFFER), we have proposed metal nanoparticle dimers as suitable platforms to study plasmon-driven chemistry. Due to their close proximity the localized surface plasmons of each particle interact, resulting in an enhanced optical response compared with the individual constituent nanoparticle. However, dimers have to be assembled from the individual nanoparticles. A proposed strategy is to assemble chemically nanoparticles in a solution employing the localized and therefore allowing for light-induced control of the assembly. Specifically, we proposed to use the localized heating as mechanism for control of the assembly. However, to achieve such control, tailoring the optical resonances is a fundamental step, which brings us to the first research question of this thesis:

– *What are the necessary conditions that would favor the assembly of plasmonic nanoparticles using a light-controlled reaction?*

The second challenge is concerned with the potential of plasmonic catalysis in the chemical industry. A chemical reactor based on plasmonic photocalytic nanoparticles will attract investment for industrial applications only if is economically more efficient than conventional chemical reactors. While the plasmonic reactor could derive in a higher conversion and less energy requirements, the need for illumination could potentially result in higher costs. And even if is economically attractive, engineering

challenges to integrate the required area for illumination could be problematic. It is therefore essential to quantify to what extent does a plasmonic reactor improves respect traditional reactors, by looking at the economic performance and engineering design. Consequently, we arrive at the second research question presented on this thesis:

– *How does compare the economic performance and design of a plasmonic reactor with the traditional, non-plasmon-assisted and non illuminated, conventional reactors?*

Thesis outline

The work presented in this thesis is divided according to the two research questions presented above. The **section 2** provides the necessary background to understand the optical resonances of metal nanoparticles, how generated is generated by plasmon damping, and how heat is transport at the nanoscale. The **section 3** introduces the general methodology that was used to study the two research questions. **Sections 4**, **5** and **6** present the results obtained during this master thesis. In particular, our first research question was investigated during the internship in the group of dr. Andrea Baldi. The results are described in the **sections 4** and **5**. In section 4 we describe the strategy to excite selectively the plasmon resonance of a dimer, without invoking an optical response of the individual constituent nanoparticle. In section 5 we apply this strategy to study how selective is the heat generation by dimers as result of the optical absorption of the plasmon resonance. The **section 6** is result of the work done with prof. dr. Gert Jan Kramer at the Copernicus Institute for Sustainable Development at Utrecht University, and in collaboration with the group of dr. Baldi. We developed a model to compare the productivity and the economic performance of a plasmon-assisted chemical reactor with a similar reactor working in dark conditions (no illumination) so no optical resonances are excited. We choose a study about the epoxidation of propylene, a relevant industrial process which is energy intensive a generates carbon dioxide. The aim of this study is to compare both plasmonic and dark reactors and find what are the possible economic and design barriers.

2 Theory

2.1 Optical properties of metal nanoparticles

In classical electrodynamics, light is considered as propagating electromagnetic wave, described by Maxwell's equations[27]. When light is incident on an object, the electromagnetic field induces an oscillating polarization in the electrons. This oscillation results in the formation of discrete dipoles and since the electrons are in accelerated motion, these dipoles radiate additional electromagnetic energy in all directions[28]. This radiation, known as *secondary waves*, is called the radiation *scattered* by the object[29]. In addition, the energy of the induced dipole can be lost in the oscillation, leading to *absorption* of light. Absorption depends on the material properties and the frequency of the incident light and therefore can occur via multitude of mechanisms. In this thesis we will restrict ourselves to solid objects at ambient temperature and visible frequencies, for which absorption is due principally to electron scattering with impurities of the solid and electron scattering with the vibrations of the solid, also called phonons[30].

The interaction of light with matter strongly depends on the dimensions of the object compared with the wavelength of light. In particular, most of the classical optics deals with objects that are very large compared with the wavelength of light ($L \gg \lambda$). This has resulted in the well-known laws of reflection and refraction and the theory of diffraction[1]. However, as noted by Lord Rayleigh[31], the laws of reflection and refraction are of no use when the size of the object becomes comparable ($L \sim \lambda$) or smaller ($L \ll \lambda$) to the wavelength of light. In this regime, the interaction of light with small particles depends on the wavelength and results in the scattering of light in different directions[31]. Instead, when $L \sim \lambda$ and $L \ll \lambda$ a rigorous treatment requires solving the Maxwell's equations.

The material composition also affects the light interaction with matter[28, 30]. Materials are typically classified as *metals*, that conduct electricity; *dielectrics*, which do not conduct electricity; and *semiconductors*, which can conduct electricity or not depending on certain conditions. The optical properties of a material are dependent upon the frequency ω of the electromagnetic field and are function of the *electric permittivity* $\varepsilon(\omega)$ and the *magnetic permeability* $\mu(\omega)$[30]. In this thesis we will study noble metals, which are non-magnetic materials and thus $\mu(\omega) \approx \mu_0$.

In the rest of section 2.1, we will combine the electromagnetic theory of Maxwell with the optical properties of metals to predict how light is affected by small particles embedded in dielectrics. In particular we will find that metallic nanoparticles exhibit a very different behavior compared with bulky metals, and that when some conditions are met by the metal, this leads to extraordinary optical properties in the particles.

[1] In fact, the laws of reflection and refraction are result of the interference of the scattered light in the two media, according to the Huygens-Fresnel principle[27]. Then refraction is the result of the interference of the scattered secondary waves with the incident light. The reflection is consequence of the backward propagation of these secondary waves.

2.1.1 Absorption and scattering of light by small particles

Let's start by considering an small particle of arbitrary shape and size as depicted in Figure 2.1. In general, we will consider that the particle is an absorbing medium, meaning that its dielectric function is complex $\varepsilon(\omega) = \varepsilon'(\omega) + i\varepsilon''(\omega)$. The optical properties of the particle are readily obtained using the relation $N = \sqrt{\varepsilon} = n + i\kappa$ where N is the complex refractive index, n is the refractive index and κ is the extinction coefficient. The medium outside the particle is homogeneous, isotropic, linear, non-magnetic and non-absorbing. The particle is illuminated by an arbitrarily polarized monochromatic field $(\mathbf{E_i}, \mathbf{H_i})$ of frequency ω propagating in an arbitrary direction $\mathbf{r}$ and described with an harmonic plane weave:

$$\mathbf{E_i} = \mathbf{E_0} e^{i(\omega t - \mathbf{kr})}, \quad \mathbf{H_i} = \mathbf{H_0} e^{i(\omega t - \mathbf{kr})} \tag{2.1}$$

where $\mathbf{k}$ is the wave vector of the homogeneous medium and is defined as $k = 2\pi N/\lambda_0$ where λ_0 is wavelength in vacuum. The problem consists in determining the electromagnetic field in all points of the space by solving the Maxwell's equations:

$$\nabla \cdot \mathbf{E} = 0 \tag{2.2a}$$

$$\nabla \cdot \mathbf{B} = 0 \tag{2.2b}$$

$$\nabla \times \mathbf{E} = i\omega\mu_0 \mathbf{H} \tag{2.2c}$$

$$\nabla \times \mathbf{H} = i\omega\varepsilon(\omega) \mathbf{E} \tag{2.2d}$$

The field inside the particle will be denoted by $(\mathbf{E_1}, \mathbf{H_1})$ while the field in the surrounding medium $(\mathbf{E_2}, \mathbf{H_2})$ is the superposition of the incident field $(\mathbf{E_i}, \mathbf{H_i})$ and the scattered field by the particle $(\mathbf{E_s}, \mathbf{H_s})$ as illustrated in Figure 2.1. At the interface between the surrounding medium and the particle the electromagnetic field must satisfy the boundary conditions:

$$\mathbf{n} \cdot [\mathbf{E_2} - \mathbf{E_1}] = 0 \tag{2.3a}$$
$$\mathbf{n} \cdot [\mathbf{H_2} - \mathbf{H_1}] = 0 \tag{2.3b}$$

for the normal components, and

$$\mathbf{n} \times [\mathbf{E_2} - \mathbf{E_1}] = 0 \tag{2.4a}$$
$$\mathbf{n} \times [\mathbf{H_2} - \mathbf{H_1}] = 0 \tag{2.4b}$$

for the tangential components. The unit vector $\mathbf{n}$ is normal to the interface between the two media.

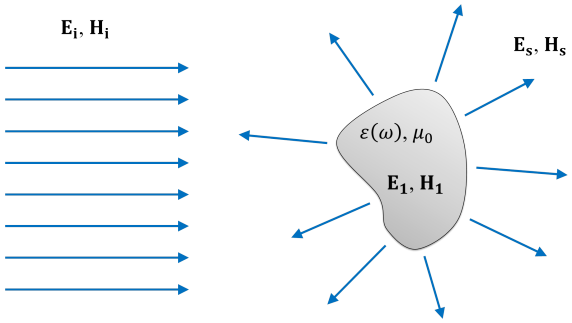

Figure 2.1: The incident field $(\mathbf{E_i}, \mathbf{H_i})$ propagates through the homogeneous medium. When it finds an object of different composition, the interaction results in the scattered field $(\mathbf{E_s}, \mathbf{H_s})$ and the field inside the particle $(\mathbf{E_1}, \mathbf{H_1})$.

Cross-sections of an arbitrary particle

Knowledge of the electromagnetic field in all points of space is used to calculate the redistribution and absorption of light by the particle. Scattering and absorption result in different energy flux per unit area. It is typical to express the scattering and absorption effect as the total scattered and absorbed power per unit area per incident power. Such quantity is called the *scattering* (*absorption*) *cross-section*[28, 29]. The cross-sections can be calculated using *Poynting's theorem*, which states that the energy flux u through a closed volume must be conserved. If a continuous illumination is assumed, the Poynting's theorem is averaged over the oscillation period of the electromagnetic field. One can show then that the conservation of energy is then reduced to the next expression[28]:

$$\mathrm{Re}\int_V \left\langle \frac{\partial u}{\partial t} \right\rangle dV = -\mathrm{Re}\int_V \nabla \langle \mathbf{S} \rangle + \langle \mathbf{J}_f \mathbf{E} \rangle \, dV \tag{2.5}$$

where $\langle \mathbf{S} \rangle = \frac{1}{2}\mathbf{E} \times \mathbf{H}^*$ is the Poynting vector, that determines the flux of electromagnetic energy, and $\mathbf{J}_f$ is the free current density associated with free charges. We recognize in this term the *Joule's effect*[32], responsible of heating in electrical conductors. Such effect is attributed with the absorption of electromagnetic energy, and we termed it as W_{abs}. In the steady-state of continuous illumination the average energy u is zero and the left term of the equation vanishes. Moreover, eq. 2.5 can be further simplified using the divergence theorem:

$$\mathrm{Re}\int_V \left\langle \frac{\partial u}{\partial t} \right\rangle dV = -\mathrm{Re}\int_A \mathbf{S} \cdot \hat{\mathbf{n}} \, dA - W_{abs} \tag{2.6}$$

The surface integral must be evaluated over a volume that encloses the particle. Therefore the Poynting vector is $\mathbf{S} = \frac{1}{2}(\mathbf{E_i} + \mathbf{E_s}) \times (\mathbf{H_i}^* + \mathbf{H_s}^*)$. This vector has the terms $(\mathbf{E_i} \times \mathbf{H_i}^*)$, $(\mathbf{E_s} \times \mathbf{H_s}^*)$ and $(\mathbf{E_i} \times \mathbf{H_s}^*) + (\mathbf{E_s} \times \mathbf{H_i}^*)$. The first and second terms are the incident and scattered energy fluxes, W_i and W_{sca}. Since the incident flux is homogeneous, the surface integral is zero. Finally, after rearranging some terms one

obtains:

$$\frac{1}{2}\mathrm{Re}\left[\int_A (\mathbf{E_i} \times \mathbf{H_s}^* + \mathbf{E_s} \times \mathbf{H_i}^*)\right] \cdot \hat{\mathbf{n}}\, dA = W_{sca} + W_{abs} \tag{2.7}$$

The meaning of the left term is evident: it represents the total extinction of light:

$$W_{ext} = W_{sca} + W_{abs} \tag{2.8}$$

This expression states that the extinction of the flux of radiant energy is due to the scattering, which redistributes the energy, or the absorption by the particle. Therefore, the cross-sections are straightforward to calculate:

$$\sigma = W/I_i \longrightarrow \sigma_{ext} = \sigma_{abs} + \sigma_{sca} \tag{2.9}$$

where $I_i = n_2\, c\, \varepsilon_0 |E_0|^2/2$ is the incident light intensity, c is the speed of light and n_2 is the refractive index of the homogeneous medium. The cross-section is an equivalent area which removes energy from the incident light. Consequently, the interaction of the light with the nanoparticle can be calculated in terms of the cross-sections.

Mie theory and dipole approximation

The scattered fields are determined by the boundary conditions, which depend on the particle geometry. In general, unless the particle geometry exhibits high degree of symmetry, exact solutions to Maxwell's equations are not possible. In addition, it is not possible to solve the scattered fields for a collection of particles in close proximity, as the symmetry is reduced and electromagnetic interactions between particles must be considered[33]. Analytical expressions are possible, based on approximations, and can reveal a great deal of information about the scattered field. We refer to the book of Bohren and Huffman[29] for those interested readers, as it provides a comprehensive treatment of the scattering by arbitrary particles. In most of the cases, however, numerical approximations such as the finite-difference time-domain (FDTD) method or the finite-element method (FEM) have to be employed in order to extract the scattering and absorption cross-sections.

Although non-spherical particles and clusters do not have an exact analytical solution, much of their properties can be understood from the solution of Maxwell's equations for a spherical particle. The formal solution to this problem was derived in 1908 by Gustav Mie, in an effort to understand the various colors resulting from the absorption and scattering in small particle colloids[34]. Mie was able to expand the electromagnetic fields in vector spherical harmonics and derive an analytical expression for the scattered fields and the fields inside the particle. Such derivation is beyond the scope of this thesis and we suggest again the treatment of Bohren and Huffman[29] for curious readers. Here we are interested in the absorption and scattering cross-sections:

$$\sigma_{ext} = \frac{2\pi}{k}\sum_{l=1}^{\infty}(2l+1)\mathrm{Re}\{a_l + b_l\} \tag{2.10a}$$

$$\sigma_{sca} = \frac{2\pi}{k}\sum_{l=1}^{\infty}(2l+1)\left(\mid a_l \mid^2 + \mid b_l \mid^2\right) \tag{2.10b}$$

where a_l and b_l represent the *electric and magnetic scattering coefficients* respectively, and l is an integer number that indicates the *multipole mode*. The dipole mode is $l = 1$, the quadrupole, $l = 2$, and so on. The scattering coefficients a_l and b_l are defined with the *spherical Bessel functions* and are function of the *size parameter* $x = kR$ where R is the particle radius and the *relative refractive index* $m = N_1/N_2$ where N_1 and N_2 are the complex refractive indices of the homogeneous medium and particle respectively.

In this thesis we will study particles of a few tens of nanometer in size, commonly called nanoparticles. We will work in the visible spectrum, which corresponds to the wavelength range $390 - 700$ nm. Therefore one can see that , or equivalently $x \ll 1$. In the limit for very small x it is possible to approximate the spherical Bessel Functions to the first order [29], so that only the dipole term survives. Another way to see this result is from the fact that when $R \ll \lambda$ the spatial modulation of the electromagnetic field, with a size of $\lambda/2$, becomes negligible; the electromagnetic field can be approximated as uniform across the nanoparticle.

Solving for a particle with $R \ll \lambda$ in which the incident field induces a dipole moment, one can find, after substituting the size parameter x and the relative refractive index m, the expression for the scattering and absorption cross-sections[29]:

$$\sigma_{sca} = \frac{k^4}{6\pi}|\alpha|^2 \tag{2.11a}$$

$$\sigma_{abs} = k\mathrm{Im}\{\alpha\} \tag{2.11b}$$

where:

$$\alpha = 4\pi R^3 \frac{\varepsilon_{particle} - \varepsilon_{medium}}{\varepsilon_{particle} + 2\varepsilon_{medium}} \tag{2.12}$$

is called the polarizability, the tendency to separate charges and form dipoles. The dipole moment is defined as $\mathbf{p} = \varepsilon_{medium}\alpha\mathbf{E_0}$. Note that the particle is polarized in the direction of the external field $\mathbf{E_0}$. Any sufficiently small particle, included non-spherical particles can be approximated with dipolar polarization. However, non-spherical particles have an anisotropic polarization, meaning that depending that the induced dipole moment depends on the orientation of the particle with respect the incident electric field $\mathbf{E_0}$. In such case, the polarizability is defined by a tensor. It is worth mentioning the $1/\lambda^4$ dependence in the scattering cross-section. Mie scattering coincides with the theory derived by Lord Rayleigh to explain the scattering of light by the molecules of air which is responsible of the blue color in the sky[31].

It is important to keep in mind the dipole approximation we have presented here. We will see that this model allows to make interpretations of the results obtained in section 4.

2.1.2 Surface plasmon resonances in metal nanoparticles

The cross-sections and the polarizability formulated in eqs. 2.11 and 2.12 are general to any material composition. However, it can be noted that if $\mathrm{Re}(\varepsilon_{particle})$, the real part of the dielectric function of the particle, is negative, the cross-sections exhibit a resonant enhancement when the condition $\varepsilon_{particle} + 2\varepsilon_{medium} = 0$ is satisfied. A negative $\mathrm{Re}(\varepsilon)$ is attributed to materials with free electrons and consequently metal nanoparticles match the condition when they are surrounded by a dielectric medium, with $\varepsilon_{medium} > 0$.

In metal nanoparticles, the gas of free electrons is displaced by the electromagnetic field of the incoming light, leaving a positive ionic background, as illustrated in Figure 2.2. Such displacement creates a surface charge density on the particle[35, 21]. Although from Mie theory it is not evident, Maxwell's equations predict[2] such surface charge oscillations in metal-dielectric interfaces and are called *surface plasmons*[21, 36]. Surface plasmons are collective excitations of the conduction electrons. In a planar surface, surface plasmons propagate carrying with them the electromagnetic field and are known as *surface plasmon polaritons*. In small particles, surface plasmons cannot propagate, and their oscillation is confined. For this reason, they are called *localized surface plasmons*[3].

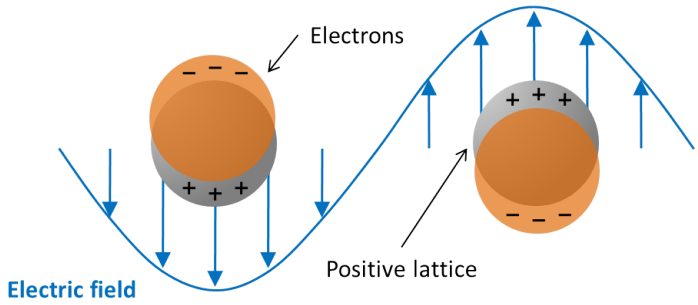

Figure 2.2: The free electrons in a metal nanoparticle (orange) oscillate in presence of an external electromagnetic field. Their oscillation leaves behind a positive ionic lattice (grey) which pulls back the electrons.

The cross-sections of metal nanoparticles is shown in top panel of Figure 2.3 for gold (Figure 2.3a) and silver (Figure 2.3b) spheres of $R = 30\,nm$, calculated using Mie theory. The bottom panel includes the real and imaginary parts of the dielectric function for both materials respectively. At particular energies, the cross-sections exhibit

[2] An excellent description is given by S. Maier[21].

[3] At optical frequencies the skin depth of metals is of a few tens of nanometers (15 nm for gold[35]). Therefore when particles are too small ($R < 10$ nm radius) the distinction between surface and bulk plasmon vanishes.

a resonance, which is attributed to the excitation of a particular surface plasmon, and is called *localized surface plasmons resonance* (LSPR).

The material composition has an important effect in the cross-section of the nanoparticle. Note that absorption is possible only if $\mathrm{Im}(\varepsilon_{particle})$, the imaginary part of the dielectric function of the metal nanoparticle, is different from zero. This is true for real metals where owing to the scattering of electrons with phonons and impurities $\mathrm{Im}(\varepsilon) > 0$. Compared with silver, gold has a larger imaginary part of the dielectric function, resulting in a larger absorption cross-section, but a smaller scattering cross-section than in silver. In particular, the imaginary part of the dielectric function in gold shows an increase around 2.5 eV, due to the interband absorption edge[30], that is responsible of the flat cross-sections at higher energies. Interband absorption results from electronic band structure of metals. Photons with sufficient energy excite optical transitions of electrons from a filled band to the unoccupied band. In silver the interband absorption edge is around 4 eV, so is not observed in Figure2.3. Since the surface plasmon excitation energy does not overlap with interband absorption edge, the resonances in silver are observed in their totality. The LSPR at lower energies is a dipolar resonance, while the LSPR at higher energies is a quadrupole resonance.

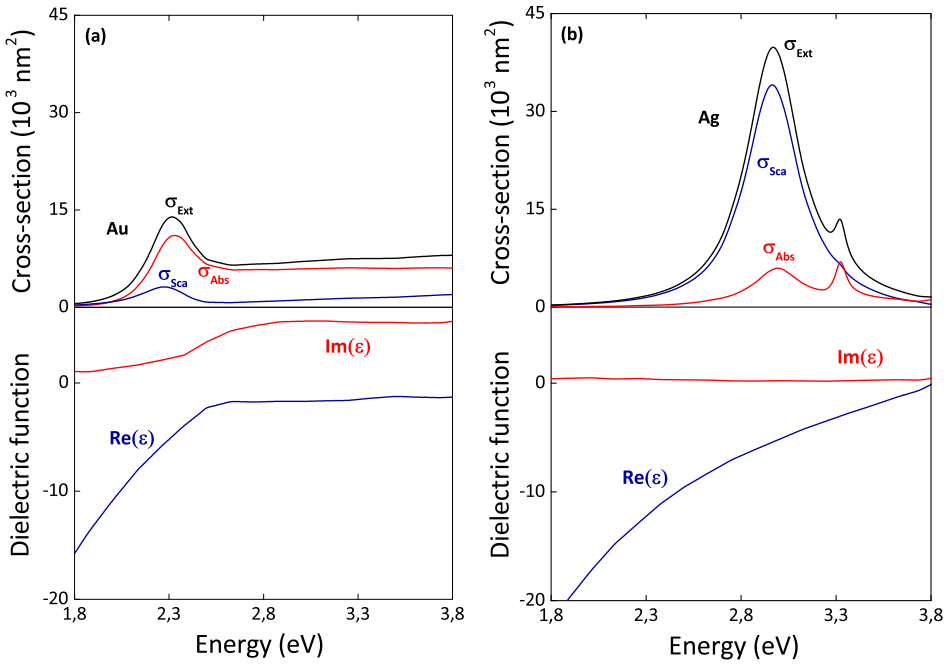

Figure 2.3: Cross-sections and real and imaginary parts of the dielectric functions for gold (a) and silver(b). Silver has a larger extinction than gold due to the smaller $\mathrm{Im}(\varepsilon)$. The dielectric function of silver in this visible is close to that described by the Drude model[30]. In contrast, the presence of the interband in gold around 2.5 eV significantly alters the optical properties of gold. The dielectric functions of gold and silver were extracted from Johnson and Christy[37].

The excitation energy of the surface plasmons can be tuned by several parameters.

The most evident is from the condition $\varepsilon_{particle} + 2\varepsilon_{medium} = 0$, from which we see that a different dielectric medium or metal vary the frequency at which the condition is satisfied. In particular, an increase of the dielectric constant of the surrounding medium leads to a redshift of the surface plasmon energy[35]. Less evident is the effect of shape and size. The shape results is responsible of an anisotropic polarizability, and thus different surface plasmon resonances [29, 38]. Size leads to retardation effects that redshift the surface plasmon resonance[35]. This allows for controlled tuning of the optical properties of metallic particles[38, 39].

The presence of surface plasmon modes that are able to couple directly to the electromagnetic field and the tunability of the resonances has attracted the attention of researchers in the last decades[40, 41, 42, 43, 44, 20]. Due to their surface charge, the electric field in the vicinity of the nanoparticle can be many times greater than electric field of the incident light[45]. Consequently, at close proximity the optical interaction with the nanoparticle is dominated by the near-field. Such intense fields are useful to sensing applications such as surface enhance Raman spectroscopy (SERS)[40]. In addition, the absorption results in the generation of hot electrons[20] and heat generation[42], with applications in chemistry[44], material science[43] and cancer therapy[41].

2.2 Localized heating in metallic particles

2.2.1 Heat generation in plasmonic particles

Plasmons are damped by virtue of radiative or non-radiative mechanisms. In the radiative path, the plasmon is damped to the ground state by re-emission of the absorbed photons (Figure 2.4a). This is responsible of the scattering of light by the nanoparticle. Following a non-radiative mechanisms leads to the absorption of light (Figure 2.4a).

In metal nanoparticles, the non-radiative path this occurs via Landau damping (Figure 2.4a). This mechanism involves the transfer of energy from the plasmon-induced electric field into excitation of hot electron-hole pairs. Landau damping is responsible for the imaginary part of the dielectric function of metals. Due to the typical plasmon energies of a few eV, electron-hole pairs are excited above the Fermi level. This results in population distribution out of thermal equilibrium, as shown in Figure 2.4b. The excess of energy is redistributed, first the rest of the sea electrons and thereupon with the phonons of the metal and the surrouding medium in form of heat (Figure 2.4c).

In order to calculate the heat generated from absorption we go back to the Poynting's theorem in eq. 2.5. We recognized that the absorption term $\mathbf{J}_\mathrm{f}\mathbf{E}$ was the Joule's effect, responsible of heating in electrical conductors. $\mathbf{E}$ is the plasmon-induced electric field inside the nanoparticle and $\mathbf{J}_\mathrm{f}$ is the electric current density that is generated by the conduction electrons of the plasmon in their oscillation. Therefore the heating density $q_{abs}(\mathbf{r})$, expressed in $\mathrm{W}m^{-3}$, is calculated as follows:

$$q_{abs}(\mathbf{r}) = \frac{1}{2}\mathrm{Re}\left[\mathbf{J}_\mathrm{f}^*(\mathbf{r})\mathbf{E}(\mathbf{r})\right] \tag{2.13}$$

where $\mathbf{J}_\mathrm{f}^*$ refers to the complex amplitude ot the electric current density:

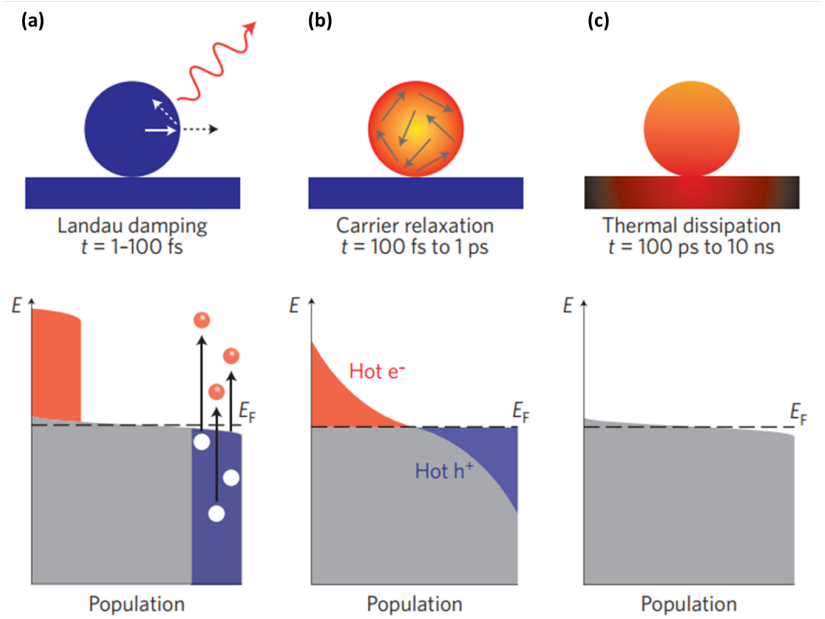

Figure 2.4: Relaxation processes of metallic nanoparticles: **(a)** Following illumination surface plasmons are excited and damping decays via re-emission of the photon (red wave) or creation of electron-hole pairs (red and white circles in the population distribution diagram). The hot electrons (red area) are created above the Fermi energy, leading to a non-thermal population distribution of energies, as represented schematically in the diagram below the particle. **(b)** The hot carriers will redistribute their energy by electron-electron scattering processes on a timescale ranging from 100 fs to 1 ps. **(c)** Finally, electron-phonon scattering results in the increase of temperature of the metal nanoparticle, and heat is subsequently transferred to the to the surroundings of the metallic structure on a longer timescale ranging from 100 ps to 10 ns, via thermal conduction. Extracted from [20].

$$\mathbf{J}_{\mathrm{f}}(\mathbf{r}) = \varepsilon_0 \varepsilon(\omega)\mathbf{E} \tag{2.14}$$

So that the heat density becomes:

$$q_{abs}(\mathbf{r}) = \frac{\omega}{2}\mathrm{Im}\left[\varepsilon_0 \varepsilon(\omega)\right]|\mathbf{E}(\mathbf{r})|^2 \tag{2.15}$$

The integration of eq. 2.15 results in the total absorbed power:

$$Q_{abs} = \int_V q_{abs}(\mathbf{r}) d^3\mathbf{r} \tag{2.16}$$

The heat generation is proportional to the square of the electric field inside the particle. This is an important aspect to consider if we want to design plasmonic structures that act as efficient heat generators. For spherical nanostructures Q_{abs} can be calculated directly from the absorption cross-sections as $Q_{abs} = \sigma_{abs} I$, where I is the irradiation intensity of incoming light. However, for particles of arbitrary shape or for a collection

of particles in close proximity that expression is not valid and in order to calculate the the heat generation we will have to solve numerically eqs. 2.15 and 2.16 at every position inside the particle.

2.2.2 Heat transport at the nanoscale

Let's consider that the dielectric medium in which the metal nanoparticle is embedded is a fluid. Before illumination, the nanoparticle and the fluid are at thermal equilibrium, so the temperature is the same for fluid and nanoparticle. After illumination, heat is generated inside the nanoparticle when the localized surface plasmon is excited, as described by the eq. 2.15. The heat is dissipated by the surrounding fluid which is at lower temperatures. Heat can dissipated via conduction, convection and radiation[46]. In most laboratory experiments, we can safely ignore radiation as the temperatures generated are relatively small while the power radiated is proportional to T^4. Consequently, the dissipation mechanisms to consider are conduction and convection, and they depend on the particle size. In thermodynamics and fluid mechanics, the Rayleigh number[4] is used to discern which is dominant. At the nanoscale, it is found that convection is suppressed and heat is dissipated by the fluid via conduction. When only the conduction term is present energy conservation is described by the heat diffusion equation:

$$\rho c_p \frac{\partial T(\mathbf{r},t)}{\partial t} - \nabla \cdot (k \nabla T(\mathbf{r},t)) = q_{abs}(\mathbf{r},t) \tag{2.17}$$

where ρ, c_p and k are the mass density, the specific heat capacity and the thermal conductivity of the components of the system. The fact that heat is dissipated by conduction means that we can effectively model the fluid as a solid, since only the thermal conductivity is required in eq. 2.17. The thermodynamic parameters of the fluid such as thermal expansivity are not considered because at the nanoscale the bouyant force is suppressed by the viscosity.

The temporal term in the above equation describes the temperature evolution if the heat density changes with time. For a nanoparticle this is the equivalent to an illumination that changes over time. When the particle is illuminated after being in the dark (at same temperature than the solution) it heats up. Then heat is transferred from metal to solvent. According to different theoretical papers[47, 48, 23] under continuous illumination a steady-state temperature is established after a transient evolution. This indeed the case with a continuous-wave (cw) laser. Baffou and Rigneault[48] showed that transient evolution is governed by the thermal relaxation processes of the metal and solvent:

[4]The Rayleigh number can be understood as the ratio between the rate of heat transfer by convection to the rate of heat transfer by conduction. The characteristic length L of the heat source determines whether convection is dominant or not. Nanoparticles are heat sources with $L = 2R \propto 10^{-8}\, m$ which results in $Ra \propto 10^{-21}$ and thus conduction dominates[46].

$$\tau_w = \frac{R^2}{\alpha_w} \tag{2.18a}$$

$$\tau_{metal} = \frac{R^2}{\alpha_{Au}} \tag{2.18b}$$

where R is the particle radius; τ_{metal} and τ_w are the thermal diffusivity of the metal and water respectively. Take gold as example and $R = 30\,nm$; since $\alpha_{Au} = 127 \cdot 10^{-6} m^2 s^{-1} \gg \alpha_w = 0.143 \cdot 10^{-6} m^2 s^{-1}$ then $\tau_{Au} \gg \tau_w$. The nanoparticle achieves thermal equilibrium faster than the fluid. Consequently, the steady temperature profile is determined by the time scale τ_w. Discarding the time dependence the diffusion equation reads now:

$$\nabla \cdot [k(\mathbf{r}) \nabla T(\mathbf{r})] = q_{abs}(\mathbf{r}) \tag{2.19}$$

Similar to the Maxwell's equations, the steady-state diffusion equation can not be solved analytically for non-spherical particles or for a collection of particles. Therefore in this thesis we used numerical approximations to calculate the temperature increase derived from the diffusion equation eq. 2.19.

2.3 Chemical reaction engineering

In the chemical industry, reactions are carried out in vessels, called chemical reactors, that are accordingly designed to withstand the temperature and pressures that lead to a efficient conversion of the reactants into productions. A reactor will vary depending on the type of chemical reaction, the raw chemicals, the products obtained and the catalyst employed[49]. The selection, design and operation of chemical reactors corresponds to branch of engineering known as *chemical reaction engineering*[50, 49].

In particular, industrial reactors are designed to maximize the net present value of a given reaction[49]. Hence, the economics of the overall process must be considered; not only the market value of the reactants and the products, but also the costs of building and operating the reactor. Economic optimization is an important step of the reactor design[50]. Optimization of a reactor, subject to maximizing its net present value, allows to minimize the construction and operation costs while maximizing the benefits incurred with the chemical reactions[50][5].

The design of a industrial reactor involves a variety of areas —thermodynamics, chemical kinetics, fluid mechanics, heat transfer, mass transfer and economics[49]. Mass transfer, thermodynamics and chemical kinetics combine to derive the equations that express the conversion of the reactants into products as a function of the design parameters —reactor volume, concentration, volumetric flow and characteristic time of the reaction. These equations are termed as the *design equations*. Furthermore, heat

[5]Of course, in the first place the chemical reaction must result in a product with higher market value that the reactant.

transfer and thermodynamics can be used to express the conservation of energy through the *energy balance equation*[50, 49]. Together, the design equation and the energy balance equation provide the necessary tools to carry out an economic optimization[50].

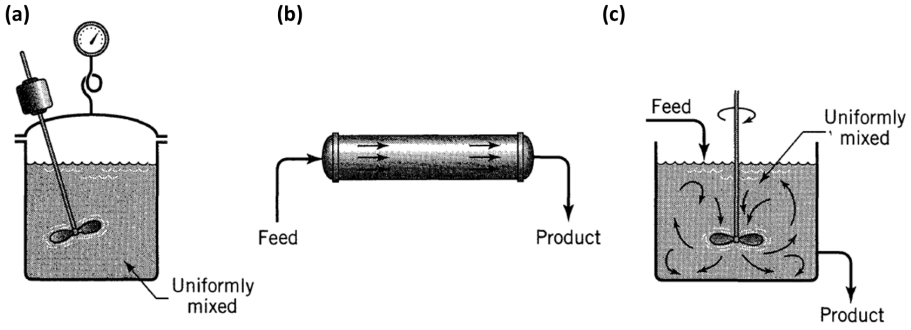

Figure 2.5: The three types of ideal reactors: **(a)** batch reactor; **(b)** plug flow reactor, or PFR; and **(c)** continuous stirred-tank reactor, or CSTR. Extracted from [49].

In the selection of a reactor there are three-basic models used to derivate the design equations and estimate the most important parameters affecting the conversion of the reactant. These are the *batch reactor* model, the *plug flow reactor* model (PFR) and the *continuous stirred-tank reactor* model (CSTR). They are illustrated in Figure 2.5. The choice of model depends on the phase of the reactants and products and the phase of catalyst used. *Homogeneous catalysis* refers to reactions in which the phase of catalysts and reactants is the same. In contrast, in *heterogeneous catalysis* the catalyst has a different phase, usually solid, with respect the phase of the reactants. One of the aims of this thesis is to attempt a first analysis of the feasibility of the use of plasmon resonances in a realistic catalytic reactor. For the sake of simplicity, we will restrict our study to gas-phase that employ solid catalysts. A plug flow reactor is the most suitable model for such reactions[50]. In the rest of this section we will derive the design equations and energy balance for plug flow reactors, which were utilized in this thesis in the design of a plasmonic reactor.

2.3.1 Design equations of a plug flow reactor

A plug flow reactor is a mathematical model that depicts a certain type of continuous reactor operation[6]. This model is based on three assumptions[50]:

- The reactor is operated at steady-state conditions[7]
- The fluid moves in flat velocity profile, also know as "plug flow"
- There is no spatial variation in species concentration or temperature at any cross section in the reactor

Chemical reactions take place along the reactor and, consequently, species compositions and temperature are allowed to vary from point to point along the reactor. Accordingly,

[6] A vessel into which reactants are fed continuously and products are withdrawn continuously from it[50].

[7] There is no mass accumulation inside the reactor[49].

the design equation is formulated for the element of volume dV corresponding to a cross-section of thickness dx, as illustrated in Figure 2.6.

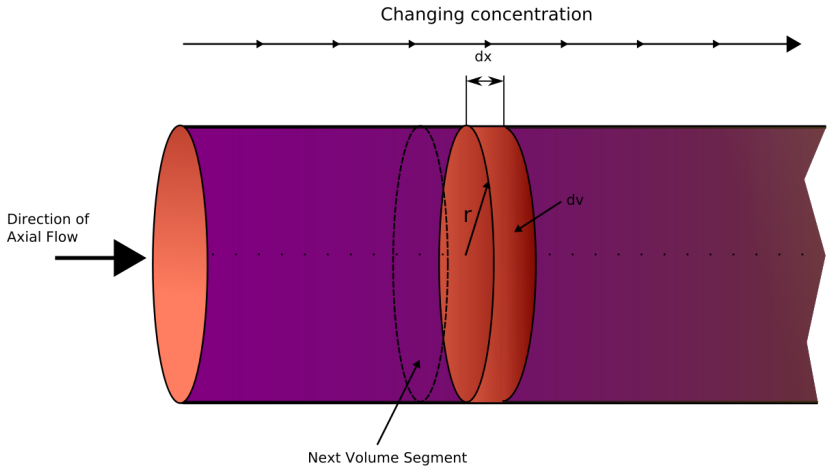

Figure 2.6: Schematic diagram of a plug flow reactor.

The design equation of any reactor is derived from the mass conservation principle, or *material balance equation*[49]. In a PFR it dictates that the input of a chemical species in dV must equal the output of that species in dV_R less the amount of input that reacted:

$$F_j = (F_j + dF_j) + (-r_j dV_R) \tag{2.20}$$

where F_j is the molar flow rate of species j, given in $moles/s$; $(F_j + dF_j)$ is the output of species j, with dF_j representing the change within the element of reactor volume dV_R; and r_j is the formation rate of species j, given in $moles/l/s$.

Before proceeding with the material balance equation 2.20 we need to introduce a series of equations that are fundamental to derive the design equation from the eq. 2.20. In particular we have to formulate dF_j and r_j.

- **The formation rate** r_j: is the sum of all the reaction rates in which the chemical species j is involved:

$$r_j = \sum_{m}^{n_R} (s_j)_m r_m \tag{2.21}$$

  where n_R represents the total number of reactions; $(s_j)_m$ is the stoichiometric coefficient of the *m-th* chemical reaction; and r_m is the rate of the *m-th* chemical reaction.

- **The differential change** dF_j: inside the reactor there are n_R reactions taking place that may contribute or not to creating the chemical species j. The term dF_j can be expressed as function of the extent $d\dot{\xi}$ of each chemical reaction and

the stoichiometric coefficient s_j of the species j in every reaction. The reaction extent is an extensive quantity, with units of mole, that describes the progress of a chemical reaction and is defined as follows[50]:

$$\dot{\xi} = \frac{1}{s_j}\frac{dn_j}{dt} \tag{2.22}$$

where n_j is the molar amount of chemical species j. The advantage of using this formula is that the extent does not depend on the stoichiometry of the reaction since n_j/s_j is constant for every species. With this definition one proceeds to define the differential change dF_j:

$$dF_j = \sum_{m}^{n_R}(s_j)_m d\dot{\xi}_m \tag{2.23}$$

where the stoichiometric coefficients of species j are expressed for the m-th reaction rate with an extent given by $d\dot{\xi}_m$

Coming back to the material balance equation 2.20, after substituting eq. 2.21 and eq. 2.23 and rearranging we find the design equations of a plug flow reactor:

$$\frac{d\dot{\xi}_m}{dV_R} = r_m \tag{2.24}$$

When more than one reaction is taking place, the design equations form a system of ordinary differential equations. Using numerical approximations, such as the Runge-Kutta method these differential equations can be solved[51].

2.3.2 Energy balance of a plug flow reactor

The energy balance in a reaction is derived from the conservation of energy. Each element of volume dV_R can be considered as a closed system; in the steady state the flow of mass entering and leaving the system is constant and conserved, as described by the material balance equation. Therefore the same must occur with the rate of energy entering and leaving the volume dV_R. The energy balance equation states that the rate of change in the total energy $\dot{E}_{tot}$ for any closed system is equal to the change in kinetic energy $= \Delta\dot{E}_{kin}$, potential energy $\Delta\dot{E}_{pot}$ and internal energy $\Delta\dot{U}$ of the chemical species[52]:

$$\Delta\dot{E}_{tot} = \Delta\dot{E}_{kin} + \Delta\dot{E}_{pot} + \Delta\dot{U} \tag{2.25}$$

However, for most chemical processes, the kinetic and potential energy of the streams are negligible in comparison to internal energy[50]. In addition, in the steady state $\dot{E}_{tot}$. This leaves the expression $\Delta\dot{U} = 0$. Using the first law of thermodynamics[52], which states that the change of internal energy is equal to the net heat supplied to the system Q, minus the net work done by the reactor to the fluid W, we obtain:

$$\Delta\dot{U} = \dot{Q} - \dot{W} \tag{2.26}$$

The work rate term, $\dot{W}$ typically consists of three components: the external work done, $\dot{W}_{ext}$, the rate of viscous work, $\dot{W}_{vis}$, and flow work $\dot{W}_{flow}$ done by pushing the streams in and out of the system. In general, the external and viscous work rates can be neglected compared with the flow work[50], and so:

$$\dot{W}_{flow} = \left(\frac{P}{\rho}\right)_{out} \dot{m}_{out} - \left(\frac{P}{\rho}\right)_{in} \dot{m}_{in} \tag{2.27}$$

where ρ is the density of the fluid, different for the inlet and outlet stream; P is the pressure in the volume of element dV_R; and $\dot{m}_{in}$ and $\dot{m}_{out}$ are the inlet mass flow rates in and out of the dV_R. In plug flow reactor the mass flow rate is constant so $\dot{m}_{in} = \dot{m}_{out}$. Noting that definition of specific enthalpy h is:

$$h = u + \left(\frac{P}{\rho}\right) \tag{2.28}$$

we obtain the energy balance equation of a plug flow reactor:

$$\dot{Q} = (h_{out} - h_{in})\,\dot{m} = \Delta\dot{H} \tag{2.29}$$

The change in enthalpy can be more conveniently expressed with parameters derived from the design equation[50]. The enthalpy is a sum of the enthalpy of reaction of all the chemical reactions at the reactor temperature T_0, and the net heat derived from warming the inlet stream and cooling the outlet stream. Therefore the change in enthalpy becomes:

$$\Delta\dot{H} = \sum_{m}^{n_R} \Delta\dot{H}_{R_{m(T_0)}}\dot{\xi}_m + \int_{T_0}^{T_{out}} \sum_{j}^{J} (F_j c_{p_j})_{out} dT - \int_{T_{in}}^{T_0} \sum_{j}^{J} (F_j c_{p_j})_{in} dT \tag{2.30}$$

where $\Delta\dot{H}_{R_m}$ is the *m-th* enthalpy of reaction; c_{p_j} is the specific heat capacity of the species j; J is the total number of chemical species; and T_{in} and T_{out} are the temperatures at the inlet and outlet of the reactor, respectively.

3 Methodology

We divided the methodology in the specific problems that this thesis has dealt with. Namely, the study of the opto-thermal properties of nanoparticles (section 3.1) and the economic performance and design of a plasmonic reactor (section 3.2).

The theoretical study of the opto-thermal properties of nanoparticles and of a plasmonic reactor involve differential equations which cannot be solved analytically. Instead, numerical approximations were employed to solve the several equations introduced in the theory sections 2.1, 2.2 and 2.3. In addition, rather than solving these equations separately, we utilized a holistic approach, developing schemes that included several equations to tackle a particular research question.

3.1 Opto-thermal modeling of nanoparticles in solution

In order to solve the heat diffusion equation 2.19 to study the temperature generated by metallic nanoparticles, the absorbed power density $q_{abs}(\mathbf{r})$ of eq. 2.15 has to be calculated first, which involves solving the Maxwell's equations 2.2 for the nanoparticles and calculating the electric fields inside the nanoparticle. We employed a different software for the thermal and the optical simulations of metallic nanoparticles. The power density was calculated with the optical software for a particular wavelength and was used as input for the thermal software as illustrated in Figure 3.1 for the case of one nanoparticle. In particular, we used this integrated scheme to benchmark the optical and thermal properties of single spherical nanoparticles, since in this case the differential equations 2.2 and 2.19 can be solved analytically.

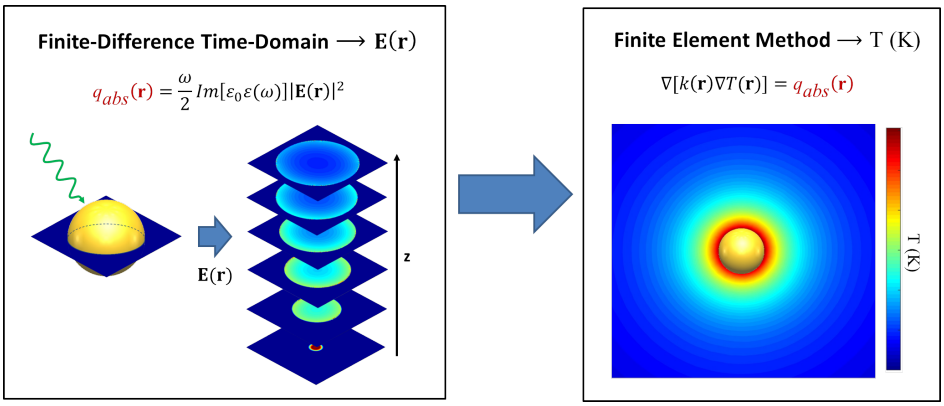

Figure 3.1: Scheme followed to calculate the temperature of optically excited metallic nanoparticles. This figure shows the scheme for the case of a single nanoparticle, and was used to benchmark the simulations against the theory. With the Finite-Difference Time-Domain or FDTD method the optical interaction of a metal nanoparticle with light is simulated. The absorbed power density $q_{abs}(\mathbf{r})$ is calculated for the metal at the wavelength of interest, generating a 2D matrices which are indexed along a direction, as shown in **(a)**. This matrices are the input for the thermal software that simulates the temperature increase using the Finite-Element Method. In particular, **(b)** shows the contour plot of the temperatures near the nanoparticle.

For the optical simulation of nanoparticles we used a commercial software, based on the Finite-Difference Time-Domain or FDTD method. The software presents an environment that allows the design of arbitrary shapes and contains multitude of options such as material properties, illumination conditions and mathematical operations to manipulate the simulated data. The material properties necessary to simulate a material object are the complex dielectric function. FDTD does not simulate magnetic materials, so the magnetic permeability $\mu(\omega)$ is equal to the vacuum value μ_0. In addition, in order results which can be compared with experiments, the complex dielectric function used should be empirical, i.e. measured from experiments. Notably, the real and imaginary parts of the dielectric function are related with each other via the Kramers-Kronig relations[30]. Some empirical dielectric functions satisfy this relations in a better degree than others. In particular, for gold in the visible the data measured by Johnson and Christy[37] was used in all the simulations. The empirical data is fitted by the software with a power series. It is important to be careful with the fitting parameters, or the simulated cross-sections will be unphysical. To calculate the cross-sections and the absorbed power density of the simulated object, the software utilizes eqs. 2.7 and 2.15 respectively. The absorbed power density is the input for the thermal software. FDTD discretizes the simulation volume and calculates $q_{abs}(\mathbf{r})$ for each finite element. The resulting values of $q_{abs}(\mathbf{r})$ for the particle are contained in a 3D matrix, that consists on a series of 2D matrices indexed along a given direction, as can be seen in Figure 3.1a for a single nanoparticle.

The temperature was simulated using another commercial software, based on the Finite Element Method to solve the diffusion eq. 2.19. This software simulates the conduction of heat in nanoparticle contained in a closed volume. The nanoparticle can be surrounded by a solid or a fluid. However, in section 2.2.2 we mentioned that at nanometer dimensions fluids behave thermodynamically like a solid. Therefore, every medium was simulated as solid, using its thermal conductivity. Moreover, in the case of solids, the thermal software can generate contour maps of the temperature, as shown in Figure 3.1b for a single metal nanoparticle. Contour maps are useful tools that allow to investigate the spatial distribution of the temperature in the medium around the nanoparticle.

The Finite Element Method requires a set of boundary conditions for the surface areas that enclose the simulation volume, which can be a finite temperature, a constant gradient of power leaving the simulation volume or isolating boundaries (no heat leaves the simulation volume). In our simulations, the surrounding medium is at ambient temperature before the nanoparticle is excited. In a real laboratory experiment, the medium is typically several orders of magnitude larger than the nanoparticle, and it behaves as a thermal reservoir. However, in the software, a larger simulation volume requires more time and memory for the simulation. Therefore, a trade-off is necessary. Typically, volumes of several μm^3 were used for all the simulations of this thesis. In addition, Brownian motion is not considered in the local response of the nanoparticles. The characteristic time for relaxation in the random motion of a nanometer size object is in the range of femtoseconds[8]. In this time a nanoparticle only displaces a few tens

[8] A femtosecond is 10^{-15} s and is denoted with the symbol fs.

of angstroms [9]. With such a fast relaxation the fluid is approximately in rest with the nanoparticle.

3.2 Design and assessment of plasmonic reactors

Since plasmon-induced chemistry is at a fundamental research stage, the design of a plasmonic reactor of industrial size requires scaling up of the small laboratory reactor to industrial dimensions. Here we introduce a model to assess the economic performance and design of plasmonic reactors that builds around the selection of the chemical reaction and the design equations. Therefore other engineering and economical aspects which cannot be derived from the reactor production, operation or dimensions will not be considered as the level or uncertainty introduced in the respective assumptions will lead to a propagation of error in the results, i.e. production, profits, costs, and illumination requirements. Our model to assess a plasmonic reactor consists in the following steps:

1. **Study of the chemical reaction**: The first step consist in selecting the chemical process. To calculate the stoichiometric coefficients of the chemical process, first it must decomposed in its elementary reactions. In an elementary reaction the speed of generation of a product C, in the general reaction $aA + bB \longrightarrow cC$, is called the reaction rate and is determined by the reactant concentrations, $[A]$ and $[B]$:

$$\frac{d\,[C]^c}{dt} = k\,[A]^a\,[B]^b \tag{3.1a}$$

   where a, b and c are the stoichiometric coefficients of the reaction, $[C]$ is the concentration of the chemical product, and k is called the reaction rate constant. In a chemical process, there maybe a large number of reactants, and A and B may participate in other reactions with different stoichiometric coefficients and products. In addition, the products of a particular elementary reaction can be reactants for another elementary reaction. The elementary reactions are specific to the chemical process considered and the catalyst used. Notably, two catalysts used in the same chemical process will in general have different elementary steps.

2. **Derive design equations**: After determining the elementary reactions, we proceed to derive the design equations for each elementary reaction. The design equations determine the rate of product formed as function of the reactor size V_R. First we must select the reactor model, i.e. batch, continuous stirred tank, or plug-flow. For heterogeneous catalysts such as solid particles and gas phase reactants the plug-flow reactor model was mentioned the most appropriate. In

[9] An angstrom is 10^{-10} m, or 0.1 nm, and is denoted with the symbol Å. Angstroms are the typical unit distance used for the atomic scale.

such case, the design equations are described by eq. 2.24 as a differential equation of the rate of reaction extent $\dot{\xi}$ with respect the reactor volume V_R:

$$\frac{d\dot{\xi}}{dV_R} = r \tag{3.2}$$

where r is the reaction rate for the elementary reaction derived from the step 1. When more than one reaction takes place in the reactor, the design equations form a system of ordinary differential equations (ODEs):

$$\frac{d}{dV_R}\begin{bmatrix}\dot{\xi}_1\\ \vdots \\ \dot{\xi}_n\end{bmatrix} = \begin{bmatrix} r_1 \\ \vdots \\ r_n\end{bmatrix} \tag{3.3}$$

where n is the number of elementary reactions, with rate of reaction extents $(\dot{\xi}_1, \cdots, \dot{\xi}_n)$ and reaction rates $(r_1, \cdots, r_n)$. To solve such ODEs, we use MATLAB throughout this thesis.

3. **Scaling up**: Based on current industrial reactors that perform the same or similar chemical processes, we extrapolate input parameters in the design equations that lead to a industrial scale production. Namely such parameters are the *volumetric flow* (m^3/h), the *pressure* (atm) and the amount of catalyst (g_{cat}) per m^3 of reactor, i.e. the *catalyst packing density*.

4. **Area of illumination**: In the design of a plasmonic reactor light has to be taking into account. For a given reactor size V_R, the illumination area A_I imposes a constraint in the reactor. To excite plasmonic nanoparticles, light must be absorbed by the nanoparticles. According to the Beer-Lambert law[30], the intensity of light decreases exponentially inside of an absorbing medium, such as the catalyst bed illustrated in Figure 3.2:

$$T = \frac{I_t}{I_0} = \exp(-\sigma_{ext} n \ell) \tag{3.4}$$

where T is the transmittance, and I_t and I_0 are the transmitted intensity at a distance z and the incident intensity, respectively. The parameter σ_{ext} is the absorption cross-section, as introduced in theory section 2.1, n is the particle concentration and ℓ is called the *path length* traveled by light.
Given a certain reactor volume and reactor design, the path length, as determined by the Beer-Lambert law, imposes a strict the constraint on the optically accessible area. Rearranging the eq. 3.4 we obtain the path length for a given transmittance:

$$\ell = -\frac{\ln(T)}{-\sigma_{abs} n} \tag{3.5}$$

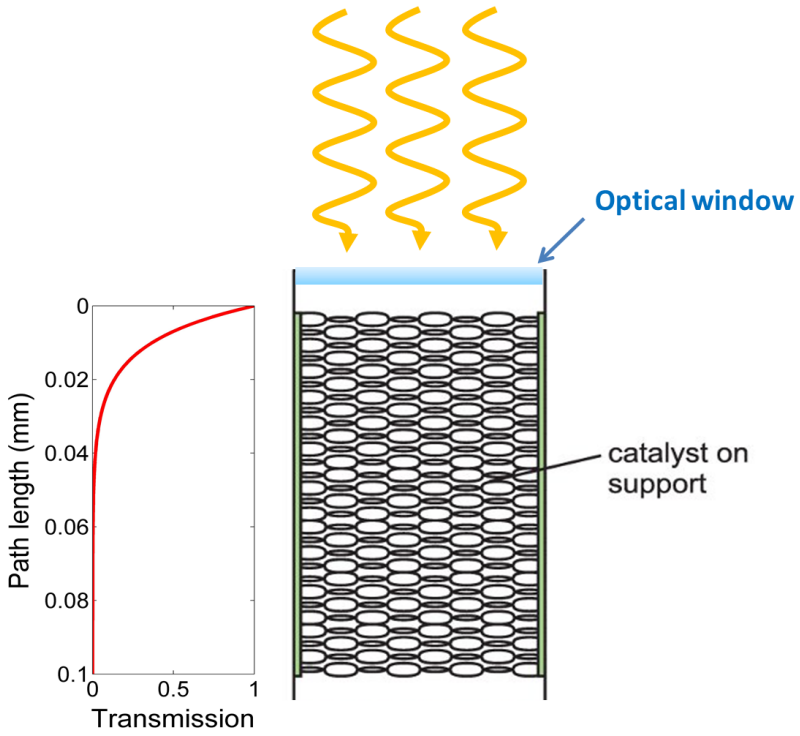

Figure 3.2: Illustration of the transmittance of light as it propagates through an absorbing medium inside a reactor. The light, irradiated from outside, reaches the catalytic support through an optical window, i.e. a transparent medium to the wavelengths of the irradiation source. Since the catalytic nanoparticles absorb and scatter light, the intensity of light is reduced, according to the Beer-Lambert law, which is plotted at the left of the reactor.

We can observe that to calculate the path length, we need to make an assumption about the transmittance T. It can bee seen in Figure 3.2 that small transmittances result of small path lengths, which in turn will lead to a larger area for a given reactor volume.

5. **OPEX and CAPEX of the reactor**: From an economic perspective industrial reactors are equipment with the following associated costs:

   - **Capital expenditure** (CAPEX): the capital costs of investment associated with building the industrial reactor. It depends on the materials utilized and the reactor volume. From an economic perspective, is typical that in the first years of operation, the capital costs I are returned to the investors at a given percentage every year, known as the *capital recovery factor* α.
   - **Operating expenditure** (OPEX): the costs of operation such as heating of reactants, pumping, cooling and distillation. As mentioned before, only the costs which can be derived from the reactor operation and production are considered in this thesis, since they can be calculated from the design

equation. Such costs are associated with the heating and the raw chemical purchase.

6. **Perform economic-based optimization**: A profitable chemical reactor must cover the operating expenses and the cost of the equipment, CAPEX, with the benefits derived of selling the chemical products. On a yearly term the cash-flow $Z(V_R)$ generated by a reactor volume is:

$$Z(V_R) = -\alpha I - C + B \tag{3.6}$$

The benefits B are cash inflows, while the operating costs C and the annual capital costs $-\alpha I$ are cash outflows. If $Z(V_R) > 0$ the reactor produces a profit and if $Z(V_R) < 0$ then the reactor incurs into economic losses. In order to obtain the maximum benefit, we want to find the maximum cash-flow $Z(V_R)$ as a function of the reactor volume V_R and therefore we impose the condition:

$$\frac{dZ(V_R)}{dV_R} = 0 \tag{3.7}$$

In other words, looking at the zeros of the derivate of the net cash-flow with respect the reactor volume we find the value of the reactor volume that lead to maximum net-cash flows. We refer to such volumes as the optimum reactor sizes.

We remark that each reaction has a different chemistry. The results obtained with one reaction cannot be applied for other reactions and therefore we always will have to follow these steps whenever a new chemical process is studied.

4 Utilizing plasmon coupling to assemble nanoparticles with light

4.1 Introduction

When two plasmonic nanoparticles, i.e. a dimer, are brought in close proximity, their individual surface plasmons can interact with each other, through the electric fields created by the surface charges[53, 33]. Such interaction results in a shift of the surface plasmon excitation energy, which depends on the interparticle separation or gap, with smaller gaps leading to larger plasmon resonances shifts[54, 55, 56]. Furthermore, when the external electric field drives the surface charge oscillation across the gap, strong fields in the gap and plasmon resonance red-shifts, i.e. lower excitation energies, can be achieved with respect to the ones of the constituent nanoparticles. An analytical theory where such energy shifts are described using a Coulomb potential between the surface charges caused by the localized surface plasmons was derived by Nordlander *et al.* [33]. Alternatively, a simpler yet powerful picture can be obtained by approximating the surface plasmons with an oscillating dipole field [55], where such energy shift is explained as consequence of dipole-dipole interaction energies. Remarkably, both theoretical models predict that the electric forces between the nanoparticles lead to the coupling of the individual plasmons, to form a coordinated single collective plasmonic oscillation.

Dimers are exceptional platforms to study plasmon-assisted chemistry. When the external field leads to an enhanced electric field in the gap, the absorption and scattering cross-section of the dimer increase with respect to the cross-section of the constituent nanoparticle[57]. Enhanced fields in the gap are translated in a larger photon density, and as result of the increased absorption, dimers are more efficient generators of hot-electrons and heat. Consequently, the optical properties of dimers can lead to increased catalytic effects in a chemical reaction. Moreover, dimers would allow us to remotely detect alterations in the chemical environment of the gap through surface-enhanced Raman scattering (SERS) measurements[58]. SERS depends on the intensity of the electric field, and dimers would provide the largest field enhancement, thus allowing us to trace the chemical reactions catalyzed by dimers.

Assembly of dimers for the study of plasmon-assisted chemistry requires a control of the gap and size of the nanoparticles. For applications in chemistry, such dimers must be dispersed in solution, which makes their assembly challenging. Top-down techniques for the fabrication of particle assemblies such as electron beam lithography, nanoimprinting or nanosphere lithography are limited to fabricating nanoparticles on a substrate, limiting their applications to 2D geometries.

Instead, a better approach for colloidal dimers is their assembly in solution. The current strategy for nanoparticle assembly in a solution consist in the manipulation of the interaction forces between the nanoparticles (such as such as covalent or hydrogen bonding, electrostatic interaction between charged ligands, or steric forces), also referred as self-assembly[59].

However, achieving high yields of a specific aggregate structure, e.g. a dimer, via

self-assembly remains challenging. Recently, it has been reported that by exciting the resonance of plasmon coupled nanoparticle is possible to trigger a chemical reactions in the gap or prevent the aggregation of assemblies other than dimers[60, 61].

In the Nanomaterials for Energy Applications group at DIFFER, where I conducted my thesis work, we propose to use the plasmon coupling to control the assembly of nanoparticle dimers. Due to Brownian motion, nanoparticles in a solution collide with each other, with a probability that depends on the temperature, the concentration, and the viscosity of the solvent. Plasmon coupling in dimers presents the advantage that both optical and thermal properties depend upon the irradiation wavelength, the composition and size of the dimer, and in particular of the gap[58]. Therefore, we propose to irradiate the solution at a dimer resonance for a given separation gap, since it would allow us to selectively excite nanoparticles in the solution that are close enough to match the target dimer resonance.

As result of the irradiation, heat would generated only for the resonant coupled dimers, which would result in an increase in temperature localized near the dimer. We propose to use such temperature increase to bind the pair of interacting nanoparticles. Our strategy is illustrated in Figure 4.1. According to the Arrhenius equation, the rate of endothermic reactions increase exponentially with temperature. As such, one could strategize to use plasmonic heating to accelerate chemical reactions[22] only in the vecinity of nanoparticle dimers.

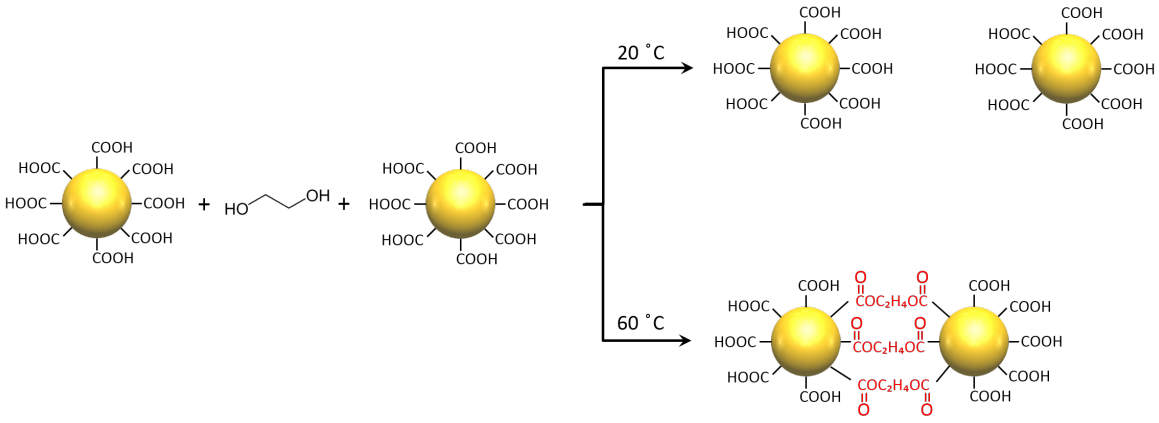

Figure 4.1: Heat assisted assembly of nanoparticles. Heat assisted esterification of carboxylic acid functionalized gold nanoparticles with hydroxyl groups on ethylene glycol, is illustrated here. Heat generation by resonant excitation of the coupled plasmons, can be used to enhance the esterification rate locally, so as to assemble two nanoparticles to form dimers

The reaction we propose is a Fisher esterification, a reaction between a carboxylic acid $R-COOH$ and alcohol $R'-OH$ to form an ester[62]. Specifically, the carboxylic acid is attached to the nanoparticle through the radical R. It is essential that the carboxylic acids of both nanoparticles react with the alcohol to form an ester bridge that ties the dimer together. Bydentate glycols, containing two $-OH$ are ideal candidates to form this bridge with the nanoparticles. The radical of the carboxylic acid must be a capping ligand that prevents the uncontrolled aggregation of nanoparticles that results

in their precipitation. A commonly employed capping ligand is poly-ethylene glycol (PEG). For the bydentate glycol, ethylene glycol was the organic molecule considered.

The temperature control of the esterification depends on the degree to which a target dimer can be selectively excited for an irradiation wavelength. Therefore, an important step previous to realization of the experiment is to study the selectivity of nanoparticles. The optical spectrum of dimers cannot be solved analytically and numerical approximations are necessary. Here we simulated electromagnetic interaction of dimers with light using the Finite-Difference Time-Domain (FDTD) method. We simulated gold and silver dimers, using the empirical data for dielectric function from Johnson and Christy[37]. We focused on the absorption cross-section of the dimers and of the constituent nanoparticle, since the heat generation depends of the electric field inside the nanoparticles, according to eq., which are related to the absorption cross-section. In section 4.2 we take a deeper look at the strategy that aims at selective excitation of dimer resonances. In section 4.3 we further investigate the parameters affecting the dimer resonance, namely the separation between the two constituent particles, the nanoparticle size and the choice of metal using FDTD simulations.

4.2 Defining spectrum contrast for selective excitation

The selectivity of dimer resonance is the degree to which such resonance wavelength does not invokes an optical response of the constituent nanoparticle. Selectivity is affected by the redshift and the intensity of the dimer resonance with respect the constituent nanoparticle. If the dimer resonance is red-shifted to larger wavelengths, i.e. lower energies, the plasmon resonance of constituent nanoparticle is not longer excited. If the cross-section of the constituent nanoparticle is many times smaller than cross-section of the dimer resonance, it can be ignored, as the heat generation would be small. To account for these two effects we defined a new parameter termed '*contrast*'. We use the contrast parameter to understand how to selectively excite dimer nanostructures without exciting individual nanoparticles. The criteria for this parameter is to score a high value for higher selectivities and low values for lower selectivities. Since selective excitation involves low overlap between the spectra of the dimer and the constituent nanoparticle, we define contrast as:

$$C(\lambda) = 1 - \frac{\sigma_{NP,abs}(\lambda)}{\sigma_{D,abs}(\lambda)} \tag{4.1}$$

where $\sigma_{NP,abs}(\lambda)$ and $\sigma_{D,abs}(\lambda)$ are the absorption cross-sections of the constituent individual nanoparticle and of the dimer respectively, at the wavelength of interest.

Ideally, to maximize the contrast parameter $C(\lambda)$, we would like to have a solution of nanoparticles irradiated with monochromatic light at a wavelength λ at which the absorption cross-section of the constituent nanoparticle $\sigma_{NP,abs}(\lambda)$ os small, while the absorption cross-section of the nanoparticle dimers $\sigma_{D,abs}(\lambda)$ is large.

A first step consists in study and select a particular resonance mode for the different polarizations present in the dimer. Next, we will explore how to maximize $C(\lambda)$ while varying the dimer separation, the nanoparticle size and their composition.

4.3 Selective excitation of dimer resonances

4.3.1 Longitudinal and transverse modes

Dimers consisting of two identical spherical particles, or homodimers, have two well defined rotational axes of symmetry[10], that are typically called *transverse* and *longitudinal* axes[11](Figure 4.2). Consequently, the electromagnetic interaction between the nanoparticles is angle-dependent with the electric field respect to the axes of symmetry, since the electric surface charge of each nanoparticle oscillates in the direction of the incident electric field[33]. Each axis of symmetry of the dimer leads to different coupled plasmons, called *longitudinal* and *transverse modes*, and are shown in the top panel of Figure 4.2.

As a first step in our analysis, we compared the dimer's longitudinal and transverse modes to the plasmon resonance of the individual nanoparticle. As can be seen in Figure 4.2, the longitudinal mode shows a large spectral shift and increase in the extinction cross-section intensity with respect to the single particle resonance. In contrast, the dimer resonance for transverse mode has a shift of only 2 nm. From the spectra, it is therefore clear that the transverse mode offers a low contrast and would be unsuitable for our strategy.

In particular, since the nanoparticle size is smaller than the wavelength of light, the electric dipole-dipole interaction potential V_{dd} allows to explain in simple terms the observed spectra of Figure 4.2[28]:

$$V_{dd} = \frac{1}{4\pi\varepsilon_0 r_{12}^3}\left[\mathbf{p}_1\mathbf{p}_2 - 3\frac{(\mathbf{r}_{12}\cdot\mathbf{p}_1)(\mathbf{r}_{12}\cdot\mathbf{p}_2)}{r_{12}^2}\right] \tag{4.2}$$

where ϵ_0 is the vacuum permittivity, r_{12} is the separation between the two nanoparticles and $\mathbf{p}_1$, $\mathbf{p}_2$ are the dipole moments of each nanoparticle, which are parallel to the electric field of the irradiating light.

The total electric force experienced by each constituent nanoparticle is a sum of the incident electric field and the electric dipole field created by the oscillation of free electrons from the neighboring particle. The total potential energy is therefore different from the individual particles, as the dipole-dipole interaction potential has to be included.

[10]Rotational symmetry is that symmetry in which an object rotated by a certain angle along an axis that passes through its center remains identical to the object before the transformation. An sphere for example remains identical for any given rotation, while a equilateral triangle remains identical for rotations of 120°.

[11]In spherical nanoparticles, the orientation of the axis of symmetry is arbitrary. Any orientation chosen is automatically an axis of symmetry. We can see that this is no longer truth when there are more than two spheres. Now the rotational symmetry in the axis that passes through the center of the two spheres is no longer arbitrary. There is a second rotational symmetry, that for an axis that passes through the center of the dimer, i.e. the middle of the center-to-center distance, and is perpendicular to the first axis of symmetry.

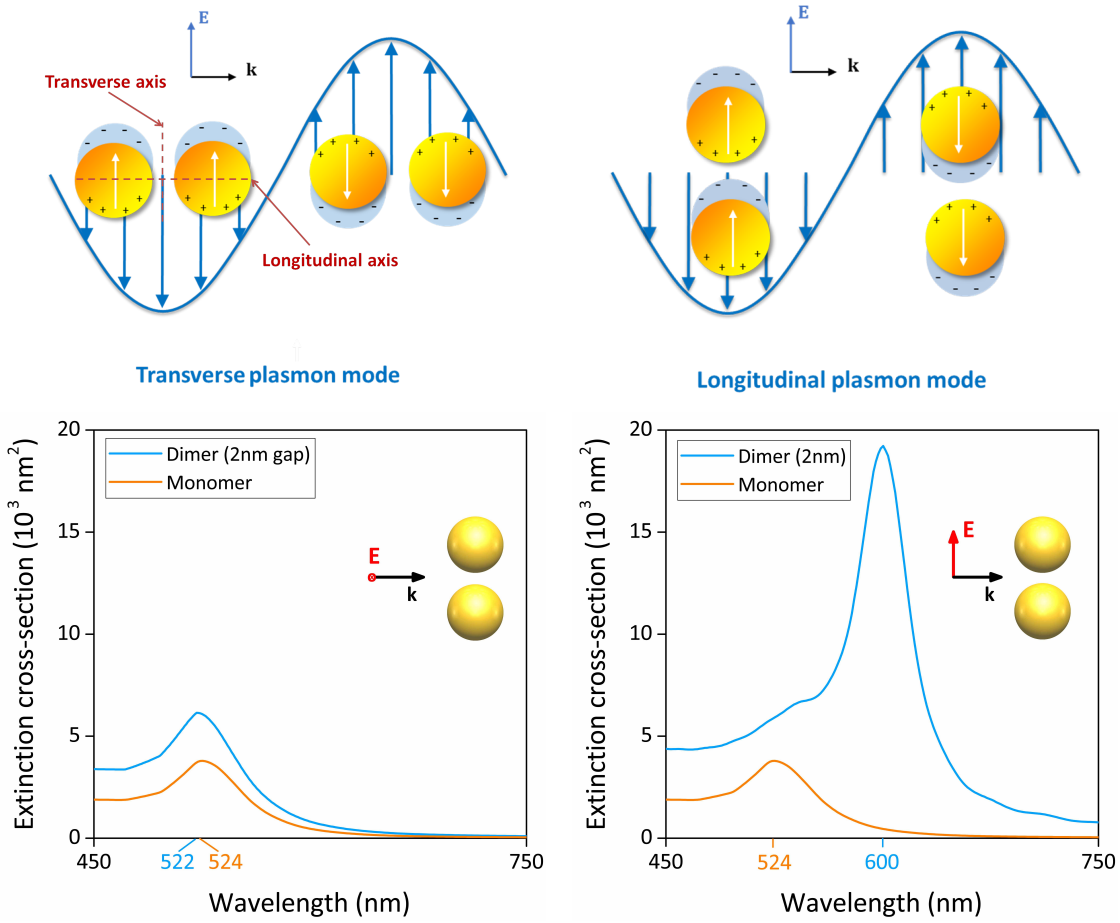

Figure 4.2: Plasmon coupling modes for two identical and spherical nanoparticles. **Top panel**: The incident electric field drives the oscillation of the electrons, resulting in accumulation of surface charge. Here, the dipole mode is illustrated, and the white arrow represents the dipole moment of the nanoparticle. The electric field has two orientation relative to the symmetric axis of the dimer, leading to two different coupling modes: transverse and longitudinal. **Bottom panel**: Extinction cross-sections calculated with FDTD for a dimer of 20 nm radius gold nanoparticles with a separation distance of 2 nm in a dielectric with refractive index $n = 1.33$, for the transverse (left figure) and longitudinal (right figure) modes. The extinction of the dimer (blue) is compared with the extinction of the monomer (orange), a single gold nanoparticle of 20 nm radius. The colored wavelengths represent the localized surface plasmon resonances of the dimer (blue) and of the monomer (orange).

In the transverse mode, the dipole moments of the nanoparticles, $\mathbf{p}_1$, $\mathbf{p}_2$, are perpendicular to the separation vector r_{12}, the second term in the brackets of eq. 4.2 is zero. The interaction interaction energy is positive, which results in a dimer resonance energy higher compared with the plasmon resonance of the individual nanoparticle, i.e. a blue-shift. In the longitudinal mode, the dipole moments, $\mathbf{p}_1$, $\mathbf{p}_2$, are parallel to the separation vector r_{12} and the interaction energy is negative if $3(\mathbf{p}_1\mathbf{p}_2/r_{12}^2) > \mathbf{p}_1\mathbf{p}_2$. A negative interaction energy leads to lower dimer resonance energy compared with the plasmon resonance of the individual nanoparticle, i.e. a red-shift.

4.3.2 Effect of separation

After having established that the dimer longitudinal mode is the most promising resonance to use in our light-driven synthesis, we now consider the effect of the interparticle separation. We performed FDTD simulations on a system consisting of two 40 nm gold nanoparticles suspended in water (n = 1.33), while varying the interparticle distance from 1 nm to 30 nm. The studies performed here were in the absence of any surface ligands on the gold nanoparticles. Simulations with gap sperations of less than 1 nm cannot be performed accurately using FDTD, as quantum tunneling of electrons start to occur between the nanoparticles [63]. As FDTD is based on classical electrodynamics, it cannot account for quantum mechanical processes.

Figure 4.3 shows the effect of separation in the absorption cross-section as a function of the wavelength. The straight white line shows the surface plasmon resonance wavelength of the individual constituent nanoparticle. The white curve shows the peak position of the dimer's longitudinal resonance, which red-shifts by up to 130 nm as the nanoparticle separation decrease to 1 nm.

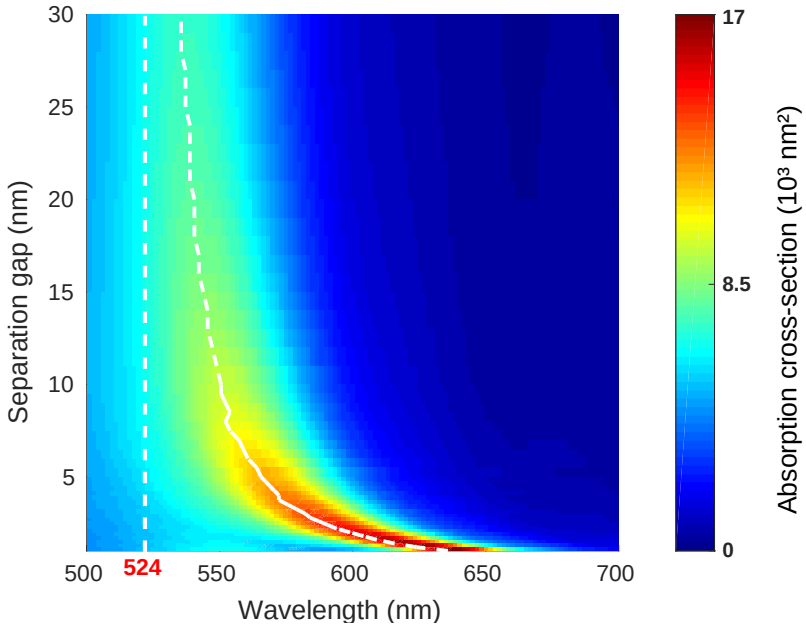

Figure 4.3: Effect of separation gap in the absorption cross-section of a dimer. Contour plot of the absorption cross-section calculated with FDTD for the longitudinal mode of 20 nm radius gold nanoparticle dimer in a dielectric with refractive index $n = 1.33$. the separation gaps vary between 1 nm and 30 nm. The white straight dashed line represents the resonance wavelength of an monomer, which is shown by the red number in the wavelength axis. The white dashed curve represents the dimer plasmon resonance as a function of the separation.

It can be seen from the marked redshift for distances below 10 nm that plasmon coupling is most effective at small separations. This result due to dependence of the

plasmon coupling strength with the separation gap, in agreement with the model of Nordlander *et al.*[33]. For large separation gaps the longitudinal dimer resonance progressively approaches the surface plasmon resonance of the constituent nanoparticle.

We can observe Figure 4.4a a significant decrease of the absorption cross-section in the range of 1 to 10 nm of gap. This result and the observed decrease of the redshift in Figure 4.3 points out a possible separation limit in which the selective excitation of a dimer resonance would be effective. We calculated the contrast at the respective dimer resonance for each separation, illustrated in Figure 4.4b, and observed that for separations above 10 nm the contrast becomes smaller than 0.8. Note that the contrast drops with increasing separation, indicating an overlap between the absorption cross-sections of the dimer and the constituent nanoparticle.

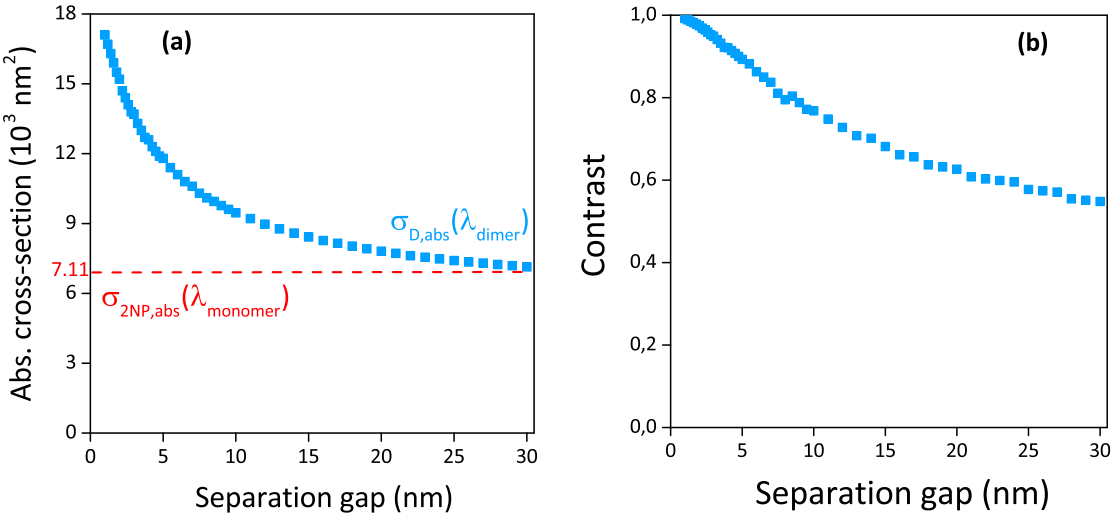

Figure 4.4: Effect of separation gap in the absorption and contrast at the dimer resonance. The absorption cross-section for the longitudinal mode of 20 nm radius gold nanoparticle dimer in a dielectric with refractive index $n = 1.33$ were calculated with FDTD for separation gaps between 1 nm and 30 nm. (a) The absorption at the dimer resonance is plotted against the separation gap. (b) The contrast is evaluated using the eq. 4.1 at the dimer plasmon resonance for the absorption cross-section of the monomer and dimer.

For separation gaps below 10 nm, the contrast remains essentially linear, although we would expect a non-linear increase, considering the increase in the redshift and the absorption at the dimer resonance of Figure 4.4a and Figure 4.3. This linearity is result of the separation dependence of the absorption cross-section in the dimer. The force F between punctual electric charge depends on the square inverse of the distance, i.e. $F \propto 1/d^2$ where d is the separation. In the dimers the electromagnetic interaction is more complicated, as is an interaction between the surface charges of the spheres. However, we expect a dependence $1/d^n$ where n is a positive number. We analyzed the absorption cross-section at the dimer resonance and found $n \approx 0.3$. For mathematical expressions such as $1/d^n$, the reciprocal, d^n, is linear for small increases in d when d is large. As the contrast equation 4.1 is defined with the reciprocal of the absorption cross-section, this explain the observed linear trend.

4.3.3 Effect of nanoparticle size

The studies related to the separation of nanoparticles are useful in providing insights on how to tailor dimerization of nanostructures. However, metal nanoparticles in solution, are typically coated with ligands in order to impart stability and prevent their aggregation and subsequent precipitation[12][65]. Such surface ligands may impart stability to the nanoparticle either via electrostatic repulsion or via steric repulsion[13][65]. The presence of ligands, however, imposes a significant constraint on the minimum nanoparticle separation that can be attained, and it is therefore an important aspect that needs to be taken into account in our assembly strategy.

Polyethylene glycol (PEG) is a commonly used organic polymer to stabilize nanoparticles in aqueous and polar solutions via steric repulsion[66]. The capping of colloidal nanoparticles with PEG, increases the hydrodynamic radius of the nanoparticles from 2 nm to 20 nm, depending on the capping agent's molecular weight. On the basis of the contrast calculated and illustrated in Figure 4.4, the separation gap should be as small as possible. However, there a thin coating of PEG can result in particle aggregation and therefore, we considered a PEG coating of 5 nm, which is experimentally attainable. This coating gives a separation of 10 nm, which is still in the region of high contrast.

In order to optimize the absorption cross-section and the contrast of the dimer, we performed simulations in which varying the nanoparticle radii was varied from 10 nm to 35 nm. Figure 4.5a compares the size dependence in the dimer's absorption cross-section (blue data) with the absorption cross-section of the individual nanoparticle (orange data) evaluated at the longitudinal resonance. We note the presence of a maximum around a size range of 31-34 nm. The observed size dependence is characteristic of the multipole modes in localized surface plasmons. In Mie theory, the scattering coefficients that define the absorption cross-section are function of the nanoparticle radius [29]. Therefore, as the dimer resonances are result of the coupling between the individual localized surface plasmons, such size dependence is also present in the dimer. In the hybridization theory, the size dependence determines the surface charge distribution. The strength of the electromagnetic interaction is determined on the surface charge density of two nanoparticles, and thus the hybrid plasmon exhibits a dependence with nanoparticle size.

The contrast illustrated in Figure 4.5b is evaluated at the dimer resonance that corresponds for each nanoparticle size. Note the presence of a maximum as a function of size, around the radius range of 26-28 nm. Note that the maximum in the contrast does not coincide exactly with the peak in the absorption cross-section shown in Figure 4.5a. Observing the orange data for the absorption cross-section of the single nanoparticle, which exhibits a linear trend, it can be understood why the peak in the contrast is present at smaller radii.

[12]Nanoparticles have a high area to volume ratio, which results in a high surface energy[64]. When two nanoparticles without any capping ligands collide, aggregation follows as the new particle reduces its surface energy.

[13]Steric repulsion or steric hindrance is caused by electron repulsion when atoms of different molecules are in close in proximity.

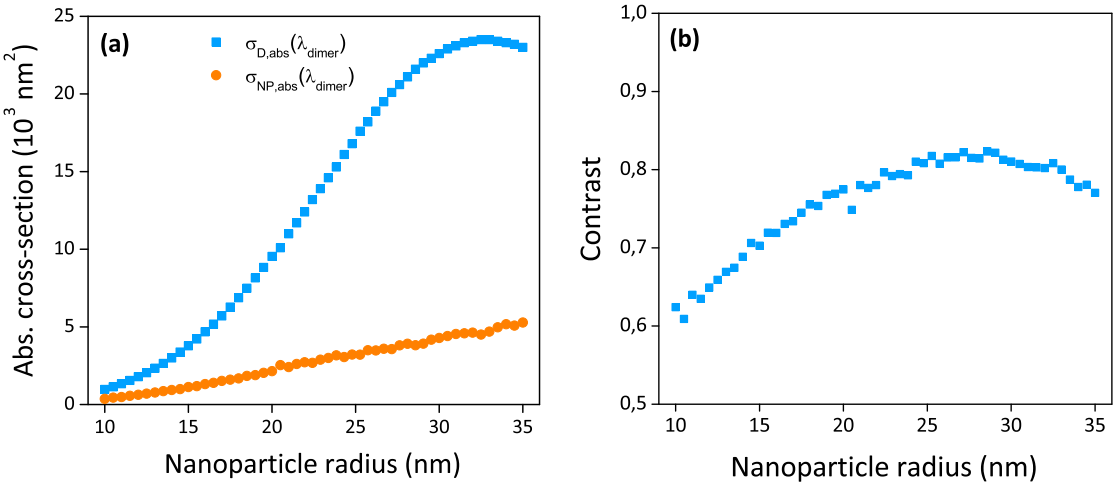

Figure 4.5: Effect of nanoparticle size in the absorption and contrast at the dimer resonance. The absorption cross-section for the longitudinal mode of 10 nm gap gold dimers of different size in a dielectric with refractive index $n = 1.33$ were calculated with FDTD. The nanoparticle radius was varied between 10 nm and 35 nm. (a) The absorption at the dimer resonance is plotted against the nanoparticle radius. (b) The contrast is evaluated using the eq. 4.1 at the dimer plasmon resonance for the absorption cross-section of the monomer and dimer.

4.3.4 Effect of nanoparticle composition

So far we have only studied gold, mainly because it is very stable in solution while having a suitable dielectric function. However, the imaginary part of the dielectric function of gold is responsible for the broad resonances observed in the simulations, limiting the contrast to $c(\lambda) \approx 0.8$. Silver, on the other hand, has less losses at optical frequencies[37], resulting in sharper plasmon resonances, and hence better selectivity in our assembly strategy. The main drawback of silver nanoparticles is that they are more prone to oxidation than gold and the functionalization of their surface is generally more challenging. Nevertheless, it is worth to investigate the contrast that we could obtain, assuming that the chemical instability could be overcome.

Using our numerical FDTD approach, we calculate the absorption cross-sections of silver dimers for a fixed separation of 10 nm, varying the radius in range of 10 to 40 nm (Figure 4.6). We found two different dimer resonances. According to the hybridization theory as the separation is reduced for the longitudinal mode, localized surface plasmons of different angular moment l can couple/hybridize to produce dimer plasmon modes[33]. In the case of an homodimer, the hybridization theory predicts that the less energetic resonance corresponds to a dimer mode with the lowest angular moment, i.e. the coupling of the dipole modes of the constituent nanoparticles. The low energy mode of the silver dimer is similar to the dimer mode we found for the gold nanoparticle dimer and which was explained within the dipole-dipole interaction model. However, the high energy resonance is described in the hybridization theory as the coupling of the dipole mode of one nanoparticle with the quadrupole mode of the other. Here we followed the notation of Nordlander and termed the low energy

and high energy resonances as $l = 1$ and $l = 2$, respectively[33]. The white dash curve marks the resonance of both modes and it can be noted that $l = 1$ mode vanishes almost completely for radii above 30 nm.

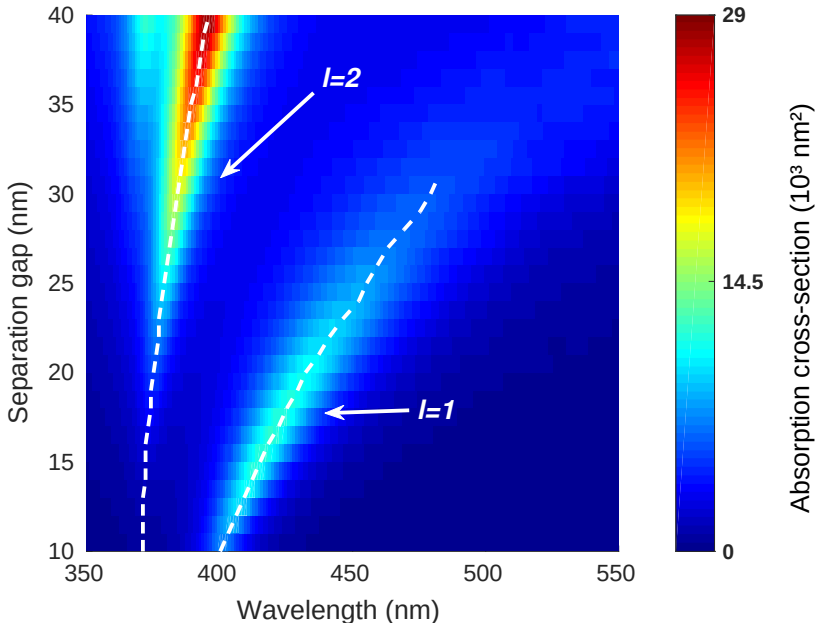

Figure 4.6: Effect of material composition in the absorption cross-section of a dimer. Contour plot of the absorption cross-sections for the longitudinal mode of a 10 nm gap silver dimers of different size in a dielectric with refractive index $n = 1.33$ calculated with FDTD. The nanoparticle radius was varied between 10 nm and 40 nm. Silver nanoparticle dimers exhibit two resonances, a low energy resonance labeled as $l = 1$, and high energy resonance labeled as $l = 2$. The $l = 1$ mode corresponds to the coupling of the individual oscillating dipole modes. The $l = 2$ mode would be due to the coupling of a dipole with a higher multipole, likely a quadrupole.

In Figure 4.7a we plot the absorption cross-section at the dimer resonances for both $l = 1$ and $l = 2$ modes. The dipole resonances of the silver dimer show a similar size dependence than in the gold dimer (Figure 4.5a), which is a consequence of the size effect in the localized surface plasmons of the individual nanoparticles. In contrast with gold, we observe that the material composition leads to a maximum in the dipole mode ($l = 1$) for a nanoparticle size around 15-16 nm. For larger radii, the dipole mode of the silver dimer starts decreasing. For radius above 30 nm, the data is not shown for the dipole resonance because the intensity of the absorption-cross section is comparable to small fluctuations present in the numerical simulation. In the case of the $l = 2$ mode we do not observe a maximum. On the basis of the size dependence of the individual plasmon resonances, we can expect that such maximum must occur at larger radii.

In order to calculate the contrast, we compared the dimer $l = 1$ and $l = 2$ resonances with the two energy resonances of silver particles present in the wavelength range of 350-550 nm, the dipole (low energy) and quadrupole mode (high energy). In contrast with

gold dimers, silver dimer resonances have contrast with both dipole and quadrupole mode of the individual nanoparticle. Excitation of the dimer resonance would result in absorption cross-sections for the dipole an quadrupole in the individual nanoparticle, although with different values. Therefore, we propose that contrast of a dimer mode resonance should be evaluated for the resonance of the individual nanoparticle which has larger absorption cross-section. Such resonance corresponds to plasmon mode that is spectrally closer to the dimer mode resonance considered.

Figure 4.7b shows the contrast calculated for the silver dimer modes. The inlet shows the resonance wavelengths for the plasmon mode with largest absorption cross-section as function of the separation. We note how the transition of low energy mode to the high energy mode as dominant in the absorption cross-section is different for the dimer (dark blue data) and the constituent nanoparticle (red data). It can be seen that when the transition happens for the dimer, from the $l = 1$ to $l = 2$, the spectrally close resonance of the individual nanoparticle is the quadrupole mode.

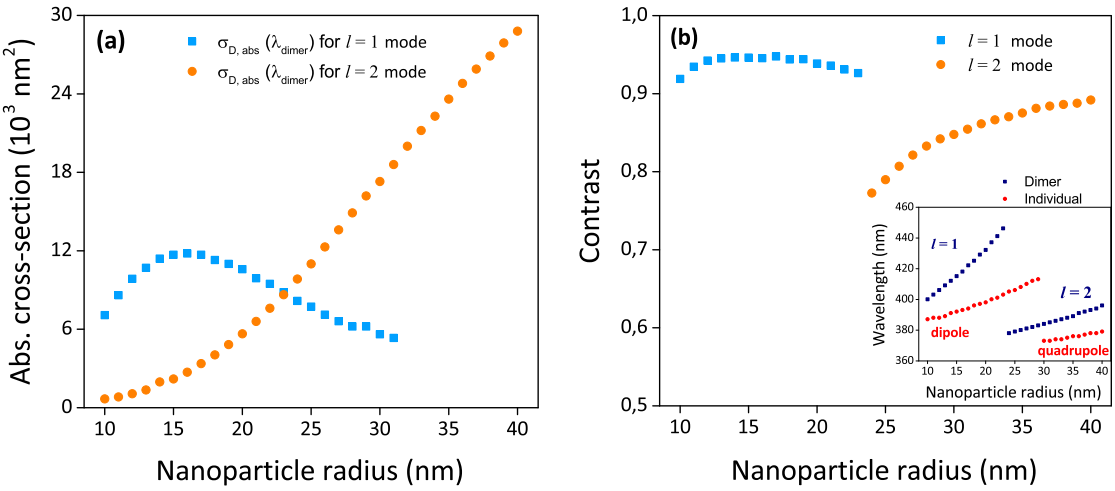

Figure 4.7: Effect of material composition for the absorption and contrast at the dimer plasmon resonance. The absorption cross-sections for the longitudinal mode of a 10 nm gap silver dimers of different size in a dielectric with refractive index $n = 1.33$ were calculated with FDTD. The nanoparticle radius was varied between 10 nm and 40 nm. The absorption at the dimer resonance is plotted against the nanoparticle radius. (b) The contrast is evaluated using the eq. 4.1 at the dimer plasmon resonance for the absorption cross-section of the monomer and dimer.

From the contrast of the silver dimers we note that in the dipole mode this values are very close to one ($C(\lambda) \sim 0.95$). The maximum is broad, and radii in the range of 11-20 nm have very similar contrast values. In contrast, the maximum of the contrast in the gold dimers was around 0.8, indicating that sharper resonances of materials with lower losses lead to higher contrast. From the inlet of Figure 4.7b we note that the redshift between the dimer $l = 1$ mode and the dipole mode of the constituent nanoparticle is larger than the redshift between the dimer $l = 2$ mode and the quadrupole mode. In addition, the absorption cross-section of the individual nanoparticle also increases with size. Therefore we can understand why the contrast for the $l = 2$ mode is smaller

compared with the $l = 1$ mode.

4.4 Discussion

Based on the numerical simulations with FDTD we have found that selective excitation of a nanoparticle dimer is an effective strategy for dimer assembly only for a certain range of sizes in the constituent particles and interparticle separations. The separation is experimentally constrained by the presence of ligands on the surface of the metal nanoparticle, but the nanoparticle size allows us to optimize the dimer resonances to obtain the highest attainable contrast at a given separation. In addition, the simulations with silver composition shows that using plasmon materials with lower losses could provide sharper resonances that increase the contrast. Furthermore, different materials also provide different sizes in which the formation of a dimer can be attained, therefore allowing to study for size effects in the plasmonic assisted chemistry of dimers.

Although stability of silver remains a challenge, our simulations suggest that the excitation of surface plasmon resonances in silver nanoparticle dimer are more selective than in gold nanoparticle dimers.

For this reason, gold is chemically stable in solution and remains as a good candidate for the formation of dimers. Our simulations suggest that better contrast is possible with a smaller gap, i.e. shorter ligands on the surface of the gold nanoparticles. However, there is a limit to the thickness of the ligands, as too shorts ligands would result in unstable nanoparticles that would aggregate and subsequently precipitate. Consequently, there must a trade-off between the strength of the coupling, and hence the contrast, and the stability of the nanoparticles in solution.

The proposed strategy of designing optical resonances around the concept of contrast can be applied to obtain a high degree of control in the excitation of the surface plasmon resonance for a particular aggregate of interacting nanoparticles. Notably, the optimization process should be done around the size and material of the aggregate, so that the highest possible contrast is obtained. Such control of which particles are excited in the solution would give control over the esterification reaction, or any other temperature-sensitive reaction.

In the present section we have focused on calculating the absorption cross-sections of nanoparticle dimers of different sizes and compositions, as in our assembly strategy we envision the use of photo-thermal heating which directly depends on σ_{abs}. However, dimerization of nanoparticles could also be driven by photo-sensitive reactions, such as 2-photon polymerization reactions, which could be triggered by the electromagnetic fields in the dimer gaps. Our strategy of using contrast can also be applied for this polymerization reaction, in which the contrast would be calculated comparing the intensity of the electric field for the hot-spots, regions of high electric field intensity, of dimer gap and the nanoparticle. This approach would have the additional advantage of using a non-linear process which could boost the contrast parameter in the assembly strategy.

5 Localized heating as a strategy for the assembly of dimers

5.1 Introduction

Owing to the nanometer size of the nanoparticles, plasmon-induced heating allows unprecedented control of the temperature at the nanoscale[42, 47]. As such, the use of nanoparticles as sources of heat has attracted attention for applications in chemical reactions, phase transitions, material growth, photothermal cancer therapy and biosensing.

To our knowledge, plasmon-induced heating has not been used to drive a chemical reaction that assembles nanoparticles in solution. A study by González *et al.*[61] reported that exciting the resonance of self-assembled nanorod trimers with a femtosecond laser, the heat generated was able to break the trimer, so the yield of dimers was increased. The concentration of dimers showed a dependence with the pulse fluence of the used.

Our strategy consists on the reverse, i.e. employing heat to form assemblies, not to break it. We propose as reaction for the dimerization of nanoparticles the esterification of the carboxyl groups attache to the polyethylene glycol (PEG) molecules with the ethylene glycol, which is the solvent of our nanoparticle soulution. Since the reaction rate is temperature dependent, we investigate the thermal response of nanoparticle dimers and the extent to which temperature effects allow us to control their assembly in solution. On the basis of the results of González *et al.*[61], the temperature control seems to be essential for a high yield of nanoparticle dimer formation. We hypothesize that if the thermal response is not selective, assembly of nanoparticles to form structures others than dimers could result in low yield of dimer formation. Due to plasmon coupling in nanoparticle dimers, section 4 showed that selective excitation of the localized surface plasmon resonance of dimers was possible. Such coupling results in redshifted resonance compared with the constituent individual nanoparticle and hence a different thermal response can also be expected.

We numerically solve the heat diffusion equation 2.19 using DEVICE, a software that implements the Finite Element Analysis (FEM) to approximate solutions of partial differential equations. The size of the nanoparticle for the dimer was considered according to the size effect observed in the last section. Specifically, in the rest of this section we simulate the temperatures generated by 34 nm radius gold dimers coated with 5 nm of PEG, suspended in a solution of ethylene glycol at an ambient temperature of 300 K. Compared with water, PEG and ethylene glycol have refractive indices of $n_{=}1.43$ and $n = 1.45$ respectively[14]).

Following the methodology of section, the absorbed power density, $q_{abs}(\mathbf{r})$, at the the dimer resonance, was calculated from the simulated electric field inside the dimer, using eq. 2.15. Subsequently, $q_{abs}(\mathbf{r})$ is used as input in the software DEVICE, and the boundary conditions are set as the ambient temperature of the solution before the irradiation of the nanoparticles, i.e. *Neumann boundary conditions.*

[14]The precise value of the refractive index depends on the molecular weight of the PEG molecule[67].

5.2 Thermal response of nanoparticle dimers

The temperature increase by plasmon-induced heating depends on the irradiation intensity, as the absorption cross-section is fixed by the wavelength of the irradiation source, typically a continuous-wave laser. We found a linear dependence between the temperature and the irradiation intensity for individual nanoparticle and the dimers. We consider an intensity of 0.5 mW/μm^2, so the plasmon-induced heating by the dimer leads to a temperature of 100 ℃. This temperature is below the boiling point of ethylene glycol, set at 197 ℃ for atmospheric pressures.

As a first step we used our numerical approach to simulate the plasmon-induced heating of dimers and individual nanoparticles irradiated at the dimer resonance. The reaction rate of esterification is temperature-sensitive and therefore the efficiency of our assembly strategy is determined by the selective in the temperature generated by the dimers compared with the individual particles.Figure 5.1 illustrates the spatial distribution of the temperatures generated by the constituent nanoparticle and the dimer for their equatorial planes. The nanoparticles are identified with the black circles in the contour plots. The interparticle separation in the dimer is of 10 nm, and therefore the PEG ligands are in contact.

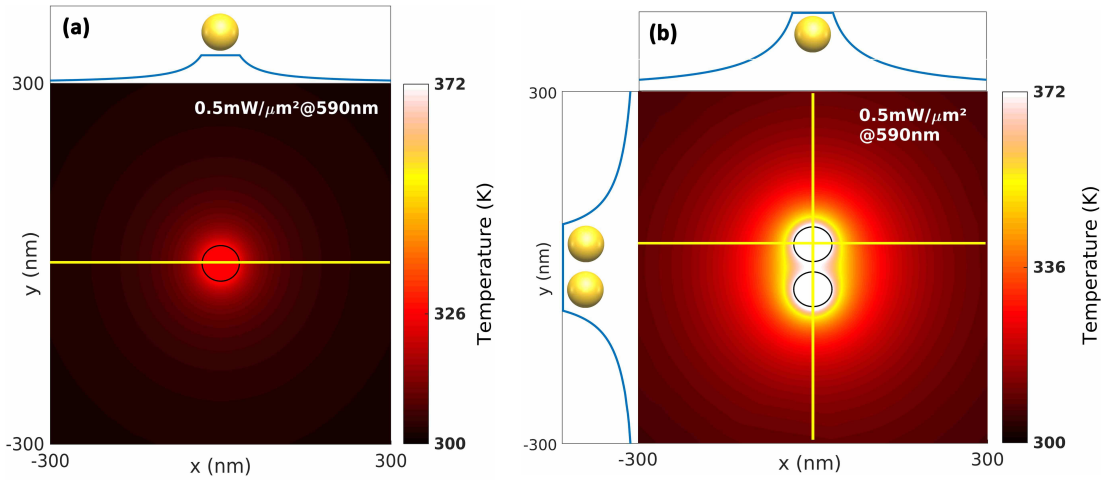

Figure 5.1: Contour plots and spacial profile of temperatures for dimer and nanoparticle. The contour map is illustrated for equatorial plane of the dimer and the constituent nanoparticle. The temperature spatial profile is shown for the constituent nanoparticle in the top of the contour plot for the axis of symmetry, and for the dimer in the top and the right of the contour plot for the two axes of symmetric. (a) FEM simulation of the temperature increase for the constituent nanoparticle, i.e. 34 nm radius gold nanoparticle capped with 5 nm of PEG. (b) FEM simulation for a 34 nm radius gold nanoparticle dimer capped with 5 nm of PEG and a gap of 10 nm, i.e. PEG is in contact for both particles. The solvent simulated was ethylene glycol. The ambient temperature is set at 300 K (27 ℃). The absorbed power density q_{abs} for the dimer and the constituent nanoparticle was calculated with FDTD, modeling PEG and ethylene glycol as dielectrics with refractive index $n = 1.45$. The particles were irradiated with a 590 nm plane wave, polarized along the y axis, with an intensity of 0.5 mW/μm^2, coinciding with the dimer resonance for the longitudinal mode.

The poor conductivity of the PEG and ethylene glycol is responsible of heat accumulation in the metallic particle, which is the hottest spot in the solution. Besides, both figures show that temperature is uniform across the nanoparticle. Baffou and Rigneault showed that this result is consequence of the faster thermal relaxation in metals (eq. 2.18)[48].

We studied the spatial evolution of the temperature for the axes of symmetry of the individual nanoparticle and the dimer, which are represented by the yellow lines if Figure. For a single nanoparticle, the temperature should decrease with a $1/r$ dependence, where r is the distance to the nanoparticle center. This statement is derived from the fact that the steady-state heat diffusion equation 2.19 is mathematically equivalent to the Poisson's equation[47]:

$$\textit{Poisson's equation}: \nabla^2\varphi = f \tag{5.1a}$$

$$\textit{Heat difussion equation}: \nabla^2 T(\mathbf{r}) = \frac{q_{abs}(\mathbf{r})}{k(\mathbf{r})} \tag{5.1b}$$

where φ is a function, such as the temperature $T(\mathbf{r})$, or the electrostatic potential, and f is, from a physics perspective, a source, such as the adsorbed power density $q_{abs}(\mathbf{r})$ or the electric charge. In any case, when the source is constant and has spherical symmetry, the solution to the Poisson's equation has an inverse dependence with the distance to the source.

Our simulations agree with the temperature generated at the surface of the nanoparticle, i.e. when $r = R$ in the analytical solution. However, the spatial evolution of the temperature for individual nanoparticle does not follow a $1/r$ dependence. Neither does it in the case of the dimer, for which we also expect a $1/r$ dependence, as for distances $r \gg R$ the heat generation could be approximated as point source.

One possible explanation for this discrepancy may be due to the chosen boundary conditions. Poisson's equations assumes the boundary to be at infinite distances, while calculating the thermal equilibrium. However, in our calculations, the simulation boundaries are placed at finite distances. There is a trade-off between the boundary conditions and the accuracy of the simulation. A large simulation volume would lead to a more accurate result, but at the expense of longer in the simulation times.

The strong absorption of the dimer results in a surface temperature increase of 72 K, while the surface temperature increase in single nanoparticle is of 26 K only. The ratio of these temperatures is approximately 2.7. In contrast, the absorbed power of the dimer is 4 times greater. However, the contrast is $C(\lambda) = 1 - \sigma_{NP,abs}(\lambda)/\sigma_{D,abs}(\lambda) \approx 0.8$, which implies that absorption cross-section of the dimer is 5 times greater than for the constituent nanoparticle at the dimer resonance. Compared to the individual nanoparticles, dimers have twice the volume, which explains a lower temperature than expected from the absorbed power. As such, this means that the thermal selectivity of the dimer resonance is always lower than the optical selectivity.

The polarization of light also affects the heat generation in dimers[47], as they exhibit plasmon resonances for the transverse and longitudinal mode. The excitation of a particular mode depends on the incident electric field orientation with respect

the axes of symmetry. We observed in the extinction cross-section calculated in Figure that both modes have different cross-sections, which leads to different absorbed powers. Consequently, the thermal response is affected by the polarization state of light [47, 68].

We compared the heat generated by the two modes of a dimer, excited at the resonance of the longitudinal mode. Figure 5.2 illustrates the spatial distribution of the temperatures generated by the transverse mode and the longitudinal mode at their equatorial planes. The nanoparticles are identified with the black circles in the contour plots. The interparticle separation in the dimer is of 10 nm, and therefore the PEG ligands are in contact.

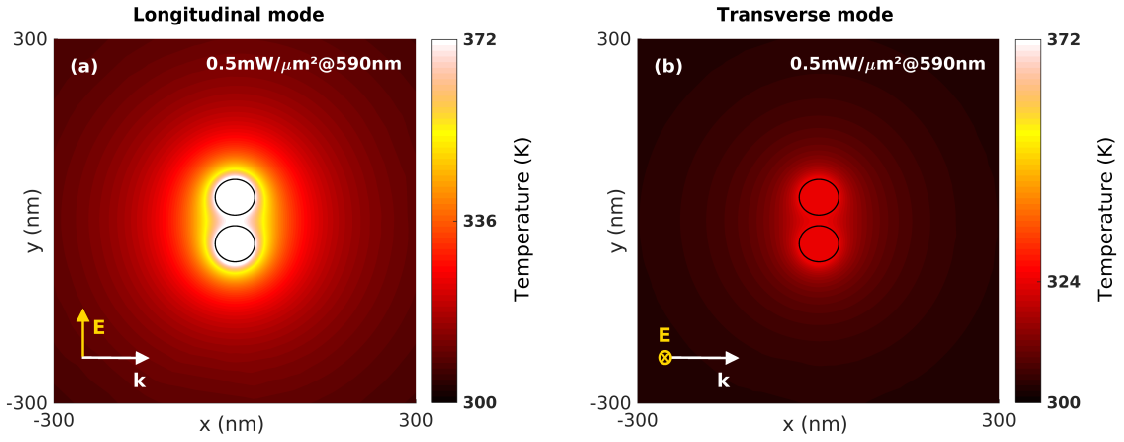

Figure 5.2: Contour plots of temperatures for the longitudinal and transverse modes of a dimer. The contour map is illustrated for equatorial plane of dimer for both modes. (a) FEM simulation of the temperature increase for the longitudinal mode of a 34 nm radius gold nanoparticle dimer capped with 5 nm of PEG. (b) FEM simulation for the same dimer and excitation of the transverse mode. The solvent simulated is ethylene glycol. The ambient temperature is set at 300 K (27 ℃). The absorbed power density q_{abs} for the dimers was calculated with FDTD, modeling PEG and ethylene glycol as dielectrics with refractive index $n = 1.45$. The dimers were irradiated with a 590 nm plane wave, with an intensity of 0.5 mW/μm^2, coinciding with the dimer resonance for the longitudinal mode. The plane wave is polarized along the y axis to excite the longitudinal mode (a) and polarized along the z axis to excite the transverse mode (b).

When the polarization is perpendicular to the longitudinal axis of the dimer, the temperature increase is of only 24 K; confirming the influence of the coupling strength with the polarization of light. Note that the temperature increase of the transverse mode is lower compared with the constituent nanoparticle. Due to the blue-shift of the transverse mode the intensity of the absorption cross-section decrease with respect the sum of the absorption cross-sections of two isolated constituent nanoparticles, which leads to a smaller absorbed power and a lower temperature.

5.3 Effect of separation gap in the thermal response

Nanoparticles suspended in a solution undergo Brownian motion, simply because of their thermal energy, and as result the gap between two nanoparticles fluctuates continuously. In the previous section 4.3.2 we found that the redshift of the longitudinal dimer resonance with respect the plasmon resonance of the individual particle decreases as a function of the separation. Therefore, dimer with gaps that vary from 10 nm, i.e. minimum separation, to several tens of nm where the plasmon coupling is weak also have a thermal response when they are irradiated at the dimer resonance of a 10 nm gap dimer.

We asked ourselves how the temperature distribution and the profile changes as function of separation gap. Figures 5.3 a-f show the spatial distribution of the temperatures generated by nanoparticle dimers and different separation gaps. It can be seen the effect of increasing separation in the temperatures added in the scale bar next to each graph. We observe that as the separation gap increases, the drop in the temperature decreases in value. For example from Figures 5.3a to Figures 5.3b the gap increases by 15 nm and the temperature at the nanoparticle surfaces drops by 28 K, but from Figures 5.3c to Figures 5.3d a further increase of 10 nm only drops the temperature by 3 K. Note that finally, for Figures 5.3e-f there is no seeming drop in the temperature.

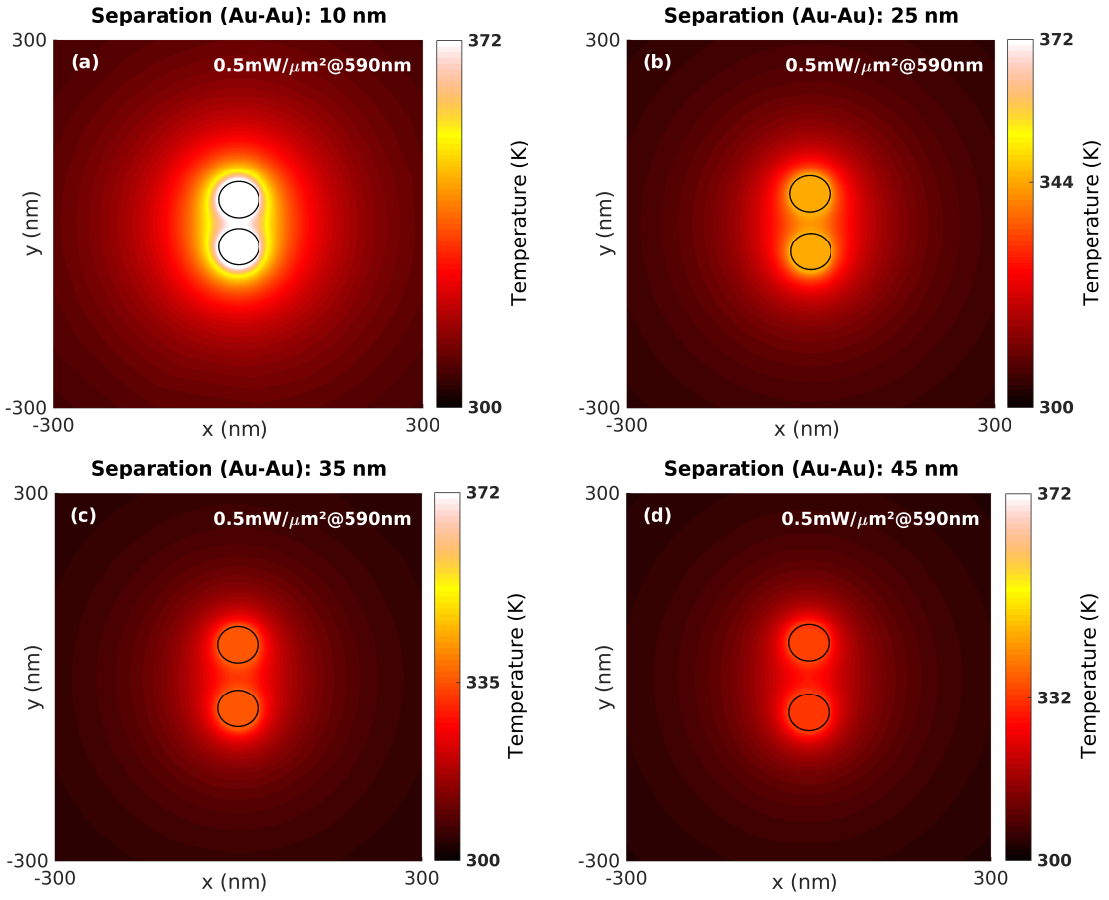

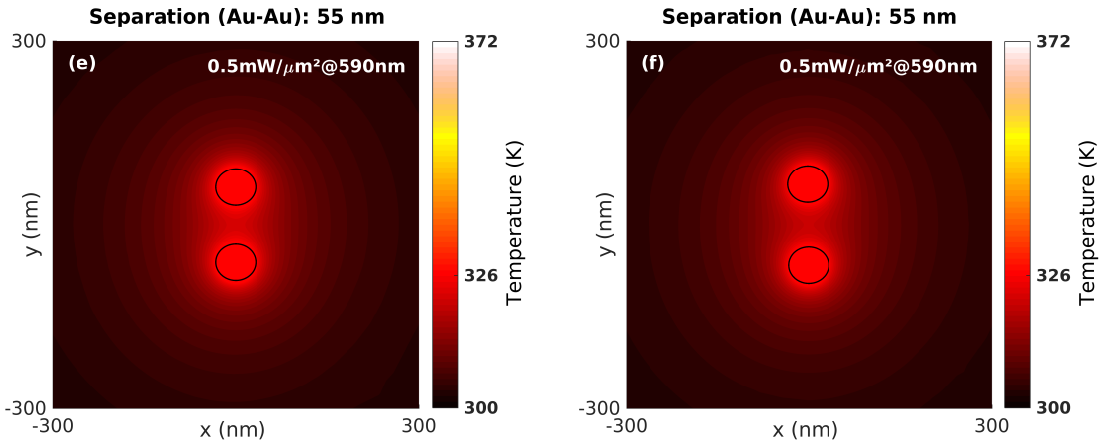

Figure 5.3: Effect of separation gap in the temperature increase generated by the longitudinal mode of a dimer. For each separation gap, the contour map is illustrated for equatorial plane of dimer. (a-f) FEM simulation of the temperature increase for the longitudinal mode of 34 nm radius gold nanoparticle dimers capped with 5 nm of PEG. The separation gap was increased from 10 nm (a) to 65 nm (f). The solvent simulated is ethylene glycol. The ambient temperature is set at 300 K (27 ℃). The absorbed power density q_{abs} for the dimers was calculated with FDTD, modeling PEG and ethylene glycol as dielectrics with refractive index $n = 1.45$. The dimers were irradiated with a 590 nm plane wave, polarized along the y axis, with an intensity of 0.5 mW/μm^2, coinciding with the dimer resonance for the longitudinal mode.

We also observe in Figures 5.3a-f that the highest temperature increase in the solvent is located in the separation gap. This "hot-spot" is essential in our proposed strategy for the esterification, since a molecule of ethylene glycol can bond with the PEG molecules of both nanoparticles, forming a bridge that ties the two nanoparticles together.

Following the results illustrated in Figures 5.3a-f we asked ourselves how the temperature in the gap and in the surface of the nanoparticle changes with separation. Figure 5.5 shows that the temperature at the center of the gap is similar to the overall temperature of the individual nanoparticle that form the dimer for distance below ~ 25 nm. The line of straight data represents the temperature increase of a single nanoparticle, revealing that as the separation increases the temperature generated by the dimer tends towards the temperature increase of individual uncoupled nanoparticles.

To understand better the trend of the temperature decrease as a function of the separation gap we calculate the *heat generation efficiency*, i.e. the ratio of absorbed power to incident power, for the dimers with a range of gaps between 10 nm and 65 nm (Figure 5.4a). The heat generation efficiency indicates a decrease similar to the temperature decrease plotted in Figure 5.5.

The heat generation efficiency is an useful tool to study the thermal selectivity of the dimer as function of the irradiation wavelength because it is independent of the temperature and of the irradiation intensity. Figure 5.4a allows for a clear interpretation that at the dimer resonance, plasmon-induced heating is generated more

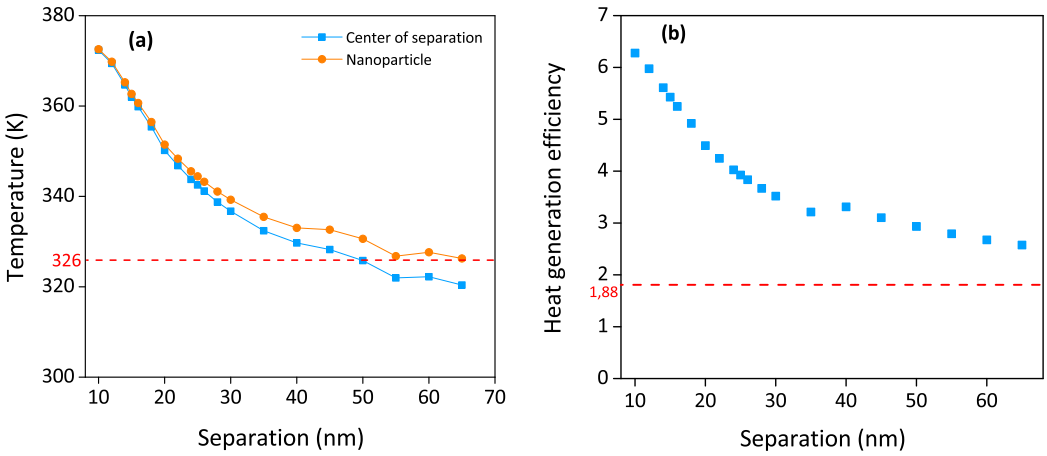

Figure 5.4: Effect of the separation gap in the temperature generated in the nanoparticles and in the hot-spot of the solvent (a) and in the heat generation efficiency (b). The power absorbed is calculated using FDTD for nanoparticles dimers of 34 nm radius coated with 5 nm of PEG and immersed in ethylene glycol, varying the separation gap between the nanoparticles. The electric field polarization is along the longitudinal mode. The dimers are irradiated with a plane wave of 0.5 mW/μm^2, and wavelength of 590 nm, coinciding with the dimer resonance for the longitudinal mode. In **(a)** the absorbed power is used in the FEM software to simulate the temperature increase at the nanoparticle and in the center of the separation gap, i.e. the hot-spot of the solvent. The ambient temperature is set at 300 K (27 ℃). The heat generation efficiency in **(b)** is calculated as the ratio of the absorbed power obtained from FDTD to the incident intensity, i.e. the irradiation intensity multiplied per the geometric area of the dimer ($2\pi r^2$).

efficiently for separations compared to that of the resonant dimer, i.e. a 10 nm gap. The red straight line is the heat generation efficiency of the constituent nanoparticle. The the ratio of the constituent to the dimer generation efficiency can be maximized in analogous fashion to the contrast to look for optimum selectivity of our assembly strategy.

When we analyzed the heat generation efficiency in detail we found a linear relationship between the temperature and the absorbed power, i.e. the volume integral of $q_{abs}(\mathbf{r})$. Figure 5.4b shows the evident linearity of the temperature increase against the absorbed power. Each value for the absorbed power represents a different separation gap, which is represented in the upper axis. We noted that such linear dependence is consequence of the Poisson's equation, which a linear differential equation. A change in $q_{abs}(\mathbf{r})$ results in a directly proportional change in the temperature $T(\mathbf{r})$.

Notably, Figure 5.4b can be used as a frame of the possible temperatures generated by a solution of monodisperse nanoparticles of a certain size, material composition, coating for a given irradiation intensity and wavelength. Aggregates larger than dimers are not included, but in base of Brownian motion, the frequency of collision for n particles decreases non-linearly with n. We observe in Figure 5.4b that large separations are concentrated at low powers, as there is a limit to the minimum power absorbed, and hence minimum temperature that can be generated, that of non-interacting individual

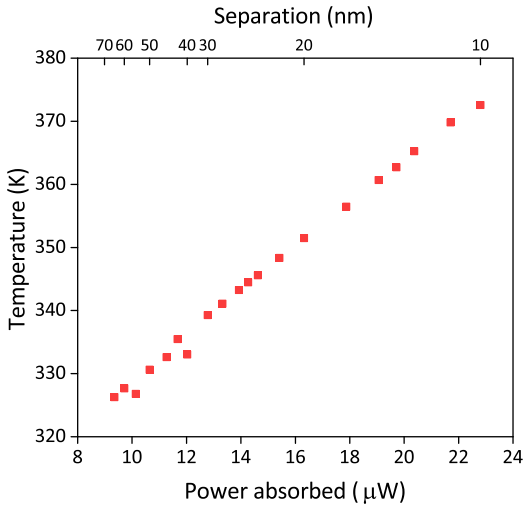

Figure 5.5: Linear dependence of the temperature as a function of the power absorbed (lower x axis) by the nanoparticle dimers. The power absorbed is calculated using FDTD for nanoparticles dimers of 34 nm radius coated with 5 nm of PEG and immersed in ethylene glycol, varying the separation gap between the nanoparticles. The electric field polarization is along the longitudinal mode. The dimers are irradiated with a plane wave of 0.5 mW/μm^2, and wavelength of 590 nm, coinciding with the dimer resonance for the longitudinal mode. Such quantity is used in DEVICE to simulate the temperature increase at the nanoparticle, which is plotted against the absorbed power. The ambient temperature is set at 300 K (27 ℃). The upper axis shows the separation gaps, which is non-linear and shows the collapse of large separation gaps since there is a minimum power and temperature that can be generated for the given irradiation intensity, that of two non-interacting nanoparticles.

particles. In addition, there is a limit to the maximum power that can be generated, that of the dimer for the smallest gap.

5.4 Discussion

The thermal simulations indicate that the thermal selectivity of the dimer resonance is lower than the optical selectivity. We explained that this is due to larger volume of the gold nanoparticle dimer compared with the individual constituent nanoparticle. Better results could be expected if the dimer had a smaller separation. This would remain a challenge, requiring stable short ligands in which esterifacation reactions are possible. It is worth mentioning that at the group of dr. Andrea Baldi at DIFFER we are currently changing ligands to shorter ones and studying the stability of the nanoparticle in solution.

Whether this lower selectivity is a barrier or not depends on the experimental results. As such, one could measure the dimer yield as a function of the thermal selectivity, as defined with the heat generation efficiency.The yield of dimers is equivalent to the concentration of dimers in solution, which is typically measured from optical density in a solution by using the Beer-Lambert law. As the dimer concentration increase, the optical density at the irradiation wavelength would increase (the individ-

ual nanoparticles have negligible absorption and scattering at the dimer resonance). If there is an empirical relationship, then employing our strategy would allow us to optimize the dimer yield.

Parallel to experiments, we consider that study of the Brownian dynamics could help us estimate and optimize the yields of dimers. Brownian motion leads to collision events between the nanoparticles. According to literature, the *collision rate frequency* per unit volume between identical hard spheres is determined by their concentration n, the dynamic viscosity of the solvent η, the temperature of the solvent T and the Boltzmann's constant k_B, so $f = (4k_BT/3\eta)n^2$[69]. Considering a temperature of 25 ℃, the dynamic viscosity of ethanol ($\eta = 0.0162$ Pa s), and a nanoparticle concentration of $n \propto 10^{16}$particles/m^3, we found a collision frequency per unit volume of $f \propto 10^{13}$ collisions/s/m^3. This is the overall frequency collision of the whole solution. In contrast, each single nanoparticle has a collision frequency $f_{NP} = (4k_BT/3\eta)n = 0.0032$ collisions/s.

The previous paragraph indicates that with higher concentrations we would obtain a higher collision frequency. If dimers are formed, we can formulate an assembly frequency rate, introducing an *sticking coefficient* $\alpha(T)$ which depends on the temperature. The sticking parameter introduces a probability of esterification when two particles collide. Consequently, we are formulating a time dependent problem, as now the concentration is a function of time. The decrease in nanoparticle concentration is related with the dimer yield. It is logical to assume that the sticking probability would depend on the reaction rate and in the speed of the particles. The reaction rate of dimer formation can be inferred from empirical observation of the dimer yield as a function of time. We hypothesize that if the reaction rate is slower than the velocity of the nanoparticles, the particles will separate apart as the the esterification needs a longer time to stick the particles together.

In conclusion, the sticking coefficient, together with Brownian dynamics of colloids and our strategy for selective excitation of the dimer resonances could provide an efficient approach for the increase in the yield of dimers. In addition to esterification, this approach can also be applied to the discussed 2-photon polimerization with a reaction rate that depends now on the irradiation source intensity. As the reaction rate is determined by the dimer resonance and the chemical reaction used, playing with the concentration, solvent temperature and solvent viscosity would allow to optimize the dimer yield.

6 Design and assessment of plasmon-assisted chemical reactors

6.1 Introduction

Designing better catalysts is of paramount importance for efficient chemical processes that require less energy consumption[18, 16]. A catalyst is an entity that accelerates a chemical reaction without being consumed in the process[70]. The increase of the reaction rate by the catalyst is called *catalytic activity*. For a chemical reaction with multiple products, a catalyst may promote the production of one of the products, referred to as *catalytic selectivity*. Catalysis, specially heterogeneous catalysis, is a fundamental part of the economy, contributing to nearly 35 % of the global gross domestic product[18, 71]. An ideal catalyst would improve the conversion rate of the desired product while minimizing the formation of any competing byproduct. Catalysis is considered a foundational pillar in the design of chemical products and processes that reduce or eliminate the use and generation of hazardous substances, i.e. green chemistry[72]. From an environmental point of view, efficient catalysts may help reduce the energy consumption and waste generation of the chemical industries[16, 73].

Most heterogeneous catalysts are solid materials, which involves reactants in gas or liquid phase. The reactions occur at the interface between the two phases, i.e. at the surface of the solid. Catalysis occurs because when the reactants adsorb in the catalyst surface, their chemical bonds are weakened or even broken so new bonds can form[71], i.e. the activation energy for a product is lowered. After the product is formed, the bonds with catalyst surface are weaker, and the molecule desorbs. Progress in heterogeneous catalysis over the last decades has been the result of extensive research in surface science and in nanotechnology applied to catalysis[16]. The effect of the surface in the reaction depends on catalyst properties such as the material composition, size, shape and exposed crystallographic facet. In addition, it has been found that when materials are reduced to a nanometer dimension, their chemical properties are modified drastically, becoming more chemically active compared with the bulk material[74].

One of the most recent and exciting developments in nanotechnology applied to catalysis has been the discovery that the catalytic activity of metallic nanoparticles can be modified and enhanced by optically exciting their localized surface plasmon resonances[19]. One of the proposed mechanisms that would explain such effect is the decay of the plasmon resonance into so-called *"hot" charge carriers* (electrons and holes) and their injection into molecular adsorbates[20]. These hot charge carriers are very short lived (a few femtoseconds) and if not harvested, eventually lead to an increase of the temperature of the nanoparticle via electron-electron and electron-phonon scattering (100 fs - 10 ns). Such photo-thermal effects can also contribute to an increased catalytic activity of the metal nanoparticles by virtue of the Arrhenius equation[22]. Notable examples of plasmon-enhanced catalysis include the epoxidation of ethylene and propylene, and the hydrogenation of carbon dioxide[24, 25, 26]. These plasmon-enhancement effects open the exciting prospect of controlling the activity and selectivity of of a catalytic process by tuning the intensity and wavelength of the

incoming light.

However, plasmon-induced catalysis is ever to become relevant for chemical industry, it must offer an economic advantage over the conventional chemical reactors used nowadays[75]. Assessing the economic performance of plasmon-induced chemistry therefore involves designing an hypothetical reactor in which chemical processes are catalyzed when the nanoparticles are illuminated. Here we asked ourselves what are the additional requirements for such plasmonic reactor, what is its economic performance, and what are the main difficulties in terms of design and in terms of costs. Our aim is to provide an insight in the possibilities and barriers that an hypothetical plasmonic reactor could present. Consequently we developed a model to design an hypothetical plasmonic reactor and evaluate its economic performance that could in principle be applied to any plasmon-induced chemical reaction, following the steps described in the methodology section 3.2.

To get insight into the economic performance of an hypothetical plasmonic reactor we decided to apply our model to the study of Marimuthu *et al.*[25], about the effect of illuminated copper nanoparticles in the selectivity of propylene epoxidation. This paper contains sufficient information to solve the design equations 2.24 and it describes the plasmonic enhancement of a catalytic process which is higly relevant in the chemical industry. The production of propylene oxide(PO)[15] consumes every year almost 10% of all the propylene[16], which is an hydrocarbon obtained from cracking crude oil. Between 60% and 70% of all propylene oxide is converted to polyether polyols, which are building blocks in the production of polyurethane plastics. The current production of propylene oxide is by the chlorohydrin and the organic hydroperoxide processes. While the chlorohydrin poses environmental concerns, the hydroperoxide process is dominated by the market value of the co-products and leads to a large amount of waste water. Energy is wasted in this co-products and hence there has been an effort in the last years to synthesize a catalyst which is highly selective to propylene oxide and that reduces the production of byproducts.

The study by Marimuthu *et al.* reported a conversion rate and PO selectivity what were function of the illumination intensity[25]. Propylene (C_3H_6) reacts with molecular oxygen to produce mainly propylene oxide (C_3H_6O), acrolein (C_3H_4O), carbon dioxide and water, as shown in 6.1. Remarkably the authors found a threshold intensity at which the selectivity towards PO is enhanced drastically while the selectivity towards carbon dioxide, a green house gas, drops.

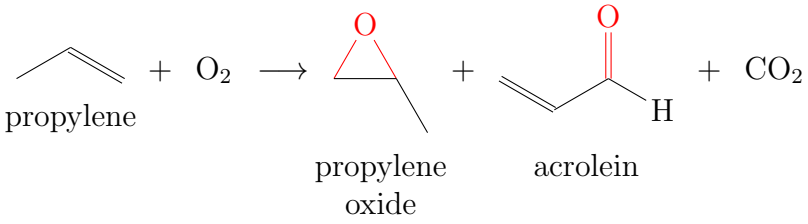

$$+ \; O_2 \longrightarrow \quad + \quad + \; CO_2 \tag{6.1}$$

[15] Also referred as propene oxide, methyloxirane, or 1,2-epoxypropane. For the sake of clarity we will call it always propylene oxide.

[16] Also referred as propene or methyl ethylene. or the sake of clarity we will call it always propylene.

Here we employed their results to derive the design equations and calculate propylene oxide production as a function of the reactor volume. Afterwards we will scale up the design equations to obtain productions and reactor volumes typical of an industrial reactor unit. For such reactor dimensions and production, we will calculated the necessary area for optical activation of the plasmon catalysts, and the economic performance of such reactors. Finally we will compare the plasmonic reactor with a reactor operated in dark conditions (no illumination). Both the plasmonic and the dark reactor are modeled from the data reported by Marimuthu *et al.* for the illumination and no-illumination conditions[25].

6.2 Design of the reactor

Design equations

The first step towards the design of the reactor consists in dividing the chemical reaction 6.1 into its elementary reactions. The elementary reactions depend on the catalyst, and in the case of copper there was no literature found explaining in detail the kinetics pathways of propylene reacting with oxygen on such catalyst. However, several studies that investigated copper as catalyst suggested that the formation of propylene oxide, acrolein and carbon dioxide follow different reaction ways that depend on the oxidation state of the copper surface[25, 76, 77]. Therefore, here we assumed that these three processes are elementary reactions. The complete stoichiometry of each reaction is as follows:

Propylene epoxidation: $$\mathrm{C_3H_{6,g}} + \frac{1}{2}\mathrm{O_{2,g}} \longrightarrow \mathrm{C_3H_6O_{,g}} \tag{6.2a}$$

Acrolein formation: $$\mathrm{C_3H_{6,g}} + \mathrm{O_{2,g}} \longrightarrow \mathrm{C_3H_4O_{,g}} + \mathrm{H_2O_{,g}} \tag{6.2b}$$

Propylene combustion: $$\mathrm{C_3H_{6,g}} + \frac{9}{2}\mathrm{O_{2,g}} \longrightarrow 3\mathrm{CO_{2,g}} + 3\mathrm{H_2O_{,g}} \tag{6.2c}$$

The subindex g indicates that the reactants and products are in gas phase. The presence of water is a product of the propylene combustion and acrolein formation. Although other products are obtained reaction of propylene with oxygen shown in 6.2, the study by Marimuthu *et al.* and of Vaughan *et al.* reported propylene oxide, acrolein and carbon dioxide to be the products in highest concentrations at the outlet of the reactor[25, 76]. The study of Vaughan *et al.* mentions that propylene oxide also reacts with oxygen to form acetaldehyde and propanal and acetone[76]. However, such products are present in very small amounts and we can ignore them in our study. Consequently, we assumed that the products of each elementary reaction do not further react after they are formed.

For each reaction written in 6.2 we derive a design equation following the eq. 2.24. The rates r_m for each chemical reaction can be expressed as the product of the reaction rate constant $k(T)$ and the concentrations of the reactants:

$$r_m = k(T)f(C) \tag{6.3}$$

where $f(C)$ is a function of the concentration of the reactant species. The term $k(T)$ is the rate constant at the temperature T and is given according to the Arrhenius equation:

$$k(T) = k_0 \exp(-E_a/RT) \tag{6.4}$$

where k_0 is the reaction constant, E_a is the activation energy and R is the gas constant.

We have assumed an isothermal reactor, so $k(T)$ is constant. In addition, since each reaction of 6.2 is assumed an elementary reaction, the function $f(C)$ can be expressed as follows[50]:

$$f(C) = [\mathrm{C_3H_6}]^{\alpha}[\mathrm{O_2}]^{\beta} \tag{6.5}$$

where $[\mathrm{C_3H_6}]$ and $[\mathrm{O_2}]$ are the concentration of the propylene and oxygen, and α, β are the so called order of the reaction. For elementary reactions the order of the reaction are identical to the absolute value of their stoichiometric coefficients. However, in general the order of the reaction is an empirical expression.

The concentration C_j of a chemical species is $C_j = F_j/v$ where F_j is the *molar flow rate* and v is the *volumetric flow*. The molar flow rate is function of the conversion extent $\dot{\xi}$ of the reactions in which the chemical species j participates [50]:

$$F_j = (F_{tot})_0 \left\{ y_{j,in} + \sum_{m}^{n_R} (s_j)_m \dot{\xi}_m \right\} \tag{6.6}$$

where for the chemical species j the term $y_{j,in}$ is the molar fraction of the inlet chemicals, $(s_j)_m$ are the stoichiometric coefficients involved in the *mth* reaction for a total of n_R reactions that take place inside of the reactor. The term $(F_{tot})_0$ is the total molar flow rate at the inlet of the reactor, i.e. $(F_{tot})_0 = (F_{\mathrm{C_3H_6}})_0 + (F_{\mathrm{O_2}})_0$. For a gas-phase reaction it can be shown that in a isothermal and isobaric reactor $v = \sum_j F_j/(F_{tot})_0$ [50]. After using eq. 6.6 for the chemical reactants, i.e. oxygen and propylene, and rearranging we obtain the concentrations:

$$C_j = C_0 \frac{(F_j)_0 + \sum_m^{n_R} (s_j)_m \dot{\xi}_m}{(F_{tot})_0 + \sum_m^{n_R} \Delta_m \dot{\xi}_m} \tag{6.7}$$

where $(F_j)_0$ is the molar flow rates at the reactor inlet, for the chemical reactant species j. The term Δ_m is the sum of all the stoichiometric coefficients involved in the *m-th* reaction, i.e. $\Delta_m = \sum_m^{n_R} (s_j)_m$.

In the reaction of propylene with oxygen we have assumed three reactions, $n_R = 3$ and the reaction extents are for the propylene oxidation, $\dot{\xi}_{\mathrm{PO}}$, the acrolein formation, $\dot{\xi}_{\mathrm{Ac}}$, and the propylene combustion, $\dot{\xi}_{\mathrm{com}}$.

Considering the stoichiometric coefficients of 6.2 and the expression for the concentrations of eq. 6.7 we arrive, after some arithmetic and rearranging terms, to the

design equations of a propylene epoxidation reactor:

$$\frac{d\dot{\xi}_{\mathrm{PO}}}{dV_R} = k_{\mathrm{PO}}(C_0)^{\frac{3}{2}} \frac{\left((F_{\mathrm{C_3H_6}})_0 - \dot{\xi}_{\mathrm{PO}} - \dot{\xi}_{\mathrm{Ac}} - \dot{\xi}_{\mathrm{com}}\right)\left((F_{\mathrm{O_2}})_0 - \frac{1}{2}d\dot{\xi}_{\mathrm{PO}} - \dot{\xi}_{\mathrm{Ac}} - \frac{9}{2}d\dot{\xi}_{\mathrm{com}}\right)^{\frac{1}{2}}}{\left((F_{tot})_0 - \frac{1}{2}d\dot{\xi}_{\mathrm{PO}} + \frac{1}{2}d\dot{\xi}_{\mathrm{com}}\right)^{\frac{3}{2}}} \tag{6.8a}$$

$$\frac{d\dot{\xi}_{\mathrm{Ac}}}{dV_R} = k_{\mathrm{Ac}}(C_0)^{2} \frac{\left((F_{\mathrm{C_3H_6}})_0 - \dot{\xi}_{\mathrm{PO}} - \dot{\xi}_{\mathrm{Ac}} - \dot{\xi}_{\mathrm{com}}\right)\left((F_{\mathrm{O_2}})_0 - \frac{1}{2}d\dot{\xi}_{\mathrm{PO}} - \dot{\xi}_{\mathrm{Ac}} - \frac{9}{2}d\dot{\xi}_{\mathrm{com}}\right)}{\left((F_{tot})_0 - \frac{1}{2}d\dot{\xi}_{\mathrm{PO}} + \frac{1}{2}d\dot{\xi}_{\mathrm{com}}\right)^{2}} \tag{6.8b}$$

$$\frac{d\dot{\xi}_{\mathrm{com}}}{dV_R} = k_{\mathrm{com}}(C_0)^{\frac{11}{2}} \frac{\left((F_{\mathrm{C_3H_6}})_0 - \dot{\xi}_{\mathrm{PO}} - \dot{\xi}_{\mathrm{Ac}} - \dot{\xi}_{\mathrm{com}}\right)\left((F_{\mathrm{O_2}})_0 - \frac{1}{2}d\dot{\xi}_{\mathrm{PO}} - \dot{\xi}_{\mathrm{Ac}} - \frac{9}{2}d\dot{\xi}_{\mathrm{com}}\right)^{\frac{9}{2}}}{\left((F_{tot})_0 - \frac{1}{2}d\dot{\xi}_{\mathrm{PO}} + \frac{1}{2}d\dot{\xi}_{\mathrm{com}}\right)^{\frac{11}{2}}} \tag{6.8c}$$

Equations 6.8a, 6.8b and 6.8c form a system of three ordinary differential equations. To solve it we used MATLAB, which has integrated a set of numerical approximations for this type of differential equations. Once the design equations are solved, we use the eq. 6.6 to plot the molar flow rates of the chemical products at the reactor outlet.

In this thesis we focus on the study by Marimuthu *et al.*[25]. Therefore, the following input data was used in the design equations:

- **Rate of propylene consumption**, depends on the illumination and temperature conditions
- **Mass of the catalyst**: $m_{cat} = 0.24$ mg
- **Selectivities** for propylene oxide, acrolein and carbon dioxide, that also depend on the illumination and temperature conditions
- **Volumetric flow**, at the inlet of the reactor: $v_0 = 100\,\mathrm{cm}^3/\mathrm{min}$
- **Temperature**
- **Pressure**: $P = 1$ atm
- **Irradiation intensity**: $I = 550\,\mathrm{mW/cm}^2$

The molar flow rate was calculated using the relationship $(F_{tot})_0 = C_0 \cdot v_0$ where the concentration is calculated using the gas law $C_0 = P/RT$. The rate of propylene consumption, r_W (μmol/$\mathrm{g_{cat}}$/s), is given as function of the catalyst mass, W, and has to

be transformed into a volume-based reaction rate, r_{V_R}(μmol/s/L), using the following relation:

$$r_{V_R} = \frac{W}{V_R} r_W = \rho_{cat,R}\, r_W \tag{6.9}$$

where $\rho_{cat,R}$ is the catalyst packing density, i.e. the catalyst mass per unit volume of reactor. We made an assumption for the volume of the reactor. On the basis of the commercial laboratory reactor employed, we estimated a reactor volume of 1 cm^3.

The design equations 6.8 were solved and compared for the illumination and dark conditions at the same rate of propylene consumption. Figure 6.1 shows the mass flow (kg/h) at the outlet of reactor products for the illuminated (Figure 6.1a) and the dark reactor(Figure 6.1b), as a function of the reactor volume.

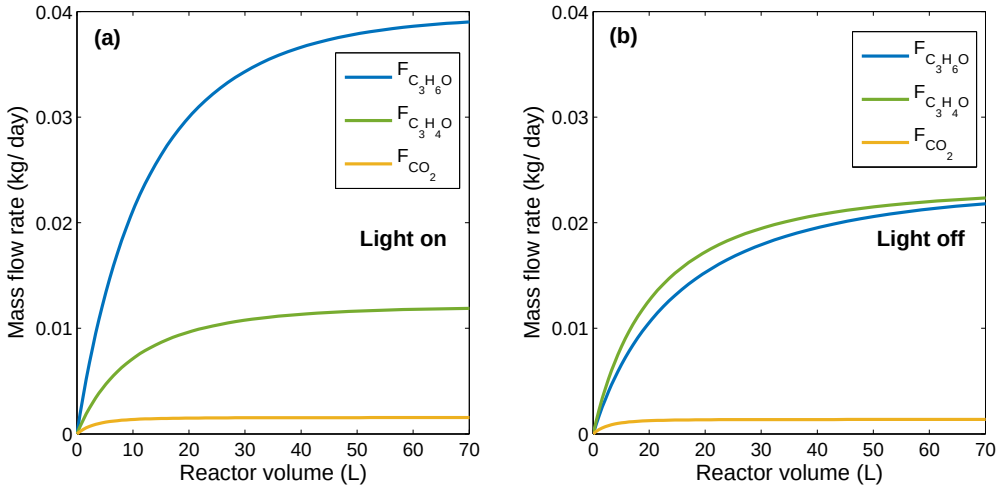

Figure 6.1: Conversion rates of propylene oxide, acrolein and carbon dioxide for laboratory conditions under the same rate of propylene consumption. The conditions of the reactor are **(a)** illumination (light on) and **(b)** dark (light off). The mass flow rates are calculated using the reported data by Marimuthu et *al.* [25]. In particular the reported rate of propylene consumption is $r = 20\,\mu\text{mol}/\text{g}_{\text{cat}}/\text{s}$ for a working temperature of the illuminated reactor **(a)** is $T = 210\,℃$ and of $T = 260\,℃$ for the dark reactor **(b)**. The reported selectivities are different in both cases: $s_{C_3H_6O} = 0.4$, $s_{C_3H_4O} = 0.22$ and $s_{CO_2} = 0.38$ for the illuminated reactor **(a)**; and $s_{C_3H_6O} = 0.2$, $s_{C_3H_4O} = 0.4$, $s_{CO_2} = 0.4$ for the dark reactor **(b)**.

At the same rate of consumption, the production of propylene oxide in the illuminated reactor almost doubles the production of the dark reactor, where the copper nanoparticles are not optically excited. Note that the low production of carbon dioxide is unrealistic. In a real reactor, part of the propylene oxide would also be consumed, resulting in secondary products, especially carbon dioxide. Indeed, at the lab conditions considered the oxygen is not consumed in its totality, and is likely that part of the propylene oxide would react with the excess of oxygen. In particular the combustion of propylene oxide would contribute to an increased production of carbon dioxide. We therefore expect that a realistic reactor would produce less propylene oxide than the one depicted in Figure 6.1.

The effect of secondary reactions with propylene oxide and acrolein is unclear. If the products and the reaction rate constants were known, additional elementary reactions could be added to the design equations 6.8. However, the study by Marimuthu *et al.* neglects secondary reactions as the conversion efficiency is very small in their study[25]. At small concentrations of propylene oxide compared with propylene, the carbon dioxide production will be mainly attributed to the combustion of propylene. With increasing conversion rates, the combustion of propylene oxide would be larger in the illuminated reactor and in the dark conditions, therefore reducing the net production of propylene oxide.

Energy balance

Epoxidation reactions have high activation energies, meaning that energy in the form of heat must be supplied to favor the reaction. Therefore reactors for the epoxidation of alkenes such as ethylene and propylene are operated at high temperatures. The inlet stream of reactants, which is at ambient temperature must be heated to the reactor temperature, by employing electric heaters or furnaces. In addition, the reaction of propylene with oxygen is an exothermic process and consequently, heat is released in the formation of propylene oxide ($\Delta H_r^\circ = -115.09\,\mathrm{kJ/mol}$), acrolein ($\Delta H_r^\circ = -327.64\,\mathrm{kJ/mol}$), and especially in the combustion of propylene ($\Delta H_r^\circ = -2057.7\,\mathrm{kJ/mol}$). If the reactor is not cooled, the exothermic reaction will heat up the reactor. An uncontrolled temperature increase is not desired because it leads to an uncontrolled catalytic activity and in general to increase production of byproducts.

The heat generated by the reaction is proportional to the enthalpy of reaction and the conversion extent of the particular reaction $\dot{\xi}$. The enthalpy of reaction is a function of the temperature and the pressure, and is typically calculated from the standard enthalpy of reaction at 298.13 K (25 ℃) and 1 atm, ΔH_r°. The lab reactor is operated at atmospheric pressure and temperatures higher than 298.13 K. In this case the reaction enthalpy is calculated as follows:

$$\Delta H_r(T_0) = \Delta H_r^\circ + \int_{T_{in}}^{T_0} \sum_j c_{p_j} dT \tag{6.10}$$

where T_{in} and T_0 are the standard and reactor temperature, respectively, and c_{p_j} is the heat capacity of the chemical species j. The combustion is the most exothermic process, followed by the production of acrolein, and of propylene oxide.

Figure 6.2 shows the enthalpy associated with heating the reactants before they enter the reactor $H_{F_{in}}$ and the enthalpy of the reaction H_r for both the illuminated reactor (Figure 6.2a) and the dark reactor (Figure 6.2b), in the same lab conditions as in Figure 6.1.

The plasmonic reactor operates at a lower temperature compared with the dark reactor, and therefore the required heating of the inlet stream is lower. We note that the heating of the inlet does not depend of the reactor volume, as the molar flow rate of oxygen and propylene at the inlet of the reactor is constant and only depends on the

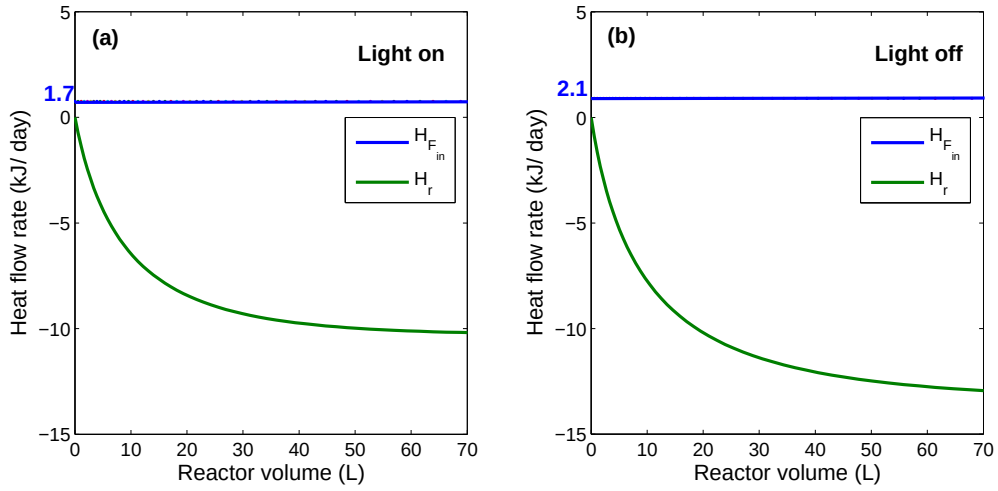

Figure 6.2: Enthalpy of heating for the inlet stream and enthalpy of reaction for the laboratory conditions under the same rate of propylene consumption. The conditions for the reactor are **(a)** illumination (light on), and **(b)** dark (light off). The mass flow rates are calculated using the reported data by Marimuthu et *al.* [25]. In particular the reported rate of propylene consumption is $r = 20\,\mu\text{mol}/\text{g}_{\text{cat}}/\text{s}$ for a working temperature of the illuminated reactor **(a)** is $T = 210$ ℃ and of $T = 260$ ℃ for the dark reactor **(b)**. The reported selectivities are different in both cases: $s_{\text{C}_3\text{H}_6\text{O}} = 0.4$, $s_{\text{C}_3\text{H}_4\text{O}} = 0.22$ and $s_{\text{CO}_2} = 0.38$ for the illuminated reactor; and $s_{\text{C}_3\text{H}_6\text{O}} = 0.2$, $s_{\text{C}_3\text{H}_4\text{O}} = 0.4$, $s_{\text{CO}_2} = 0.4$ for the dark reactor. All the values for the enthalpies of reaction and the specific heat were extracted from the National Institute of Standards and Technology[78].The enthalpy is calculated using eq. 2.30 without considering the term for the cooling of the outlet stream.

reactor temperature and pressure. The enthalpy of reaction is negative, meaning that is an exothermic process and is larger for the dark reactor. This is due to the higher operating temperature, as can be seen from eq., and also to the larger combustion of carbon dioxide. In epoxidation processes the combustion route becomes dominant as temperatures increase[25]. This is a common problem of industrial reactors, and typically a flow of a coolant at lower temperature and high specific heat must be employed to keep the reactor at the operating temperature.

The need for coolant can be reduced if the catalyst is more selective towards propylene oxide, which is a less exothermic process. If we neglect the combustion of propylene oxide, and take into account that carbon dioxide is a waste product Figure indicates that plasmonic reactors are more energy efficient.

6.3 Economic assessment: industrial plasmonic-reactor

The cost of an industrial reactor is mainly determined by its size. When a reactor is scaled up, operating costs such as heating of the reactants, pumping, cooling of the reactor and distillation of the products become significant. In addition, the material required to build the reactor has to be taken into account. From an economic perspective, the cash-flow of operating expenses and benefits must be positive and overcome

the capital costs of purchasing the reactor. Consequently, in the scaling up of the reactor it is important to optimize the size and productivity.

Scaling up to industrial production

In order to achieve an industrial reactor size, we considered a target production of 1 ton of products per day, which is a typical production of single industrial reactor unit, and looked at the assumptions that had to be made in the design equations to calculate the volume that would meet such production:

- **Pressure**: From the design equations 6.8 and eq. 6.5 it is noted that increasing the concentration could lead to an increase of the production. The concentration, defined by the gas law, was increased by raising the pressure of the reactor, since the temperature is kept constant. On basis of two studies[79, 80], that report reactors working with pressures in the range of 10-50 atm, we considered an intermediate pressure of 35 atm.

- **Volumetric flow rate**: We assume that industrial reactors will have a larger volumetric flows of several thousand liters per hour. We did a review of undergraduate books, and find that flows of several hundred liters per hour are described for reactors of a few tens of L. We are aiming at larger reactor sizes, specifically in the order of m^3 and thus we can assume a larger volumetric flow rate[81, 50]. In particular we considered $v_0 = 4000$ L/h. In contrast, the lab reactor of the study by Marimuthu *et al.* had a volumetric flow of $v_0 = 6$ L/h[25].

- **Packing density of the catalyst**: The mass of catalyst per unit volume of reactor was calculated as function of the fraction of the reactor volume filled with the catalyst support, $f_{void}(\%)$ and the fraction of the support volume that contains catalyst $f_{content}(\%)$:

$$\rho_{cat,R} = \rho_{\mathrm{Cu}} \cdot f_{void} \cdot f_{content} \tag{6.11}$$

  where ρ_{Cu} is the mass density of the catalyst. Data about the void fraction was retrieved from a literature search in undergraduate text books, which seem to indicate typical values between 0.3 and 0.5. However, we have to account for the fact that high packing density will lead to increased absorption in the Beer-Lambert law. Therefore we considered we considered $f_{void} = 0.1$ % and $f_{content} = 0.01$ % which results in $\rho_{cat,R} = 8.9\,\mathrm{g_{cat}}/\mathrm{L}_{reactor}$. In comparison, the lab reactor of the study by Marimuthu *et al.* had a packing density of $\rho_{cat,R} = 0.24\,\mathrm{g_{cat}}/\mathrm{L}_{reactor}$[25].

This scaling-up assumptions are used for every industrial reactor modeled in this thesis. In Figure 6.3 we show the outlet stream of unreacted oxygen and propylene (Figure 6.3a) and of the products (Figure 6.3b) as a function of the reactor volume calculated with the design equations for the best selectivity performance of the plasmonic reactor.

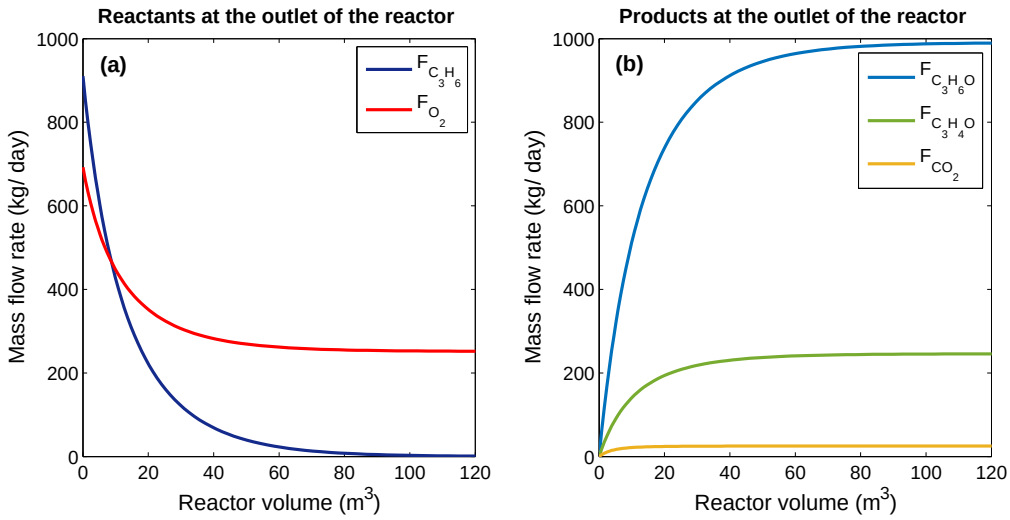

Figure 6.3: Mass flow rates at the outlet of a plasmonic reactor of industrial dimensions for the highest propylene oxide selectivity. Outlet stream of **(a)** propylene and oxygen, and **(b)** propylene oxide, acrolein and carbon dioxide. The mass flow rates are calculated using the reported data by Marimuthu et *al.* [25]. In particular the reported rate of propylene consumption is $r = 10\,\mu\text{mol}/\text{g}_{\text{cat}}/\text{s}$ for a working temperature of the illuminated reactor is $T = 200$ ℃. The reported selectivities are: $s_{\text{C}_3\text{H}_6\text{O}} = 0.5$, $s_{\text{C}_3\text{H}_4\text{O}} = 0.22$ and $s_{\text{CO}_2} = 0.28$.

Note that the reactor volume is in the order of cubic meters, a typical dimension for industrial reactors. For the larger volumes considered, the propylene is consumed in its totality while the oxygen remains in a moderate amount. As mentioned with the laboratory reactor, it can be expected that the remaining oxygen would react with the products, and in a realistic plasmonic reactor the production of propylene and acrolein would be lower.

Capital and Operating cost

The calculation of all the operation expenditures requires several additional assumptions which cannot be extrapolated from the study by Marimuthu *et al.* or from the design equation[25]. These assumptions would introduce a considerable amount of uncertainty in the results, which would have to be added to the uncertainty introduced by our previous assumptions. Consequently, we only consider the heating cost and the raw chemical cost, because it depends on the volumetric stream and the concentration, which are calculated from the design equations. Later in this thesis we discuss what could be a reasonable impact of additional expenses on the total costs.

The net cash-flow is calculated using the formula introduced in the methodology section for the design and assessment of plasmonic reactors, eq.3.6. The operating costs are identified with the OPEX, $C(V_R)$, while the capital costs or CAPEX is given by $\alpha I(V_R)$, where α and I are the capital recovery cost and capital investment, respectively. The benefits $B(V_R)$ are derived from the market price of the outlet stream chemicals, ignoring the cost of separation. We can rewrite eq. 3.6 as follows:

$$Z(k\$/yr) = -\alpha I - \sum_j \left(F_{j,in} \cdot M_j \cdot p_j + p_e \cdot \int_{T_{in}}^{T_0} (F_j c_{p_j})_{in} dT \right) + \left(\sum_j F_{j,out} \cdot M_j \cdot p_j \right) \tag{6.12}$$

where c_{p_j} is the heat capacity, M_j is the molar mass and $F_{j,in}$, $F_{j,out}$ are the molar flow rates at the inlet and outlet of the reactor, respectively, and are given on yearly term basis for the chemical species j. The market price of the chemicals is given by p_j while the electricity cost is given by p_e. The ambient and reactor temperature are represented by T_{in} and T_0, respectively.

It is unrealistic to consider 365 days of continuous operation. Instead the *capacity utilization* can be used, defined as the extent to which the installed capacity is used, with a typical value around the 80%[17]. According to the book of Peters and Timmerhaus , the capital costs can be divided into purchased equipment, installation of equipment, instrumentation, piping and buildings and services facilities[82]. From the book of Peters and Timmerhaus we will assume a reactor cost of 100,000 \$ per m^3[82]. Typical capital recovery factors for new technologies are around 10-15% [75]. Here we consider $\alpha = 15\%$. In addition, we assumed that the reactor cost is linear with the reactor volume, so we can extrapolate the costs to any desired size.

The cash-flows of the industrial plasmonic reactor for the capital costs, the operation costs and the benefits are represented in Figure 6.4 as a function of the reactor volume. It can be observed that the benefits are dominant and grows as a function of the reactor with larger slope until a plateau is reached. Then the annual capital cost, which is a linear function of the reactor size becomes dominant.

The net cash-flow increases in the size range $0 - 12\text{m}^3$, then peaks and falls afterwards, going to negative values. The negative region corresponds to oversized reactors and should be avoided. The peak of the function corresponds to the optimum reactor size, which for the conditions considered here is $V_R = 12.6\,\text{m}^3$. The net cash-flow results in annual profit of 145 k\$/year.

Area of illumination

The area of illumination is a crucial aspect to consider. The path length, derived from the Beer-Lambert law in eq. 3.4, is the constraint parameter that determines the required illumination area given a certain reactor size.

The concentration of catalytic nanoparticles n is related with the packing density $\rho_{cat,R}$ as $n = \rho_{cat,R}/m_{np}$. The catalytic nanoparticle mass m_{np} is given by the catalyst density ρ_{Cu} and the nanoparticle volume V_{np}. Since $\rho_{cat,R} = \rho_{\text{Cu}} \cdot f_{void} \cdot f_{content}$, rearranging we obtain $n = \cdot f_{void} \cdot f_{content}/V_{np}$. According to the study by Marimuthu *et al.*, the nanoparticles are reported to have a size of $r = 41 \pm 9$ nm[25]. As such the concentration is of the order of $10^{19}\,\text{m}^3$.

For copper nanoparticles of 41 nm in size the scattering is negligible at the resonance wavelength. Therefore we only consider the absorption cross-section, which was

[17]Retrieved from https://www.federalreserve.gov/releases/g17/current/

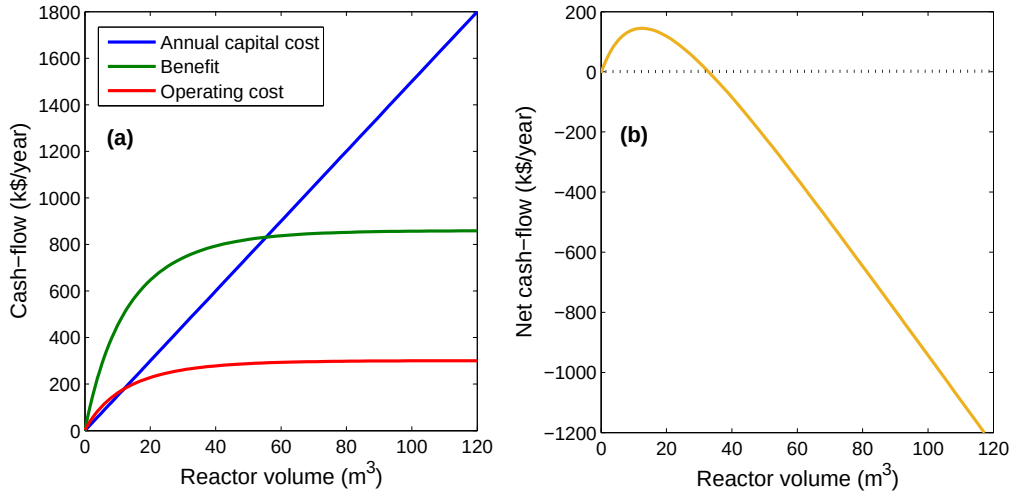

Figure 6.4: Cash-flow for an illuminated plasmonic reactor, on a yearly basis. In **(a)** the individual cash-flow terms, i.e. benefit, operating costs, and annual capital costs are represented while in **(b)** each cash-flow is added up to calculate the net cash-flow. The capital recovery factor is $\alpha = 15\%$. The mass flow rates on daily basis are calculated using the reported data by Marimuthu et *al.* [25]. The yearly production is calculated using a 80% capacity utilization. The reported rate of propylene consumption is $r = 10\,\mu\text{mol}/\text{g}_{\text{cat}}/\text{s}$, and the operating temperature $T = 200\,^{\circ}\text{C}$. The selectivities are $s_{\text{C}_3\text{H}_6\text{O}} = 0.5$, $s_{\text{C}_3\text{H}_4\text{O}} = 0.22$ and $s_{\text{CO}_2} = 0.28$. All the values for the enthalpies of reaction and the specific heat were extracted from the National Institute of Standards and Technology[78].

calculated using FDTD for a copper nanoparticle supported in a silica substrate. The upper dielectric media, which consists of propylene and oxygen, was modeled with a refractive index $n = 1$. At the resonance wavelength, the absorption cross-section is in the order of $10^{-15}\,\text{m}^2$.

In order to determine the path length ℓ we need to assume a value for the transmittance T of the reactor. Here we considered the case in which 99.99 % of light was absorbed, which results in $T = 0.0001$. The path length is of 10^{-4}, i.e. a tenth of a millimeter. The illumination are is calculated for the given reactor size as follwos:

$$A_I = \frac{V_R}{\ell} \tag{6.13}$$

For the plasmonic reactor of industrial dimensions considered, an illumination area of roughly 6000 m^2 or 0.6 ha per m^3 is found. Taking into consideration the small path length, we conclude that according to this model, the realization of a plasmonic reactor would be impossible without a complete reassessment of the light management in the reactor. In addition, since the Beer-Lambert law gives an exponential decrease of the light intensity, for the transmittance considered most of the reactor would remain in the dark, operating as conventional rector. Consequently, the production and the net cash-flow can be expected to change significantly if such reactor were ever build. The reactor cost would be dominated by the transparent window. The support of the window would require challenging engineering. Finally, transparent materials such as

silica do not stand the high pressures typical of a steel vessel, forcing us to revisit our assumption about the reactor pressure. With a lower pressure, the benefits would be reduced, making even less attractive the choice of a plasmonic reactor.

6.4 Economic performance: dark versus illuminated conditions

Regardless of the engineering challenge, the economic attractiveness of the plasmonic reactor is evident from the results illustrated in Figure. Therefore, let's assume in the rest of this section, that somehow we manage to overcome the challenge of light management, and therefore we can benefit from the enhanced catalytic activity of the copper nanoparticles. Then it would be interesting to compare the economic performance of the plasmonic reactor with the dark reactor. Both reactors are scaled-up from the lab models compared in Figure 6.1 using the scaling-up assumptions introduced earlier.

The economic performance is evaluated at the optimum size of each reactor model. Here we consider the same assumptions, i.e. a capacity utilization of 80 % and capital recovery factor of 15 %. The price of each reactor is the same for simplicity. Figure 6.5 shows the net cash-flow of both reactors as a function of the reactor size.

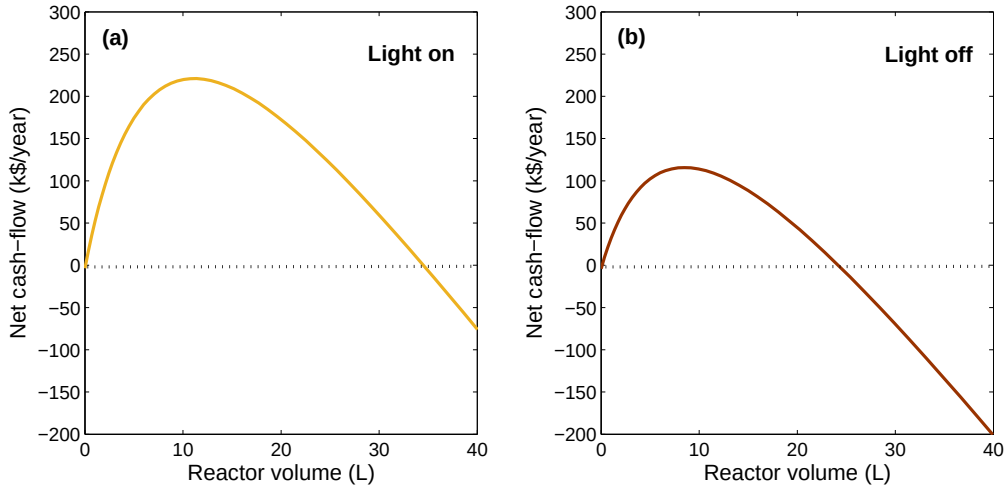

Figure 6.5: Comparative net cash-flow of the plasmonic reactor in the situations of (a) light on, and (b) light off (dark reactor). The mass flow rates on daily basis are calculated using the reported data by Marimuthu et *al.* [25]. The yearly production is calculated using a 80% capacity utilization and annual capital recovery factor is $\alpha = 15\%$. The reported rate of propylene consumption is $r = 20\,\mu\text{mol}/\text{g}_{\text{cat}}/\text{s}$, with an operating temperature of $T = 210$ ℃ for the illuminated reactor **(a)**, of $T = 260$ ℃ for the dark reactor **(b)**. The selectivities are different in both cases: $s_{C_3H_6O} = 0.4$, $s_{C_3H_4O} = 0.22$ and $s_{CO_2} = 0.38$ for the illuminated reactor **(a)**; and $s_{C_3H_6O} = 0.2$, $s_{C_3H_4O} = 0.4$, $s_{CO_2} = 0.4$ for the dark reactor **(b)**. All the values for the enthalpies of reaction and the specific heat were extracted from the National Institute of Standards and Technology[78].

The higher selectivity towards propylene oxide, which has higher market value than

acrolein leads to a higher net cash-flow for the illuminated reactor. The optimum size for the illuminated reactor is $V_R = 11.4\,\mathrm{m}^3$ while for the dark reactor $V_R = 8.5\,\mathrm{m}^3$. At this optimum we find that the illuminated reactor generates approximately 100 k$/year more than the dark reactor.

Note that the illuminated reactor with these conditions has a better economic performance than the illuminated reactor with the best selectivity performance, which was modeled in the Figure 6.4. Comparing both reactors the decrease in propylene oxide selectivity is a 20 % for the reactor modeled in Figure 6.5. However, such reactor has increase in propylene consumption, i.e. propylene conversion, of 100 %.

In order to understand the economic performance of each reactor we decomposed the net cash flows of the reactors into their respective annual capital costs, benefits, and operating costs for the optimum size and highest propylene conversion, which is illustrated in Figure 6.6.

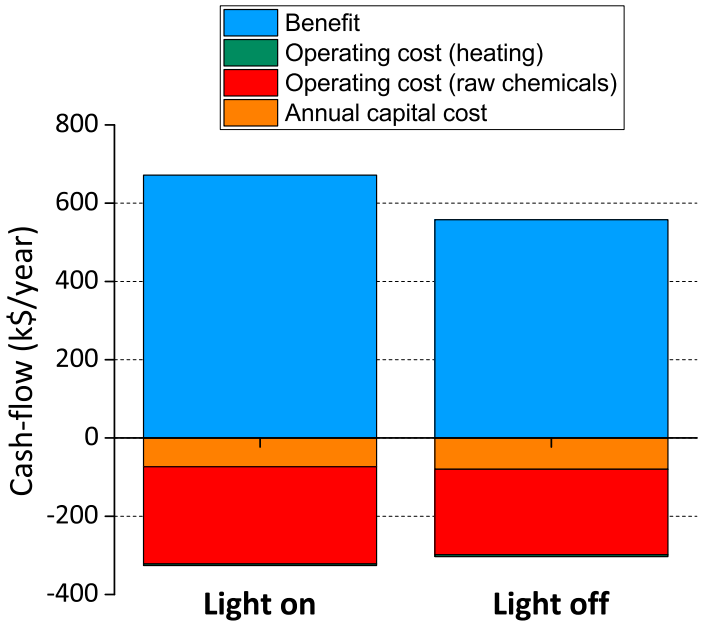

Figure 6.6: Economic performance for the plasmonic and dark reactors, for industrial dimensions and for the same rate of propylene consumption. The reactor conditions are **(a)** illumination (light on), and **(b)** dark (light off). The mass flow rates on daily basis are calculated using the reported data by Marimuthu et *al.* [25]. The yearly production is calculated using a 80% capacity utilization and annual capital recovery factor is $\alpha = 15\%$. In particular the reported rate of propylene consumption is $r \approx 140\,\mu\mathrm{mol}/\mathrm{g}_{\mathrm{cat}}/\mathrm{s}$. At this rate the temperature of the illuminated reactor **(a)** is $T = 260$ ℃ while for the dark reactor **(b)** $T = 310$ ℃. The selectivities are different in both cases: $s_{\mathrm{C_3H_6O}} = 0.29$, $s_{\mathrm{C_3H_4O}} = 0.17$ and $s_{\mathrm{CO_2}} = 0.54$ for the illuminated reactor **(a)**; and $s_{\mathrm{C_3H_6O}} = 0.15$, $s_{\mathrm{C_3H_4O}} = 0.25$, $s_{\mathrm{CO_2}} = 0.6$ for the dark reactor **(b)**.

From a business perspective, high conversion is preferred over high selectivity, as the former leads to larger economic revenue. We investigated how the net cash-flow varies with the propylene conversion and found that in both illuminated and dark reactor the

net cash-flow increases non-linearly. The illuminated rector generates more profit than the dark reactor for all the propylene conversions investigated. The highest consumption rate, $r = 140\,\mu\text{mol}/\text{g}_{\text{cat}}/\text{s}$ corresponds to a net cash-flow of 345 k\$/year, for the illuminated reactor, with a reactor size $V_R = 4.9\,\text{m}^3$, while the dark reactor generates 259 k\$/year, for a reactor size $V_R = 5.33\,\text{m}^3$.

The net cash-flows are decomposed in Figure 6.6. We observe that for the same propylene consumption, the plasmonic reactor generates more benefit due to the larger selectivities toward propylene oxide and acrolein, which have a market value. In contrast, the dark reactor is dominated with a selectivity towards carbon dioxide, which does not have any economic value. The higher operating cost in the plasmonic reactor is due to the larger conversion of the raw chemicals, i.e. propylene and oxygen. We are assuming product separation, so the raw chemicals can be recycled. Recycling reduces the cost of purchasing the raw chemicals, but if the conversion is high then little chemicals are recycled and the price to paid for them increases. However, the reactor price, which is represented by the annual capital cost is smaller in the plasmonic reactor compared with the dark reactor, meaning that is more efficient in terms of production per m^3.

6.5 Discussion

The results obtained in this section are an estimation of what a plasmonic reactor would look like and what benefits could generate compared with a identical reactor operated in the dark. We find that plasmonic reactors offer a high selectivity towards propylene oxide and acrolein, while the selectivity for carbon dioxide is reduced. At the same time, plasmonic reactors require lower operating temperatures than a dark reactor, reducing the cost for heating the inlet stream chemicals. In contrast a reactor of the same characteristics with no illumination has lower production and generates less net cash-flows.

We have neglected operating and capital costs that cannot be calculated from the design equations. However, on the basis of Figure 6.6, we see that the operating costs are dominated by the price of the raw chemicals. The electricity price is relatively a minor expense in the operation of the reactor. While pumping, cooling and distillation would add to the operating costs it is likely they would be still small compared with the raw chemicals purchase. Regarding the capital costs, it is difficult to estimate what would the effect of a more educated guess be in the total cost, since this involves expenses that are not related with the model, but with construction and plant engineering [82].

Regardless of the economic advantages of the plasmonic reactor, the main barrier we identified is the realization of such a reactor. We find, on basis of the Beer-Lambert law, that the absorption would impose a very challenging constraint in the design of such plasmonic reactors. An illumination area of 1 ha per m^3 of reactor and a thickness in the order of hundreds of micrometers to millimeters would not be physically realizable. Such reactor would not sustain the high pressures required for industrial production. In addition, with a transmittance of $T = 0.0001$ most of the reactor would remain in dark conditions, leading to smaller benefit than

the predicted in the last sections. To overcome this challenges the illumination area has to be reduced while the transmittance has to be increased, which cannot be achieved simultaneously on the basis of the Beer-Lambert law. Consequently, we are forced to explore alternative solutions to this challenge.

One possible alternative could be the design of better plasmonic catalysts. Metal nanoparticles with higher activity and selectivity would require smaller concentrations than the ones used for copper. Smaller nanoparticles could increase the total surface area available for a fixed amount of catalyst used. Notably, research in the catalytic properties of other materials which support plasmon resonances could be fundamental in providing the necessary understanding. The plasmon resonance of copper is on the same energy range than the interband absorption edge [30]. Metal nanoparticles such as gold and silver exhibit larger cross-sections that could lead to enhanced catalytic activity compared with copper nanoparticles. Notably, these two metals have been studied in dark conditions for propylene epoxidation with better results in terms of conversion and selectivity [79]. The study of Christopher *et al.* reported higher rate of ethylene epoxidation using silver nanoparticles illuminated with low-intensity visible light, on the order of solar intensity[24]. Ethylene oxide is another chemical highly relevant in the chemical industry, and plasmonic reactors employing silver catalysts could be employed in ethylene and propylene epoxidation, leading to better conversions and thus higher benefits. We calculated the concentration of nanoparticles from the study by Christopher *et al.* to find $n = 3.813 \times 10^{15}\,\text{particles/m}^3$, two order of magnitude lower than the concentration of copper nanoparticles in the study by Marimuthu *et al.* and 4 order of magnitude lower than the concentration of copper nanoparticles used for our industrial reactor model. In contrast, the absorption cross-section is approximately one order of magnitude larger. When we calculated the path length of such illuminated reactor, we find that $\ell = 0.1689$ m, which requires only 6 m^2 per m^3 of reactor. This result highlights the importance of choosing the right catalyst for a given reaction.

In the case of gold, research with gold nanoparticles attracted some attention on basis of the results reported by Hayashi *et al.*[83]. The authors investigated the propylene epoxidation employing gold nanoparticles deposited in a titanium support. The largest advantage of these catalysts for the propene epoxidation is that they are capable of epoxidizing propene very selectively (selectivities of 99+% are very common) under mild conditions (typically 323 K and 1 bar). However, the conversion efficiency is very low and the exact reaction mechanism is still a matter of debate. Combined research to improve the efficiencies and applied plasmon-activated catalysis could result in an economic feasibility of such catalysts if the illumination areas required fall in the range of m^2.

However, the ideal alternative would consist of catalysts that can induce the same effect of plasmonic nanoparticles without requiring visible light, hence eliminating the need for transparent windows. This alternative implies ruling out plasmonic nanoparticles. It is possible to tailor plasmon resonances that belong to other parts of the electromagnetic spectrum such as the infrared[18] or microwaves[19]. However, the main

[18]The infrared spectrum extends from the nominal red edge of the visible spectrum at 700 nanometers (frequency 430 THz), to 1 mm (300 GHz).

[19]Microwaves are a form of electromagnetic radiation with wavelengths ranging from one millimeter

challenge would be to excite such resonances, since it would still require from a high-intensity illumination source. In addition, molecules, and in particular water, present significant absorption in the infrared and microwave, due to the excitation of their vibrational and rotational spectra[30].

The alternative must consists in using materials that, like plasmonic nanoparticles, can inject electrons into the chemical molecules adsorbed into the material surface. However, these materials must, like plasmonic nanoparticles, allow for remote control. Remarkably, such materials exist. One example are *piezoelectric* materials. When mechanical stress is applied to a piezoelectric, thus deforming the crystal lattice, a surface charge is created. A study of Inoue *et al.* reported on the catalysis when surface acoustic waves propagate through a piezoelectric with a ferroelectric deposited in its surface[84]. Acoustic waves are oscillations in pressure, which in a piezoelectric are translated into oscillations of the mechanical stress. Charge will accumulate in the antinodes of the surface wave, where compression is induced. The advantage of using acoustic waves is that they can be easily generated, no illumination window is required, they propagate through solids, and are not absorbed by the gaseous chemicals of the reactor. Although he study by Inoue *et al.* originally did not attracted much research, current studies have reported that by virtue of a constant pressure-induced strain (compression or extension of a material) a catalyst can be optimized for a particular chemical reaction[85, 86]. Therefore we hypothesize that surface acoustic waves in a piezoelectric material that acts as support for metal nanoparticles could lead to surface charges in the metal nanoparticles, therefore activating an enhance catalytic performance. Of course, this idea would require significant research to provide the necessary evidence, but on basis of the catalytic properties of plasmonic nanoparticles, the studies about the effect of strain, and the superior economic performance of improved catalysts, there is an attractiveness in studying such phenomena.

(300 GHz) to one meter (300 MHz).

Conclusion

The assembly of dimers with high yield requires control of the parameters involved in the reaction that ties the two constituent nanoparticles together. We have studied how to achieve control for the particular case in which light is used to excited the plasmon resonances and generate an increase of temperature that can be employed to accelerate the reaction rate of an esterification process. To understand how the optical heating of dimers can lead to control of the dimerization and thus to high yields, we have used a combination of numerical methods, namely the Finite-Differences Time-Domain and Finite Element Method.

Our strategy consists in generating a response only on the dimers, i.e. a selective excitation of the dimer resonances without invoking the plasmon resonance of the individual nanoparticle. **Notably, we have found that the parameter *contrast* can help to optimize the plasmon resonances of dimers**. The contrast was defined as a function absorption cross-section ratio for the individual nanoparticle with respect to the dimer. Moreover, we propose that other dimerization reactions that depend on the enhanced fields in the dimer gap can be optimized as well using the contrast, as the electric fields depend on the nanoparticle size, separation gap, and wavelength of the irradiation source..

In a solution, nanoparticles have to be coated with a ligand, which imposes a constraint on the minimum gap. The gap is a very important parameter according to our simulations, since high contrasts were found at small separations. In our strategy for dimerization, gold nanoparticles particles are coated with polyethylene glycol ligands of an assumed thickness of 5 nm, imposing a gap of 10 nm. **Our simulations suggest that for a given constraint in the gap, we should vary the nanoparticle size in the dimer**. The calculated contrast shows a peak as a function of the size and after tuning for the given dielectric properties of the ligand and the solvent, such size would give the best results in terms of selective excitation of the dimer resonances, for the longitudinal plasmon mode.

However, if a solution of nanoparticles is irradiated with source of constant intensity tuned to the longitudinal dimer resonance, **the temperature increase in the dimers will be always less selective compared with the optical response**. To overcome this issue we propose several alternatives deduced from our simulations of the contrast: (1) use shorter ligands; (2) use different a material composition for the nanoparticle. We are currently investigating shorter ligands, which will allow for a higher contrast. According to our simulations, **plasmonic materials to substitute gold should have a small imaginary part of the dielectric function, as this quantity results in broader resonances**. We found with silver, a material with lower optical losses, that the contrast for the optimum sizes in a gap of 10 nm was higher, reaching almost unity (highest contrast possible).

The question of whether lower thermal selectivity is an issue in the thermal selectivity remains an open question. The reaction rate is non-linear with temperature, following an exponential dependence by virtue of the Arrhenius equation. As such, lower thermal selectivity could be compensated with the different exponential

rates that irradiated dimers and individual nanoparticles have. To investigate the effect of the thermal selectivity we propose to complete the results of this thesis by studying the Brownian dynamics of the nanoparticles. Our discussion in the section 5 showed that **the frequency of collision can be increased, leading to more events for which there is a chance of dimerization, given that the reaction rate is faster than the velocity of the nanoparticles in solution**. It is possible therefore that such studies reveal additional conditions that favor the assembly of nanoparticles.

In summary, the highlight statements contain important conditions that favor the assembly of two nanoparticles using light. From an experimental point of view, it is difficult to estimate quantitatively the exact effect on the yield. Nevertheless, combining chemistry for the synthesis and functionalization of nanoparticles in solution with theoretical studies such as FDTD, FEM, and Brownian dynamics could be a promising approach for light-controlled assembly of nanoparticles with high-yield.

Alternatively, reactions that depend on the enhanced field such as 2-photon polymerizations could be an more efficient route to obtain dimers. Although we did not study such reactions, we base our argument in the fact that a 2-photon polymerization process depends on the intensity of electric field in the dimer gap. The advantage of this approach is the extraordinarily high contrast expected, since the enhancement of field in the dimer gap can be several orders of magnitude larger than the enhancement of the field for individual nanoparticles.

The second part of this thesis, contained in the section 6, focused on the economic assessment of plasmon-activated catalysis. Although such topic is still in fundamental research status, its future depends on the economic attractiveness of potential applications. For such purpose, we decided to study a particular application, chemical reactors, were plasmon-activated catalysis has been proposed as efficient and cleaner alternative. **Our reactor model shows that plasmonic reactors are more efficient than identical reactors without plasmon excitation in terms of productivity and economic revenue**. A higher selectivity and lower operating temperature resulted in smaller reactor size compared with the dark reactor, i.e. plasmonic reactors are more efficients in terms of productivity per m^3 of reactor. Such efficiency could lead to lower capital costs. **In addition, if applied to industrial processes such as ethylene and propylene epoxidation, plasmonic reactors lead to a reduced energy consumption in terms of heating, and also lower carbon emissions per ton of chemical produced**. Other reactions would require from a complete reassessment of the assumptions taken for the epoxidation of propylene. Using the reactor model we developed, in theory we could study other relevant processes for which plasmon-activated catalysis has reported data, such carbon dioxide hydrogenation.

However, **the illumination required to excite plasmon resonances of nanoparticles could severely limit the application of plasmon-induced catalysis at the industrial scale**. Using the Beer-Lambert law, we find that areas up to several hectares are necessary for the scaled-up industrial reactor we studied. Future applications may depend crucially on the illumination area required. Light management in plasmonic reactor is of great significance. We have assumed a simplistic model in which the plasmonic catalysts were irradiated from the top. There is currently technologies such solar plants with light concentration and photochemistry that deal more

efficiently with the light.

On the basis of the economic attractiveness, this study provides a motivation for research in plasmon activated catalysis. **The Beer-Lambert law determines what an ideal plasmonic catalyst should look like**. Namely, such catalyst should provide enhanced activities and selectivities with lower absorption or scattering cross-section, or alternatively with lower concentration. Therefore, understanding better catalytic properties of plasmonic nanoparticle is an essential step. **Notably, studying dimer and other assemblies of interacting nanoparticles could be a preliminary step towards achieving improved catalysts**. As such, through a re-assessment of the results obtained in section 6, future research could be guided in the direction for feasible development of plasmon-enhanced catalytic devices.

A Design and assessment of plasmon-assisted chemical reactors: MATLAB code

```
%% Reactor design analysis
clc
clear

We define the constants for desing equations of the reactor.
% Since the reaction is in gas-phase:
R = 0.0821; % Gas constant (atm/L/K/mol)
T = 533 ; % Temperature (K)
P_tot = 35; % Total pressure in the inlet stream (atm)
x = 0.5; % Pressure ratio
w = 0.5; % Volumetric fraction of the inlet stream
V_0 = 1e-3; % Initial reactor volume (L)
v0 = 4000; % Volumetric flow (L/h)
p_copper = 8.940; % Density of catalyst (kg/L)
v_fraction = 0.1; % Fraction of the reactor filled with the catalyst support
m_content = 0.01; % Fraction of the support with catalyst

r_P_c = 140*3600*1000*1e-6; % Consumption rate of propylene (mol/h/kg)

% Selectivities, rate of reactions from the paper and rate consntants:
s_PO = 0.29; % Selectivity towards propylene oxide
s_CO2 = 0.54; % Selectivity towards carbon dioxide
s_Ac = 0.17; % Selectivity towards acroelein

% Catalyst density in the reactor (kg_cat/L_reactor):
p_cat = p_copper*v_fraction*m_content; % Use for the INDUSTRIAL REACTOR
p_cat = (2.4000e-07)/(1.0000e-03); %(kg_cat/L) % Use for the LABORATORY REACTOR

% Reaction parameters
% Molar mass of the chemicals (g/mol)
n_C3H6 = 42.08; % Propylene
n_O2 = 32; % Oxygen
n_C3H6O = 58.08; % Propylene oxide
n_C3H4O = 56.06; % Acrolein
n_CO2 = 44; % Carbon dioxide
n_H2O = 18; % Water

% Stoichiometric coefficients of oxygen in the reactions
x_PO = 1/2;
x_CO2 = 9/2;
x_Ac = 1;

%(1) CALCULATE THE INITIAL CONDITIONS OF THE REACTANTS
% Concentration and molar fractions:
C_C3H6 = P_tot*x/R/T; % Concentration of propylene (mol/L)
C_O2 = P_tot*(1-x)/R/T; % Concentration of oxygen (mol/L)
C_0 = C_O2 + C_C3H6; % Total concentration (mol/L)
Ftot_0 = C_0*v0;
y_O2_0 = w*C_O2/C_0; % Molar fraction of oxygen
y_P_0 = (1-w)*C_C3H6/C_0; % Molar fraction of propylene

    % (2) CALCULATE THE REACTION RATE CONSTANTS

% Consumption rate:

r_P = r_P_c*(p_cat); % Consumption rate of propylene (mol/L/h)


% Reaction rates of the products (mol/L/h):

r_PO = s_PO*r_P;

r_CO2 = s_CO2*r_P;
```

```
r_Ac = s_Ac*r_P;

% Rate consntats of product formation:
k_PO = r_PO/C_C3H6/(C_O2^(x_PO));
k_CO2 = r_CO2/C_C3H6/(C_O2^(x_CO2));
k_Ac = r_Ac/C_C3H6/(C_O2^(x_Ac));

% Propylene epoxidation is chosen as the reaction limiting step:
n = x_PO + 1; % Order of the reaction
t_cr = 1/(k_PO*C_0^(n-1)); % Characteristic time of the reaction

% (3) DESIGN EQUATION:
% Define the differential equations and solve them
f = @(t,z) [(y_P_0 - z(1) - z(2) - z(3))*(y_O2_0 - 0.5*z(1) - z(2) - 4.5*z(3))^(x_PO)/((1 - 0.5*z(1) + 0.5*z(3))^(x_PO + 1));...
(C_0^(x_Ac - x_PO))*(k_Ac/k_PO)*(y_P_0 - z(1) - z(2) - z(3))*(y_O2_0 - 0.5*z(1) - z(2) - 4.5*z(3))/((1 - 0.5*z(1) +
0.5*z(3))^(x_Ac + 1));...
(C_0^(x_CO2 - x_PO))*(k_CO2/k_PO)*(y_P_0 - z(1) - z(2) - z(3))*(y_O2_0 - 0.5*z(1) - z(2) - 4.5*z(3))^(x_CO2)/((1 - 0.5*z(1)
+ 0.5*z(3))^(x_CO2 + 1))];

% Define the opts for the ODE solverm, the span of values for t, and
% initial values for the conversion exten z
opts = odeset('RelTol',1e-6 ,'AbsTol',1e-6);
tspan = [0 16]; % Dimensionless time span
z_0 = [0 0 0]; % Values at t = 0 for the product equations Z1, Z2, Z3

% Solve the design equation:
[tau,z] = ode45(f, tspan, z_0,opts);

% We have now the dimensionless extent of the three reactions:
Z1 = z(:,1); % Propylene epoxidation
Z2 = z(:,2); % Acrolein formation
Z3 = z(:,3); % Propylene combustion

% Calculate the molar flow rates at the outlet of the reactor:
F_C3H6 = Ftot_0*(y_P_0 - Z1 -Z2 -Z3);
F_O2 = Ftot_0*(y_O2_0 - 0.5*Z1 - Z2 - 4.5*Z3);
F_C3H6O = Ftot_0*Z1;
F_C3H4O = Ftot_0*Z2;
F_CO2 = Ftot_0*3*Z3;
F_H20 = Ftot_0*(3*Z3+Z2);

% Calculate the mass generated in kg per day:
m_C3H6 = Ftot_0*(y_P_0 - Z1 - Z2 - Z3)*_C3H6*24/1000;
m_O2 = Ftot_0*(y_O2_0 - 0.5*Z1 - Z2 - 4.5*Z3)*n_O2*24/1000;
m_C3H6O = Ftot_0*Z1*n_C3H6O*24/1000;
```

```
m_C3H4O = Ftot_0*Z2*n_C3H4O*24/1000;
m_CO2 = Ftot_0*3*Z3*n_CO2*24/1000;
m_H20 = Ftot_0*(3*Z3+Z2)*n_H2O*24/1000;

% Reactor volume:
VR=tau*v0*t_cr;

% Show the results as a function of the reactor volume:
f1 = figure(1);
subplot(1,2,1)
plot(VR/1000,m_C3H6, VR/1000,m_O2,'LineWidth',2)
ylabel('Molar flow rate (kg/ day)','FontSize',13.2)
title('Reactants at the outlet of the reactor','FontSize',13.2,'FontWeight','bold','Color','r')
legend('F_C_3_H_6','F_O_2')
xlabel('Reactor volume (L)','FontSize',13.2)

subplot(1,2,2)
plot(VR/1000,m_C3H6O, VR/1000,m_C3H4O, VR/1000,_CO2,'LineWidth',2)
xlabel('Reactor volume (m^3)','FontSize',13.2)
ylabel('Molar flow rate (kg/day)','FontSize',13.2)
title('Products at the outlet of the reactor','FontSize',13.2,'FontWeight','bold','Color','r')
legend('F_C_3_H_6_O','F_C_3_H_4_O','F_C_O_2')



%% Enery balance analysis
% Here we calculate the rate of heat that has to be added to the reactor

% THERMODYNAMIC DATA

% Initial temperature (K)
Ti = 298.15;
t = T/1000;

% Standard heat capacity (1 atm, 298.15 K)
% Products (J/mol*K):
cp_O2_0 = 31.32234 - 20.23531*t + 57.86644*(t^2) - 36.50624*(t^3) - 0.007374/(t^2);
cp_C3H6_0 = 64.32;

% Reactants (J/mol*K):
cp_C3H6O_0 = 72.55;
cp_C3H4O_0 = 71.28;
cp_CO2_0 = 24.99735 + 55.18696*t -33.69137*(t^2) + 7.948387*(t^3) - 0.136638/(t^2);
cp_H2O_0 = 30.09200 + 6.832514*t + 6.793435*(t^2) - 2.534480*(t^3) + 0.082139/(t^2);
```

```
% Standar formation enthalpies (1 atm, 298.15 K)
% Products (kJ/mol):
Hf_O2_0 = 0;
Hf_C3H6_0 = 20.41;

% Reactants (kJ/mol):
Hf_C3H6O_0 = -94.68;
Hf_C3H4O_0 = -65.40;
Hf_CO2_0 = -393.52;
Hf_H20_0 = -241.83;

% Formation enthalpies - temperature dependence
% Products (kJ/mol):
Hf_O2 = Hf_O2_0 + 31.32234*t - 20.23531*(t^2)/2 + 57.86644*(t^3)/3 - 36.50624*(t^4)/4 + 0.007374/t - 8.903471;
Hf_C3H6 = Hf_C3H6_0 + 23.68212/1000*(T-Ti) + 0.13885/1000/2*((T^2)-(Ti^2));

% Reactants (kJ/mol):
Hf_C3H6O = Hf_C3H6O_0 + 23.68212/1000*(T-Ti) + 0.13885/1000/2*((T^2)-(Ti^2));
Hf_C3H4O = Hf_C3H4O_0 + 23.68212/1000*(T-Ti) + 0.13885/1000/2*((T^2)-(Ti^2));
Hf_CO2 = Hf_CO2_0 + 24.99735*t + 55.18696*(t^2)/2 -33.69137*(t^3)/3 + 7.948387*(t^4)/4 + 0.136638/t - 403.6075;
Hf_H20 = Hf_H20_0 + 30.09200*t + 6.832514*(t^2)/2 + 6.793435*(t^3)/3 - 2.534480*(t^4)/4 - 0.082139/t - 250.8810;

% Standard reaction enthalpy (1 atm, 298.15 K)(kJ/mol)
Hr1_0 = (Hf_C3H6O_0 + 4.5*Hf_O2_0) - (Hf_C3H6_0 + 0.5*Hf_O2_0);
Hr2_0 = (Hf_C3H4O_0 + Hf_H20_0) - (Hf_C3H6_0 + Hf_O2_0);
Hr3_0 = (3*Hf_CO2_0 + 3*Hf_H20_0) - (Hf_C3H6_0 + 4.5*Hf_O2_0);

% Reaction enthalpy (1 atm, High-T)(kJ/mol)
Hr1 = (Hf_C3H6O) - (Hf_C3H6 + 0.5*Hf_O2);
Hr2 = (Hf_C3H4O + Hf_H20) - (Hf_C3H6 + Hf_O2);
Hr3 = (3*Hf_CO2 + 3*Hf_H20) - (Hf_C3H6 + 4.5*Hf_O2);

Hr_4=(3*Hf_CO2 + 3*Hf_H20) - (Hf_C3H6O + 4*Hf_O2);

% Heat balance associated with the enthalpy of reaction (Q_Hr)(kJ/mol), the heating of
% the inlet stream (Q_F_in)(kJ/mol) and the cooling of the outlet stream (Q_F_out)(kJ/mol):
Q_Hr = Ftot_0*(Hr1*(Z1) + Hr2*(Z2) + Hr3*(Z3));
Q_F_in = Ftot_0*(y_O2_0*(31.32234*t - 20.23531*(t^2)/2 + 57.86644*(t^3)/3 - 36.50624*(t^4)/4 + 0.007374/t - 8.903471)+
y_P_0*(23.68212/1000*(T-Ti) + 0.13885/1000/2*((T^2)-(Ti^2))));
Q_F_out = (F_C3H6O*cp_C3H6O_0 + F_C3H4O*cp_C3H4O_0 + F_CO2*cp_CO2_0)*(T-Ti);

% We only consider the heating (kJ/mol) of the inlet stream for the cost-benefit:
Q = Q_F_in;
```

```
%% Economic performance of the reactor
% Price of the chemicals
p_C3H6 = 1.1/(1000/n_C3H6); % Propylene price ($/mol)
p_O2 = 0.04/(1000/n_O2); % Oxygen price ($/mol)
p_C3H6O = 2.5/(1000/n_C3H6O); % Propylene oxide price ($/mol)
p_C3H4O = 1.90/(1000/n_C3H4O); % Acrolein price ($/mol)
% Price of electricity
p_e = 0.0808/3600;

% Heater efficiecy
n_eff = 0.8;
Q_e = Q/n_eff; % Supplied heat by the electric heater

% Calculate the cost and benefits of the reactor
Cost = zeros(length(tau),1);
B = zeros(length(tau),1);
Cost_c = zeros(length(tau),1);

for i=1:length(tau)
Cost_c(i)=p_C3H6*(F_C3H6(1)-F_C3H6(i)) + p_O2*(F_O2(1)-F_O2(i)); % Cost of chemicals
B(i) = F_C3H6O(i)*p_C3H6O + F_C3H4O(i)*p_C3H4O; % Benefit of chemicals
end

% OPEX
C = Cost_c + Q_e*p_e;

% CAPEX
I = VR*100; % Investment cost of the reactor
a = 0.15; % Capital recovery factor

% Net cash-flow on a yearly basis
cu = 0.8; % Capacity utilization factor
Z_yr = (B - C)*cu*24*365/1000 -a*I/1000;

% Results for the net cash-flow
f2 = figure(2);
subplot(1,2,1)
plot(VR/1000,a*I/1000,VR/1000,B*cu*24*365/1000, VR/1000,C*cu*24*365/1000,'LineWidth',2)
xlabel('Reactor volume (L)','FontSize',13.2)
ylabel('Economic objective function (k$/year)','FontSize',13.2)

subplot(1,2,2)
plot(VR/1000,Z_yr,'LineWidth',2)
xlabel('Reactor volume (L)','FontSize',13.2)
ylabel('Economic objective function (k$/year)','FontSize',13.2)
```

```
%% Area required of illumination
% Nanoparticle radius:
r = 20.5*1e-9;
% Cross-section calculated with FDTD:
cs = 2668.24*1e-18;

% Nanoparticle concentration in the reactor:
n = v_fraction*m_content/(4/3*pi*(r^3));

% Transmittance- INTRODUCE A VALUE
T = 0.00001;
% Path length of the reactor:
l = - log(T)/n/cs;

% ILLUMINATION AREA
[m, I]=max(Z_yr); % Optimum reactor size
A_i = VR(I)/l;
```

References

[1] G. Myhre, D. Shindell, F.-M. Bréon, W. Collins, J. Fuglestvedt, J. Huang, D. Koch, J.-F. Lamarque, D. Lee, B. Mendoza, T. Nakajima, A. Robock, G. Stephens, T. Takemura, and H. Zhang. Anthropogenic and Natural Radiative Forcing. In *Climate Change 2013: The Physical Science Basis. Contribution of Working Group I to the Fifth Assessment Report of the Intergovernmental Panel on Climate Change*, chapter 8. Cambridge University Press, 2013.

[2] M. Collins, R. Knutti, J. Arblaster, J.-L. Dufresne, T. Fichefet, P. Friedlingstein, X. Gao, W.J. Gutowski, T. Johns, G. Krinner, M. Shongwe, C. Tebaldi, A. J. Weaver, and M. Wehner. Long-term Climate Change: Projections, Commitments and Irreversibility. In *Climate Change 2013: The Physical Science Basis. Contribution of Working Group I to the Fifth Assessment Report of the Intergovernmental Panel on Climate Change*, chapter 12. Cambridge University Press, 2013.

[3] Cynthia Rosenzweig, Gino Casassa, David J. Karoly, Anton Imeson, Chunzhen Liu, Annette Menzel, Samuel Rawlins, Terry L. Root, Bernard Seguin, Piotr Tryjanowski, et al. Assessment of observed changes and responses in natural and managed systems. *Climate Change*, 2007:79, 2007.

[4] C.B. Fields, R. Barros, D.J. Dokken, K.J. Mach, Te Bilir, M. Chatterjee, K.L. Ebi, Yo Estrada, R.C. Genova, B. Girma, Es Kissel, An Levy, and S. MacCracken. Summary for policymakers. In *Climate Change 2014: Impacts,Adaptation, and Vulnerability. Part A: Global and Sectoral Aspects. Contribution of Working Group II to the Fifth Assessment Report of the Intergovernmental Panel on Climate Change*, pages 1–32. Cambridge University Press, 2014.

[5] International Energy Agency (IEA). Key World Energy Statistics 2016, 2016.

[6] Energy Information Administration (EIA). International Energy Outlook 2016, 2016.

[7] International Monetary Fund (IMF). World Economic Outlook - October 2016: Subdued Demand - Symptoms and Remedies, 2016.

[8] Bwo-Nung Huang, Ming Jeng Hwang, and Chin Wei Yang. Causal relationship between energy consumption and GDP growth revisited: a dynamic panel data approach. *Ecological Economics*, 67(1):41–54, 2008.

[9] Leon Clarke, Kejun Jiang, Keigo Akimoto, Mustafa Babiker, Geoffrey Blanford, Karen Fisher-Vanden, J-C Hourcade, Volker Krey, Elmar Kriegler, Andreas Löschel, et al. Assessing Transformation Pathways. In *Climate Change 2014: Mitigation of Climate Change. Contribution of Working Group III to the Fifth Assessment Report of the Intergovernmental Panel on Climate Change*, chapter 6.

[10] Stephen Pacala and Robert Socolow. Stabilization wedges: solving the climate problem for the next 50 years with current technologies. *Science*, 305(5686):968–972, 2004.

[11] David Archer, Michael Eby, Victor Brovkin, Andy Ridgwell, Long Cao, Uwe Mikolajewicz, Ken Caldeira, Katsumi Matsumoto, Guy Munhoven, Alvaro Montenegro, et al. Atmospheric lifetime of fossil fuel carbon dioxide. *Annual Review of Earth and Planetary Sciences*, 37, 2009.

[12] Harry B. Gray. Powering the planet with solar fuel. *Nature chemistry*, 1(1):7–7, 2009.

[13] Kazuhiko Maeda, Kentaro Teramura, Daling Lu, Tsuyoshi Takata, Nobuo Saito, Yasunobu Inoue, and Kazunari Domen. Photocatalyst releasing hydrogen from water. *Nature*, 440(7082):295–295, 2006.

[14] Somnath C. Roy, Oomman K. Varghese, Maggie Paulose, and Craig A. Grimes. Toward solar fuels: photocatalytic conversion of carbon dioxide to hydrocarbons. *Acs Nano*, 4(3):1259–1278, 2010.

[15] Tarik Kousksou, Pascal Bruel, Abdelmajid Jamil, T El Rhafiki, and Youssef Zeraouli. Energy storage: Applications and challenges. *Solar Energy Materials and Solar Cells*, 120:59–80, 2014.

[16] Yimin Li and Gabor A. Somorjai. Nanoscale advances in catalysis and energy applications. *Nano letters*, 10(7):2289–2295, 2010.

[17] Nathan S. Lewis and Daniel G. Nocera. Powering the planet: Chemical challenges in solar energy utilization. *Proceedings of the National Academy of Sciences*, 103(43):15729–15735, 2006.

[18] J.A. Dionne, A. Baldi, B. Baum, C.-S. Ho, V. Janković, G.V. Naik, T. Narayan, J.A. Scholl, and Y. Zhao. Localized fields, global impact: Industrial applications of resonant plasmonic materials. *MRS Bulletin*, 40(12):1138–1145, 2015.

[19] Matthew J. Kale, Talin Avanesian, and Phillip Christopher. Direct photocatalysis by plasmonic nanostructures. *ACS Catalysis*, 4(1):116–128, 2013.

[20] Mark L. Brongersma, Naomi J. Halas, and Peter Nordlander. Plasmon-induced hot carrier science and technology. *Nature Nanotechnology*, 10(1):25–34, 2015.

[21] Stefan A. Maier. *Plasmonics: fundamentals and applications*. Springer Science & Business Media, 2007.

[22] Guillaume Baffou and Romain Quidant. Nanoplasmonics for chemistry. *Chemical Society Reviews*, 43(11):3898–3907, 2014.

[23] Guillaume Baffou and Romain Quidant. Thermo-plasmonics: using metallic nanostructures as nano-sources of heat. *Laser & Photonics Reviews*, 7(2):171–187, 2013.

[24] Phillip Christopher, Hongliang Xin, and Suljo Linic. Visible-light-enhanced catalytic oxidation reactions on plasmonic silver nanostructures. *Nature Chemistry*, 3(6):467–472, 2011.

[25] Andiappan Marimuthu, Jianwen Zhang, and Suljo Linic. Tuning selectivity in propylene epoxidation by plasmon mediated photo-switching of Cu oxidation state. *Science*, 339(6127):1590–1593, 2013.

[26] Xiao Zhang, Xueqian Li, Du Zhang, Neil Qiang Su, Weitao Yang, Henry O. Everitt, and Jie Liu. Product selectivity in plasmonic photocatalysis for carbon dioxide hydrogenation. *Nature Communications*, 8:14542, 2017.

[27] Max Born and Emil Wolf. *Principles of optics: electromagnetic theory of propagation, interference and diffraction of light*. Elsevier, 2013.

[28] John David Jackson. *Classical electrodynamics*. John Wiley & Sons, 2007.

[29] Craig F. Bohren and Donald R. Huffman. *Absorption and scattering of light by small particles*. John Wiley & Sons, 2008.

[30] Mark Fox. *Optical properties of solids*. Oxford University Press, 2002.

[31] John W. Strutt. On the light from the sky, its polarization and colour. *The London, Edinburgh, and Dublin Philosophical Magazine and Journal of Science*, 41(271):107–120, 1871.

[32] Paul Lorrain and Dale Corson. *Electromagnetic fields and waves*. Freeman, 1970.

[33] Peter Nordlander, C Oubre, E Prodan, K Li, and MI Stockman. Plasmon hybridization in nanoparticle dimers. *Nano letters*, 4(5):899–903, 2004.

[34] Gustav Mie. Beiträge zur Optik trüber Medien, speziell kolloidaler Metallösungen. *Annalen der physik*, 330(3):377–445, 1908.

[35] Viktor Myroshnychenko, Jessica Rodríguez-Fernández, Isabel Pastoriza-Santos, Alison M. Funston, Carolina Novo, Paul Mulvaney, Luis M. Liz-Marzán, and Francisco J. Garcia de Abajo. Modelling the optical response of gold nanoparticles. *Chemical Society Reviews*, 37(9):1792–1805, 2008.

[36] William L. Barnes, Alain Dereux, and Thomas W. Ebbesen. Surface plasmon subwavelength optics. *nature*, 424(6950):824, 2003.

[37] Peter B. Johnson and R-W. Christy. Optical constants of the noble metals. *Physical Review B*, 6(12):4370, 1972.

[38] Matthew Pelton, Javier Aizpurua, and Garnett Bryant. Metal-nanoparticle plasmonics. *Laser & Photonics Reviews*, 2(3):136–159, 2008.

[39] Miguel A. García. Surface plasmons in metallic nanoparticles: fundamentals and applications. *Journal of Physics D: Applied Physics*, 44(28):283001, 2011.

[40] Steven R. Emory and Shuming Nie. Near-field surface-enhanced raman spectroscopy on single silver nanoparticles. *Analytical chemistry*, 69(14):2631–2635, 1997.

[41] Dakrong Pissuwan, Stella M. Valenzuela, and Michael B. Cortie. Therapeutic possibilities of plasmonically heated gold nanoparticles. *TRENDS in Biotechnology*, 24(2):62–67, 2006.

[42] Alexander O. Govorov and Hugh H. Richardson. Generating heat with metal nanoparticles. *Nano Today*, 2(1):30–38, 2007.

[43] Linyou Cao, David N. Barsic, Alex R. Guichard, and Mark L. Brongersma. Plasmon-assisted local temperature control to pattern individual semiconductor nanowires and carbon nanotubes. *Nano Letters*, 7(11):3523–3527, 2007.

[44] Syed Mubeen, Joun Lee, Nirala Singh, Stephan Krämer, Galen D Stucky, and Martin Moskovits. An autonomous photosynthetic device in which all charge carriers derive from surface plasmons. *Nature nanotechnology*, 8(4):247–251, 2013.

[45] Xiaofeng Fan, Weitao Zheng, and David J. Singh. Light scattering and surface plasmons on small spherical particles. *arXiv preprint arXiv:1407.2345*, 2014.

[46] Theodore L. Bergman and Frank P. Incropera. *Fundamentals of heat and mass transfer*. John Wiley & Sons, 2011.

[47] Guillaume Baffou, Romain Quidant, and F Javier Garcia de Abajo. Nanoscale control of optical heating in complex plasmonic systems. *ACS Nano*, 4(2):709–716, 2010.

[48] Guillaume Baffou and Hervé Rigneault. Femtosecond-pulsed optical heating of gold nanoparticles. *Physical Review B*, 84(3):035415, 2011.

[49] Octave Levenspiel. *Chemical reaction engineering, 3rd Edition*. John Wiley & Sons, 1999.

[50] Uzi Mann. *Principles of chemical reactor analysis and design: new tools for industrial chemical reactor operations*. John Wiley & Sons, 2009.

[51] Uri M. Ascher and Linda R. Petzold. *Computer methods for ordinary differential equations and differential-algebraic equations*, volume 61. Siam, 1998.

[52] James R. Welty, Charles E. Wicks, Gregory Rorrer, and Robert E. Wilson. *Fundamentals of momentum, heat, and mass transfer*. John Wiley & Sons, 2009.

[53] Emil Prodan, Corey Radloff, Naomi J Halas, and Peter Nordlander. A hybridization model for the plasmon response of complex nanostructures. *science*, 302(5644):419–422, 2003.

[54] Chad E. Talley, Joseph B. Jackson, Chris Oubre, Nathaniel K Grady, Christopher W. Hollars, Stephen M. Lane, Thomas R. Huser, Peter Nordlander, and Naomi J. Halas. Surface-enhanced Raman scattering from individual Au nanoparticles and nanoparticle dimer substrates. *Nano Letters*, 5(8):1569–1574, 2005.

[55] W. Rechberger, A. Hohenau, A. Leitner, J.R. Krenn, B. Lamprecht, and F.R. Aussenegg. Optical properties of two interacting gold nanoparticles. *Optics Communications*, 220(1):137–141, 2003.

[56] Stefan A. Maier, Mark L. Brongersma, Pieter G. Kik, and Harry A. Atwater. Observation of near-field coupling in metal nanoparticle chains using far-field polarization spectroscopy. *Physical Review B*, 65(19):193408, 2002.

[57] Isabel Romero, Javier Aizpurua, Garnett W Bryant, and Francisco J. Garcia De Abajo. Plasmons in nearly touching metallic nanoparticles: singular response in the limit of touching dimers. *Optics express*, 14(21):9988–9999, 2006.

[58] Javier Aizpurua, Garnett W. Bryant, Lee J. Richter, Francisco J. García De Abajo, Brian K. Kelley, and T. Mallouk. Optical properties of coupled metallic nanorods for field-enhanced spectroscopy. *Physical Review B*, 71(23):235420, 2005.

[59] Zhihong Nie, Alla Petukhova, and Eugenia Kumacheva. Properties and emerging applications of self-assembled structures made from inorganic nanoparticles. *Nature nanotechnology*, 5(1):15–25, 2010.

[60] Kosei Ueno, Saulius Juodkazis, Toshiyuki Shibuya, Yukie Yokota, Vygantas Mizeikis, Keiji Sasaki, and Hiroaki Misawa. Nanoparticle plasmon-assisted two-photon polymerization induced by incoherent excitation source. *Journal of the American Chemical Society*, 130(22):6928–6929, 2008.

[61] Guillermo González-Rubio, Jesus Gonzalez-Izquierdo, Luis Banares, Gloria Tardajos, Antonio Rivera, Thomas Altantzis, Sara Bals, Ovidio Peña-Rodríguez, Andrés Guerrero-Martínez, and Luis M Liz-Marzan. Femtosecond laser-controlled tip-to-tip assembly and welding of gold nanorods. *Nano Letters*, 15(12):8282–8288, 2015.

[62] Frederick Bettelheim, William Brown, Mary Campbell, Shawn Farrell, and Omar Torres. *Introduction to general, organic and biochemistry*. Nelson Education, 2012.

[63] Wenqi Zhu, Ruben Esteban, Andrei G. Borisov, Jeremy J. Baumberg, Peter Nordlander, Henri J. Lezec, Javier Aizpurua, and Kenneth B. Crozier. Quantum mechanical effects in plasmonic structures with subnanometre gaps. *Nature Communications*, 7:11495, 2016.

[64] K.K. Nanda, A. Maisels, F.E. Kruis, H. Fissan, and S. Stappert. Higher surface energy of free nanoparticles. *Physical review letters*, 91(10):106102, 2003.

[65] Amro Badawy, Todd P. Luxton, Rendahandi G. Silva, Kirk G. Scheckel, Makram T. Suidan, and Thabet M. Tolaymat. Impact of environmental conditions (pH, ionic strength, and electrolyte type) on the surface charge and aggregation of silver nanoparticles suspensions. *Environmental Science & technology*, 44(4):1260–1266, 2010.

[66] Joanne Manson, Dhiraj Kumar, Brian J. Meenan, and Dorian Dixon. Polyethylene glycol functionalized gold nanoparticles: the influence of capping density on stability in various media. *Gold Bulletin*, 44(2):99–105, 2011.

[67] Stefano Ottani, Daniele Vitalini, Fabio Comelli, and Carlo Castellari. Densities, viscosities, and refractive indices of poly (ethylene glycol) 200 and 400+ cyclic ethers at 303.15 K. *Journal of Chemical & Engineering Data*, 47(5):1197–1204, 2002.

[68] Erik C. Garnett, Wenshan Cai, Judy J. Cha, Fakhruddin Mahmood, Stephen T. Connor, M. Greyson Christoforo, Yi Cui, Michael D. McGehee, and Mark L. Brongersma. Self-limited plasmonic welding of silver nanowire junctions. *Nature Materials*, 11(3):241–249, 2012.

[69] Jacob H Masliyah and Subir Bhattacharjee. *Electrokinetic and colloid transport phenomena*. John Wiley & Sons, 2006.

[70] Peter Atkins and Julio de Panda. *Physical Chemistry, 8th Edition*. W. H. Freeman and Company, 2006.

[71] Kurt W. Kolasinski. *Surface science: foundations of catalysis and nanoscience*. John Wiley & Sons, 2012.

[72] Paul T. Anastas, Mary M. Kirchhoff, and Tracy C. Williamson. Catalysis as a foundational pillar of green chemistry. *Applied Catalysis A: General*, 221(1):3–13, 2001.

[73] Vivek Polshettiwar and Rajender S. Varma. Green chemistry by nano-catalysis. *Green Chemistry*, 12(5):743–754, 2010.

[74] Susie Eustis and Mostafa A. El-Sayed. Why gold nanoparticles are more precious than pretty gold: noble metal surface plasmon resonance and its enhancement of the radiative and nonradiative properties of nanocrystals of different shapes. *Chemical society reviews*, 35(3):209–217, 2006.

[75] Kornelis Blok and Evert Nieuwlaar. *Introduction to energy analysis*. Taylor & Francis, 2016.

[76] Owain P.H. Vaughan, Georgios Kyriakou, Norman Macleod, Mintcho Tikhov, and Richard M. Lambert. Copper as a selective catalyst for the epoxidation of propene. *Journal of Catalysis*, 236(2):401–404, 2005.

[77] Ye Wang, Hui Chu, Wenming Zhu, and Qinghong Zhang. Copper-based efficient catalysts for propylene epoxidation by molecular oxygen. *Catalysis Today*, 131(1):496–504, 2008.

[78] NIST-JANAF Thermochemical Tables. *Journal of Physical and Chemical Reference Data Monograph No. 9*.

[79] Alexander Nijhuis, Michiel Makkee, Jacob A. Moulijn, and Bert M. Weckhuysen. The production of propene oxide: catalytic processes and recent developments. *Industrial & engineering Chemistry research*, 45(10):3447–3459, 2006.

[80] Eric W. Schultz, Mitchell B. Schwartz, and Kyle M Yu. Production of propylene oxide from propylene using patented silver based catalyst. *Senior Design Reports (CBE)*, 2016.

[81] H. Scott Fogler. *Elements of chemical reaction engineering*. Prentice-Hall International London, 1999.

[82] Max Stone Peters, Klaus D. Timmerhaus, Ronald E. West, Klaus Timmerhaus, and Ronald West. *Plant design and economics for chemical engineers*, volume 4. McGraw-Hill New York, 1968.

[83] Toshio Hayashi, Koji Tanaka, and Masatake Haruta. Selective vapor-phase epoxidation of propylene over au/tio2catalysts in the presence of oxygen and hydrogen. *Journal of Catalysis*, 178(2):566–575, 1998.

[84] Yasunobu Inoue, Masahiko Matsukawa, and Kazunori Sato. Effect of surface acoustic wave generated on ferroelectric support upon catalysis. *Journal of the American Chemical Society*, 111(24):8965–8966, 1989.

[85] Peter Strasser, Shirlaine Koh, Toyli Anniyev, Jeff Greeley, Karren More, Chengfei Yu, Zengcai Liu, Sarp Kaya, Dennis Nordlund, Hirohito Ogasawara, et al. Lattice-strain control of the activity in dealloyed core–shell fuel cell catalysts. *Nature chemistry*, 2(6):454–460, 2010.

[86] Sen Zhang, Xu Zhang, Guangming Jiang, Huiyuan Zhu, Shaojun Guo, Dong Su, Gang Lu, and Shouheng Sun. Tuning nanoparticle structure and surface strain for catalysis optimization. *Journal of the American Chemical Society*, 136(21):7734–7739, 2014.

Acknowledgments

This thesis has been in many ways both a personal and a professional journey. There is a lot I have learned, not only at the academic level from my internship in the group of dr. Andrea Baldi at DIFFER. In addition I was lucky to have the support of persons which are close to me. Therefore, I would like to thank all of them in this section. Starting with my supervisor, dr. Andrea Baldi. Thanks for the opportunity to do my master thesis in your group. You have taught me what science is about, and that we should try to put the standards for research as high as possible. Above all you have taught to think critically in the assumptions and steps to follow during the several projects we have done together. Mention apart is for Rifat Kamarudheen. Your daily supervision has been very positive. Taking into account that there were some years without doing any physics, I overestimated by far how much things I forgot about research, which made some tasks more difficult. However, you have been patience, and all your advices have helped to reach the end of this thesis. I also would like to thank my girlfriend and my parents, who have supported me a lot during all these months, and made me realize I could do this. To Ruben Hamans and Matteo Parente, you have filled with jokes the time at the office and the breaks for lunch an coffee. To my supervisor at Utrecht University, prof.dr. Gert Jan Kramer, for giving me this opportunity to make a thesis in fundamental research and the useful insights in thinking more practically like an engineer. Finally I would like to thank the group of prof.dr. Jaime Gmez Rivas for the feedback on photonics related questions and to prof.dr.ir. Martin van Sint Annaland for the advices provided in the design of the plasmonic reactor.